TAMPEREEN TEKNILLINEN YLIOPISTO
TAMPERE UNIVERSITY OF TECHNOLOGY

Markku Kakko

The effect of the geometric parameters to the thermal-hydraulic dimensioning of a H-type finned tube heat exchanger

Master of Science Thesis

Examiners
Sc.D Seppo Syrjälä
Doctoral student Turo Välikangas
Examiner and topic approved on
1th November 2017

ABSTRACT

TAMPERE UNIVERSITY OF TECHNOLOGY
Master's Degree Programme in Environmental and Energy Engineering
KAKKO, MARKKU: The effect of the geometric parameters to the thermal-hydraulic dimensioning of a H-type finned tube heat exchanger
Master of Science Thesis, 91 pages, 35 appendix pages
November 2017
Major: Energy efficiency
Examiners: Sc.D Seppo Syrjälä, Doctoral student Turo Välikangas
Keywords: finned tube, heat transfer, CFD, pressure drop, heat transfer coefficient, fin efficiency, thermal-hydraulic

The effect of the geometrical parameters of the in-line H-type finned tube to the heat exchanger dimensioning was studied in this Master's thesis. As the flow field around tubes and fins does not anneal to simple analytical solutions, computational fluid dynamics (CFD) was extensively used in this thesis to calculate heat transfer and pressure drop for different finned tube geometries. The calculation method was found to be in line with the validation experiment.

The data from CFD solution was reduced into a non-dimensional form as Reynolds number based correlations of the Nusselt and Euler numbers and fin efficiency. Additionally, universal correlations for all geometrical parameters were developed for the Nusselt number, Colburn j-factor, Euler number, Fanning friction factor and fin efficiency which are given in the appendices.

With the correlations from the CFD solutions, a thermal-hydraulic dimensioning was made for all CFD cases for equal heat transfer rate and pressure drop. The cases were then compared to the reference geometry to get insight on the effect of the geometric parameters in the heat exchanger core mass, volume and approximate manufacturing welding work for a given conductance and pressure drop requirement. The fin pitch was found to have the highest effect on all performance parameters while the tube pitches and fin thickness was found to be the next important geometric parameters. The least important geometric parameters were the gap between fins and the slit width of the fin.

TIIVISTELMÄ

TAMPEREEN TEKNILLINEN YLIOPISTO
Ympäristö- ja energiatekniikan koulutusohjelma
KAKKO, MARKKU: H-tyypin ripaputkilämmönsiirtimen geometrian vaikutus termohydrauliseen mitoitukseen
Diplomityö, 91 sivua, 35 liitesivua
Marraskuu 2017
Pääaine: Energiatehokkuus
Tarkastajat: Tekniikan tohtori Seppo Syrjälä ja tohtoriopiskelija Turo Välikangas
Avainsanat: ripaputki, lämmönsiirto, virtauslaskenta, painehäviö, lämmönsiirtokerroin, ripahyötysuhde, termohydraulinen

Tässä diplomityössä tutkittiin H-tyypin ripaputkisiirtimen geometrian vaikutusta lämmönvaihtimen mitoitukseen. Koska virtauskenttä ripaputkilämmönsiirtimessä ei ole selitettävissä yksinkertaisilla analyyttisillä ratkaisuilla, numeerista virtauslaskentaa (CFD) käytettiin lämmönvaihtimen lämmönsiirron ja painehäviön laskentaan erilaisille ripageometrioille. Laskentamalli vastasi yleisin osin kokeellisia tuloksia.

CFD laskennasta saatu tietomäärä tiivistettiin korrelaatioiden avulla yleisesti käytössä oleviksi lämmönsiirron ja painehäviön korrelaatioiksi. Jokaiselle geometrialle tehtiin sovite Nusseltin ja Eulerin luvuille sekä ripahyötysuhteelle Reynoldsin luvun funktiona. Lisäksi kaikki geometriat kattava yleinen korrelaatio tehtiin Nusseltin luvulle, Eulerin luvulle, Colburnin j-kertoimelle, Fanningin kitkakertoimelle sekä ripahyötysuhteelle.

Geometrioille tehdyillä korrelaatioilla jokaisesta geometriasta mitoitettiin lämmönvaihdin, jonka lämmönsiirtoteho ja painehäviö olivat yhtä suuret. Tapauksia verrattiin referenssigeometriaan, jotta saatiin selvitettyä geometrian vaikutusta lämmönvaihtimen kokonaismassaan, -tilavuuteen ja likiarvoiseen hitsaustuntimäärään. Ripavälin havaittiin olevan merkittävin parametri lämmönsiirtimen mitoituksessa. Toiseksi tärkeimmät parametrit olivat putkivälit ja rivan paksuus. Vähiten merkittävät parametrit olivat ripojen välykset ja rivan virtaussuuntainen railo.

PREFACE

This thesis was made for Alfa Laval Aalborg Rauma office to get insight on the effect of the finned tube geometry on the heat transfer and pressure drop of the heat exchanger.

I would like to thank Manager of the Cruise Key Customers Sales Pasi Aaltonen for offering a very interesting and challenging subject for this thesis. I would also like to thank Alfa Laval Aalborg for support regarding this thesis and for offering a great and inviting working environment.

I would also like to thank Turo Välikangas for great suggestions regarding the thesis structure and content. The discussions with Turo of the CFD and thermal-hydraulic dimensioning practices were also teaching.

Last but not least, I would also like to thank Iida Päivömaa for offering some other things to think about in addition to this thesis.

CONTENTS

List of Figures

List of Tables

NOMENCLATURE

Symbols

$\dot{m}$	Mass flow, $\frac{kg}{s}$
$\dot{V}$	Volumetric flow rate, $\frac{m^3}{s}$
$\dot{W}_{pumping}$	Pumping power, W
$\sigma_{loss} = \frac{S_T - D}{S_T}$	Modified contraction ratio, $-$
a	Dimensionless fin height for fin efficiency, $-$
A_c	Minimum flow cross-section, m^2
A_h	Heat transfer area, m^2
$A_{contact}$	Fin contact area with the tube, m^2
A_{fr}	Frontal area, m^2
b	Dimensionless heat conductivity for fin efficiency, $-$
c_p	Specific heat capacity at constant pressure, $\frac{J}{kgK}$
D'	Cross-diffusion in ω transport equation, $\frac{W}{m^3}$
D_h	Hydraulic diameter, m
Eu	Euler's number, $-$
F	Correction factor for logarithmic mean temp, $-$
f	Fanning friction factor, $-$
f_a	Factor accounting for the tube bundle configuration, $-$
f_b	Friction coefficient for tube bundle, $-$
f_D	Darcy's friction factor, $-$
g	Gravity acceleration, $\frac{m}{s^2}$
G'	Production term in turbulence equations, $\frac{W}{m^3}$
$G = \rho V_{max} = \frac{\dot{m}}{A_c}$	Mass flux at the smallest cross-section, $\frac{kg}{m^2 \times s}$
Gr	Grashof number, $-$
h	Heat transfer coefficient, $\frac{W}{m^2 K}$
I	Turbulence intensity, %
I_i	Modified Bessel function, first kind, i-th order, $-$
j	Colburn j-factor, $-$
k	Thermal conductivity, $\frac{W}{mK}$
K_c	Exit loss coefficient, $-$
K_e	Entrance loss coefficient, $-$
K_i	Modified Bessel function, second kind, i-th order, $-$
k_T	Turbulent kinetic energy, $\frac{m^2}{s^2}$
L	Channel length, m
N_L	Tubes in longitudinal direction, $-$
N_T	Tubes in transverse direction, $-$
Nu	Nusselt number, $-$
Nu_{bundle}	Nusselt number of a tube bundle, $-$
$Nu_{l,\psi}$	Combined Nusselt number, $-$
$Nu_{l,laminar}$	Laminar Nusselt number, $-$
$Nu_{l,turbulent}$	Turbulent Nusselt number, $-$
P	Fin pitch, m
p	Pressure, Pa

Pr	Prandtl number, $-$
Q	Total heat transfer, W
q	Heat flux, $\frac{W}{m^2}$
R	Thermal resistance, $\frac{K}{W}$
Re	Reynolds number, $-$
$Re_{\psi,l}$	Tube bundle Reynolds number, $-$
Ri	Richardson number, $-$
S'	Source term in turbulence equations, $\frac{W}{m^3}$
s_f	Fin thickness, m
s_w	Tube wall thickness, m
T	Temperature, K
U	Overall heat transfer coefficient, $\frac{W}{m^2K}$
u	Velocity component, $\frac{m}{s}$
u_*	Friction velocity, $-$
V	Velocity, $\frac{m}{s}$
x_c	Characteristic dimension, m
x_i	Cartesian coordinates (x, y, z), m
x_{crit}	Critical distance from the leading edge, m
y	Distance of cell centroid normal to a nearest wall, m
Y'	Dissipation term in turbulence equations, $\frac{W}{m^3}$
y^+	Dimensionless wall distance, $-$
z	Elevation tangential to the gravity acceleration, m
Greek symbols	
$\alpha = \frac{k}{\rho c_p}$	Thermal diffusivity, $\frac{m^2}{s}$
β	Coefficient of thermal expansion, $\frac{1}{K}$
χ	Pressure drop correction for tube bundle, $-$
Δ	Difference, $-$
δ	Boundary layer thickness, m
Δ_f	The slit width, m
δ_f	The gap between fins, m
ϵ	Dissipation of turbulent kinetic energy, $\frac{m^2}{s^3}$
η_0	Surface efficiency, $-$
η_f	Fin efficiency, $-$
Γ	Effective turbulent diffusivity, $\frac{m^2}{s^2}$
μ	Dynamic viscosity, $\frac{kg}{ms}$
$\nu = \frac{\mu}{\rho}$	Kinematic viscosity, $\frac{m^2}{s}$
ω	Specific rate of dissipation, $\frac{m^2}{s^2}$
ψ	Void fraction of the tube bundle, $-$
ρ	Density, $\frac{kg}{m^3}$
$\sigma = \frac{A_c}{A_{fr}}$	Contraction ratio, $-$
τ	Shear stress, Pa
φ	Geometric parameter for the fin efficiency, $-$
φ'	Geometry parameter for fin efficiency, $-$
Subscripts	
1	At the point 1
2	At the point 2

∞	Free stream conditions
D	Tube diameter as the characteristic dimension, $-$
D_h	Hydraulic diameter as the characteristic dimension, $-$
$eval$	Evaluation conditions
i	First Cartesian coordinate direction
i	Inner
j	Second Cartesian coordinate direction
m	Mean
max	Maximum
min	Minimum
n	Sum index
o	Outer
w	At solid surface
x_c	Characteristic dimension, m

1. INTRODUCTION

Currently, the trend is to increase the energy and material efficiency at all fields. Many times the increased energy efficiency results into higher material costs. If a competitive design is to be achieved, the design has to be optimised so that provides highest energy efficiency possible while requiring minimum material and working hours to be produced.

In this study, a heat recovery from the exhaust gas of the diesel engines or gas turbines with finned tube heat exchangers is considered. Waste heat recovery is an easy way to increase the total efficiency of the power plant by utilising the thermodynamically low grade heat, for example, in air or feed-water preheating. (Thulukkanam, 2013, Chapter 6.1.4) The slightly higher grade heat may also be used, for example, as a process heat or in producing super-heated steam which may be used in a steam turbine to produce electricity. To utilise the waste heat from the exhaust gas, a heat transfer surface has to be used to transfer the heat from the exhaust gas into, for example, water. The water may evaporate in the heat exchanger, producing steam, which can be used as process heat and turbine feed, or alternatively the warm water may directly be used in district heating applications.

The choice of the heat exchanger can be quite arbitrary but in the applications where the fluid to which the heat is transferred to is at high pressure, finned tubes are a good choice due to the fact that the tubes are able to withstand pressure with a minimal material requirements (Shah and Sekulic, 2003, Chapter 1.5.3.2.). The fin pitch may easily be varied to account for different fouling characteristics. The in-line arrangement provides uninterrupted flow passage for efficient soot blowing while the staggered arrangement maximises the heat transfer for given mass and volume. Additionally, the finned tubes may even be used in corrosive applications as the fin and tube thicknesses may be varied for corrosion allowance. This makes the finned tube heat exchangers suited for different operation situations even with harsh and fouling media. (Thulukkanam, 2013, Chapter 4.1.3.)

The heat transfer mechanisms in the finned tubes can be roughly divided as followed. At the finned side, the heat from exhaust gas is transferred to the fin surface by combined advection, conduction and radiation. In the fin, the heat is conducted to the tube inner wall driven by temperature gradients. At the tube inner wall, the heat is transferred to the medium inside with combined advection and conduction.

Even though the heat transfer is the primary concern in the waste heat recovery, the hydraulic performance of the heat exchanger is usually just as important. The pressure drop caused by heat exchanger increases the operation costs by requiring

more pumping power. The pumping power to overcome the friction may be provided with a fan, diesel engine or gas turbine in typical heat recovery applications and it directly increases the electricity consumption of the heat recovery. As the electricity is thermodynamically the highest quality energy (Cengel, 2008, Chaper 3.1), there are trade-offs between the heat transfer characteristics and pressure drop in the heat exchanger core. The high velocity heat exchangers produce compact and cheap heat exchangers with high pressure drop while the low velocity heat exchangers produce bulkier and heavier heat exchangers with low pressure drop.

2. THERMAL-HYDRAULIC DIMENSIONING

Thermal-hydraulic dimensioning means a simultaneous dimensioning for the heat transfer and pressure drop according to the boundary conditions. Usually heat transfer is increased in the power of less than one as the velocity is increased while the pressure drop increases in power of one to two (Kays and London, 1964, Chapter 1). Thus the allowed pressure drop or pumping power limits the maximum heat exchanger core velocity and heat transfer capacity for a given set of heat exchanger dimensions and surface types.

To increase the total heat transfer capacity on the gas side in accordance with the allowed pressure drop, one has to increase frontal area of the heat exchanger to lower the velocity and pressure drop while simultaneously making the heat exchanger core slightly longer. This, however, decreases the heat transfer coefficient at surfaces which results in a heat exchanger with more surface area for a given heat duty. (Kays and London, 1964, Chapter 1) A proper dimensioning for the pressure drop has a major impact on the heat exchanger feasibility and the pressure drop should always be dimensioned as close to the allowed pressure drop as possible while accounting the possible off-design operation (Shah and Sekulic, 2003, Chapter 1.4.1).

Another approach to increase heat duty for a given heat exchanger core volume is to use more compact heat surfaces to increase the heat transfer rate within the heat exchanger core. The increased heat transfer surface area density increases the pressure drop for a given velocity and outer dimensions. However, as the pressure drop decreases in higher power than heat transfer with velocity, decreasing the velocity decreases the pressure drop more than the heat transfer. A more compact design with lower velocity usually leads into a heat exchanger with larger frontal area. This combined with the increased heat transfer surface area usually leads into a higher heat transfer rate for given outer dimensions. (Kays and London, 1964, Chapter 1)

To calculate heat transfer and pressure drop for a surface type, friction factor and heat transfer coefficient has to be known. As the friction factor and heat transfer coefficient are usually tedious or impossible to solve from the governing equations as the boundary conditions are usually not known, correlations for them has been developed from experiments and CFD to simplify the dimensioning process. The correlations for heat transfer and pressure drop are usually presented with dimensionless Reynolds (2.1) and Prandtl (2.2) numbers. Reynolds numbers is a measure of the ratio of the inertial and viscous forces in a fluid flow and flows with a similar Reynolds number behave similarly. The Prandtl number is a measure of viscous and

thermal diffusion and it relates the thermal and momentum diffusion and boundary layer thicknesses in a laminar flow. (Shah and Sekulic, 2003, Chapter 7.2)

$$Re_{x_c} = \frac{\text{inertial forces}}{\text{viscous forces}} = \frac{\rho V x_c}{\mu} \tag{2.1}$$

$$Pr = \frac{\text{viscous diffusion rate}}{\text{thermal diffusion rate}} = \frac{\nu}{\alpha} = \frac{c_p \mu}{k} \tag{2.2}$$

In the equations (2.1) and (2.2) ρ is the density, V is the velocity, x_c is the characteristic dimension, μ is the dynamic viscosity, ν is the kinematic viscosity, α is the thermal diffusivity and c_p is the specific heat capacity.

The characteristic dimension used in engineering correlations is typically chosen to match the length scale of the problem. For a flat plate, the characteristic dimension is the distance from the plate leading edge. For internal flow, it is the diameter of the tube while for channels a hydraulic diameter is typically used. For more complex geometries, the choice of characteristic dimension is more arbitrary, and an useful definition for extended surfaces is given by Kays and London (1964, Chapter 1). In this study the characteristic dimension is chosen as the tube diameter for all purposes except for the universal correlations, where the hydraulic diameter as the characteristic dimension was found to correlate with the CFD data the best.

$$D_h = \frac{4 A_c L}{A_h} \tag{2.3}$$

In the equation (2.3) A_c is minimum flow cross-section in the channel, A_h is total heat transfer area and L is the length of the passage. This characteristic dimension is only used in the Appendix I.

As there are two frequently used friction factors used in the literature, the friction factor used in this study is the Fanning friction factor unless otherwise noted. The Darcy's friction f_D factor is four times higher than the Fanning friction factor f (Shah and Sekulic, 2003, Chapter 7.2).

As there are effectively two heat surfaces in the compact heat exchangers, one for the finned side and one inside the tubes, the finned side is hereafter referred as outer surface and the surface inside tubes is referred as inner surface. The media in the heat exchanger may also vary depending on the application but in this study the outer surface is in contact with air while the inner surface is in contact with saturated water.

2.1 Heat transfer

As the fluid flows through heat exchanger core it changes temperature due to heat transfer at the heat exchanger surface according to the equation (2.4) (Incropera et al., 2011, Chapter 8.3). The specific heat capacity for the temperature range in this study may be approximated to vary linearly which means that the average of the specific heat capacity may be used instead of integration.

$$Q = \int_{T_1}^{T_2} c_p \dot{m} dT \approx c_{p,m} \dot{m} (T_2 - T_1) \tag{2.4}$$

The equation for heat transfer is given in the equation (2.5). The equation can also be derived by using the equations, (2.4) and (2.11) and (2.12), and by multiplying both sides with the heat transfer surface area. As the temperature change of the fluid due to the heat transfer for internal flows is exponential, a logarithmic mean temperature has to be used as correct temperature difference in the equation (2.5) (Incropera et al., 2011, Chapter 8.3.3.). In the equation (2.5) the F is a correction factor for heat exchanger type. The correction factor for evaporating heat exchangers in this study is 1 as the medium inside tubes can be considered to be isothermal (Thulukkanam, 2013, Chapter 2.2.3.3.2).

$$Q = FUA_h \Delta T_{lm} \tag{2.5}$$

The logarithmic mean temperature ΔT_{lm} is defined by the equation (2.6). In the equation (2.6) the ΔT_1 and ΔT_2 is the temperature difference of the fluids at the inlet and the outlet of the heat exchanger respectively. (Incropera et al., 2011, Chapter 8.3.3.) Considering the heat exchangers in this study, where the temperature inside the tubes is constant, the $\Delta T_i = T_i - T_w$ and $\Delta T_o = T_o - T_w$.

$$\Delta T_{lm} = \frac{\Delta T_i - \Delta T_o}{\ln\left(\frac{\Delta T_i}{\Delta T_o}\right)} \tag{2.6}$$

For a typical non-regenerative heat exchanger with the two mediums divided by a wall the overall heat transfer coefficient in the equation (2.5), defined for the outer surface, is given in the equation (2.7) and total heat transfer is given in the equation (2.5). (Incropera et al., 2011, Chapter 8.2) The formulation is developed for the outer surface but it could have been developed for the inner surface as well.

$$\begin{aligned} UA_{h,o} &= \left(\frac{1}{\eta_{0,o} h_o A_{h,o}} + \frac{s_w}{k A_{h,w}} + \frac{1}{\eta_{0,i} h_i A_{h,i}} \right)^{-1} \\ &= (R_o + R_w + R_i)^{-1} = \left(\sum_{i=1}^{\infty} R_n \right)^{-1} \end{aligned} \tag{2.7}$$

In the equation (2.7) the η_0, h and A_h are the surface efficiency, heat transfer coefficient and heat transfer area associated with inner and outer surfaces, respectively. The U is the overall heat transfer coefficient. The R_c is the thermal resistance which for convective boundary layer is given by the equation (2.8), for plane wall by the equation (2.9) and for pipe wall by the equation (2.10) (Incropera et al., 2011, Chapters 3.1 and 3.3). The surface efficiency η_0 is discussed more in-depth in the section 3.1 for finned tubes.

$$R = \frac{1}{\eta_0 h A_h} \tag{2.8}$$

$$R_w = \frac{s_w}{kA} \tag{2.9}$$

$$R_{w,pipe} = \frac{\ln\left(\frac{D_o}{D_i}\right)}{2\pi L k} \tag{2.10}$$

By limiting the domain of interest to the tube wall i.e. setting the tube wall to constant temperature, the inner surface resistance terms drops out. Additionally, by dropping out the wall conduction term, the conduction effect will be encompassed in the product of heat transfer coefficient and surface efficiency. With aforementioned simplifications the equation (2.7) is simplified to (2.11).

$$U = \eta_{0,o} h_o \tag{2.11}$$

Heat transfer in is based on governing equations of the fluid dynamics (4.1), (4.2), (4.3) and thermodynamics but to get useful relations for engineering heat transfer applications, Newton's law of cooling (2.12) for convection is utilised. While the governing equations can be solved at least numerically, the Newtons law of cooling hides all the complexities of the convective heat transfer in the convective heat transfer coefficient, which is a function of the fluid properties and the flow, which in turn are function of the geometry and boundary conditions. Usually the heat transfer coefficient is given with a dimensionless Nusselt number (2.13) or Colburn j-factor (2.14) where the h is the heat transfer coefficient and k is the heat conductivity. (Incropera et al., 2011, Chapter 8.2)

$$q = h(T_\infty - T_w) \tag{2.12}$$

$$Nu_{x_c} = \frac{\text{convective heat transfer}}{\text{conductive heat transfer}} = \frac{hx_c}{k} \tag{2.13}$$

$$j = \frac{Nu_{x_c}}{Re_{x_c} Pr^{\frac{1}{3}}} \tag{2.14}$$

With the total heat transfer rate, surface area and surface efficiency, the convective heat transfer coefficient can be calculated from the equations (2.11) and (2.5). Respectively, with the correlations obtained from the CFD solutions, by knowing the surface area, outer heat transfer coefficient and the surface efficiency, the total heat transfer rate can be calculated.

When calculating the heat transfer rate of the heat exchanger, the heat transfer coefficient in the equation (2.11) has to be known. Typically correlations for the Nusselt number (2.13) or Colburn j-factor (2.14) for the given geometry are used in calculating the heat transfer coefficient. The Nusselt number or Colburn j-factor are usually correlated with least squares empirical correlations with only variables being non-dimensional Reynolds number, Prandtl number and some geometry dependant constant. As the definition of the Reynolds number, Nusselt number and Prandtl number includes fluid properties which vary with temperature, a correct evaluation temperature or some temperature correction method has to be used to account for variation in properties in boundary layer. (Incropera et al., 2011, Chapter 7.1) In this study the evaluation temperature is chosen to be $T_{eval} = T_w + \Delta T_{lm}$. While these correlations are extremely useful from an engineering point of view, a special care should be taken for the applicability of the aforementioned correlations.

2.2 Pressure drop

Total static pressure change in a heat exchanger core can be divided into a pressure changes due to an acceleration and a change in the static head, and to pressure losses due to entrance and exit losses, viscous drag and form drag. (Shah and Sekulic, 2003, Chapter 6.2) Depending on the geometry and fluid properties some of these might be neglected but especially in the gas heat exchangers all these but static head have some impact on the total pressure drop across the heat exchanger core. Of these the acceleration and the static head change are recoverable while the inlet and outlet losses, viscous drag and form drag are associated with irreversible processes and they cannot be recovered.

The static pressure change due to acceleration arise when the flow has to accelerate because of the change in the cross-sectional area or fluid density. As the fluid accelerates the pressure energy converts into kinetic energy and vice versa. The static head pressure change arises due to gravity acceleration. Both these recoverable

pressure changes can be solved from the well known Bernoulli energy equation (2.15) which is only valid along the streamlines. The static head term is the first one on the right hand side while the acceleration term is the second one on the right hand side. The g in the equation is gravity acceleration and z is the elevation. Other losses may be accounted with loss terms but then one has to know inlet and outlet loss factors, friction coefficient and form drag coefficient. (Shah and Sekulic, 2003, Chapter 6.2)

$$p_1 - p_2 = \rho g(z_2 - z_1) + \frac{1}{2}\rho(V_2^2 - V_1^2) \tag{2.15}$$

Kays and London has given an equation (2.16) for friction factor in the heat exchanger core which accounts for all of the aforementioned pressure change components but static head pressure decrease. The friction drag and form drag has, however, been summed into the Fanning friction factor f. (Kays and London, 1964, Chapter 1). In this study, the equation (2.16) was used in calculating the Fanning friction factor with the value of the pressure drop from the CFD solutions.

$$\begin{aligned}\Delta p = \frac{G^2}{2\rho_i}\Bigg[&(K_e + 1 - \sigma^2) + 2\left(\frac{\rho_i}{\rho_o} - 1\right) \\ &+ f\frac{A}{A_c}\frac{\rho_i}{\rho_m} - (1 - \sigma^2 - K_c)\frac{\rho_i}{\rho_o}\Bigg]\end{aligned} \tag{2.16}$$

In the equation (2.16) $G = \rho V_{max} = \frac{\dot{m}}{A_c}$ is the mass flux at the smallest cross-section, K_e and K_c are the loss coefficients associated with the entrance and the exit respectively, $\sigma = \frac{A_c}{A_{fr}}$ is the contraction ratio of the heat exchanger core. The ρ_i, ρ_o and ρ_m corresponds to the densities at inlet, outlet and evaluation temperature respectively.

As the pressure drop is usually the value of the interest the friction factor has to be obtained in some way. Usually the friction factor is given as a Reynolds number based correlation for either Fanning friction factor (2.18) or Euler number (2.17) depending on the application. The Δp is the pressure drop and τ_w is the skin friction. (Shah and Sekulic, 2003, Chapter 7.2)

$$Eu = \frac{\text{pressure drop}}{\text{dynamic pressure}} = \frac{\Delta p}{\frac{1}{2}\rho V^2} \tag{2.17}$$

$$f = \frac{\text{wall shear}}{\text{dynamic pressure}} = \frac{\tau_w}{\frac{1}{2}\rho V^2} = \frac{f_D}{4} \tag{2.18}$$

3. FINNED TUBES

A feasible way to increase the heat transfer surface of a tube bank heat exchanger is to add fins to the tubes resulting in a finned tube heat exchanger. The fins can be used in both inner and outer surface of the tubes, but in this study only ones on the outer surface are considered. By using fins outer surface of the tubes, the heat transfer area outside of the tubes can be increased without increasing the heat exchanger core volume resulting in a higher heat transfer surface per volume. Some finned tubes used in waste heat recovery applications are shown in Fig. 3.1. The fins can be of any shape and size but only the single gilled tubes (left) and double gilled tubes (middle at back) are considered in this study. This type of gilled tubes are hereafter referred as H-type finned tubes.

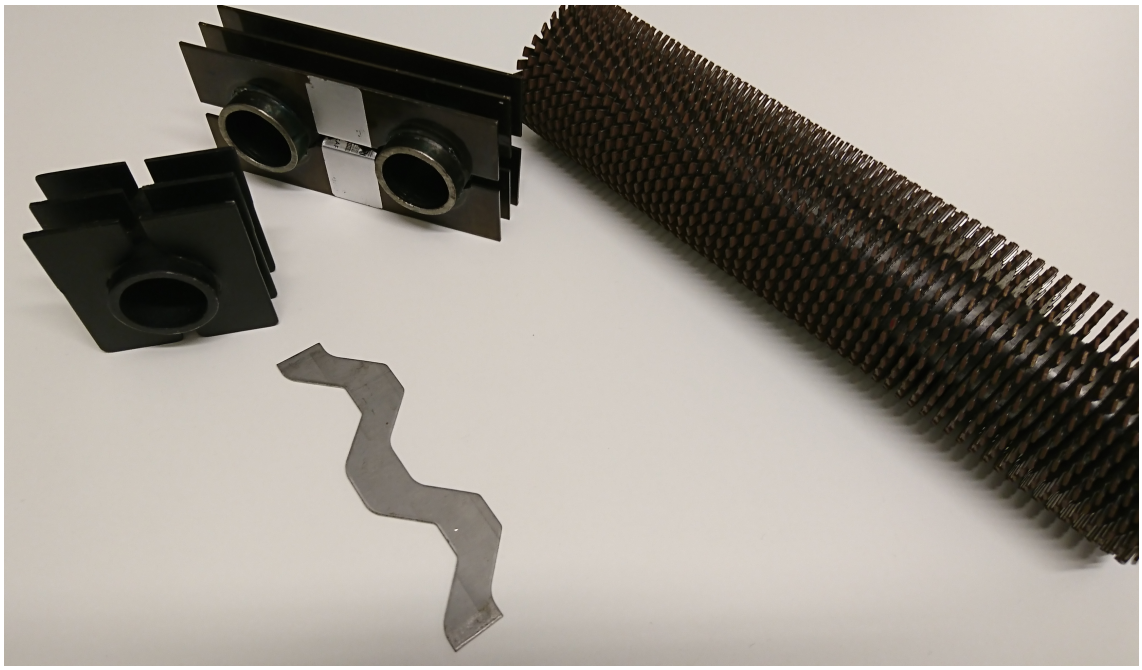

Figure 3.1. *Some typical finned tubes.*

This kind of construction is usually beneficial when the outer heat transfer coefficient is much lower than the inner heat transfer coefficient. This is the case, for example, in the evaporating waste heat recovery applications where the outer heat transfer coefficient dominates the overall heat transfer coefficient (Incropera et al., 2011, p. 710). The finned surface is utilised at the side of lower heat transfer coefficient which decreases outer thermal resistance according to the equation (2.7). (Shah and Sekulic, 2003, Chapter 1.4)

3.1 Fin efficiency

The fin efficiency is the ratio of the actual heat transfer to the ratio of the heat transfer of the isothermal fins. In fin systems, the heat transfer is usually calculated with an assumption of isothermal fin, and the variation in the fin surface temperature due to limited conductivity is then corrected with a fin efficiency. As the fin temperature is an arbitrary function of the geometry, the material properties and the flow field, a simple universal fin efficiency formulation, for all geometries with complex flow fields, cannot be developed. However, there are empirical correlations for different geometries for estimating the fin efficiency. The definition of the fin efficiency is given in the equation (3.1).

$$\eta_f = \frac{Q}{Q_{max}} = \frac{\int_{A_h} h(T_x - T_{fin}) dA_h}{\int_A h(T_x - T_{tube,i}) dA_h} \tag{3.1}$$

The fin efficiency η_f can be calculated for example by relation given by Schmidt in the equations (3.2) and (3.3) (VDI e. V., 2010, Chapter M1). The solution procedure is iterative as the overall heat transfer coefficient has to be known. The T_{fin} is the fin surface temperature at given position, the T_x is the evaluation temperature of the outer medium at the same position and the T_w is the fin base temperature while the s_f is the fin thickness.

$$\eta_f = \frac{tanh(X)}{X} \tag{3.2}$$

$$X = \varphi \frac{D}{2} \sqrt{\frac{2U}{k s_f}} \tag{3.3}$$

The φ parameter varies with geometry and for rectangular fins in in-line tube bank it is given by the equations (3.4) and (3.5). Other geometries may be found from (VDI e. V., 2010, Chapter M1). The S_T and S_L are transverse and longitudinal pitches respectively while the δ_f is the gap between fins.

$$\varphi = (\varphi' - 1)\left[1 + 0.35 \ln \varphi'\right] \tag{3.4}$$

$$\varphi' = 1.28 \frac{S_T - \delta_f}{D} \sqrt{\frac{S_L - \delta_f}{S_T - \delta_f} - 0.2} \tag{3.5}$$

However, when using CFD for the optimisation, the evaluation of the integrals in the equation (3.1) is quite straightforward and the fin efficiency in this study is the actual fin efficiency in each case at given boundary conditions. The CFD fin

efficiency is compared against the given correlation in the validation section.

Once the fin efficiency is known, a total surface efficiency may be calculated from the equation (3.6) which may be used in the equation (2.7) for calculating the total heat transfer for a fin system in question. The A_{tube} is the heat transfer area of the tube while the A_{fin} is the heat transfer area of the fin. (Schmidt, 1949)

$$\eta_0 = \frac{1}{A_h}(A_{tube} + \eta_f A_{fin}) \tag{3.6}$$

3.2 Boundary layers associated with the finned tubes

As the fins in a finned tube heat exchangers are in fact a flat plates forming a channel between two fins it is beneficial to examine couple of analytical and empirical solutions for flat plate boundary layers and internal flows as they may give some insight into the nature of the boundary layers and flow development in the finned tube heat exchangers. At the developing region, it might be possible to approximate the heat transfer coefficient and friction factor with flat plate boundary layer solutions. If the flow length is long enough, the flow may become fully-developed and the heat transfer coefficient and friction factor may be approximated with the fully-developed channel flow correlations. However, as the tubes causes recirculation regions behind the tubes the heat transfer coefficient might vary quite much locally depending on the chosen geometry.

When the free stream enters a zone with a solid surface, the surface starts to decelerate the free flow near the walls due to the wall friction and boundary layers begin to grow due to the momentum transfer in the vicinity of the walls. Momentum boundary layer can be described as a zone where the velocity is less than 99 % of the free stream velocity. Analogously, when the free stream at a temperature enters a zone where the wall is in a different temperature a thermal boundary layer develops due to the heat transfer between wall and free stream. Thermal boundary layer can be described as a zone where the temperature difference is less than 99 % of the temperature difference between the free flow and the wall. (Shah and Sekulic, 2003, Chapter 7.1)

Boundary layer is zone in a free shear layer or in a vicinity of a wall where the effects of the viscosity are dominating. All interesting phenomena from the thermal-hydraulic point of view such as skin friction and heat transfer occur due to and within the boundary layers as the gradients of the velocity and temperature are largest there. The flow outside of boundary layers can be regarded as inviscid and isothermal and it does not affect the friction or heat transfer unless free stream accelerates or decelerates (Shah and Sekulic, 2003, Chapter 7.1). However, in this study almost the whole heat exchanger core is one big boundary layer. As the mathematical formulation of the boundary layers can be quite complex, the usual solutions are given for the constant heat flux at the wall or for the constant wall temperature. While the boundary layer theory may be useful in solving simple flow

cases where the boundary conditions can be given in mathematical, form they may not be very accurate in solving complex three dimensional flows with flow separation like the ones in this study.

3.2.1 Flat plate boundary layer

The boundary layer in flat plates can be either laminar or turbulent in nature depending on the length from the leading edge and the instabilities in the free flow. If the distance from the leading edge is small, the flow is more likely laminar and all fluid particles flows strictly parallel to the flat plate and farther in downstream the flow becomes turbulent. Turbulence is associated enhanced mixing of the momentum and energy with strong random fluctuations in every direction. However, if there are instabilities in the free flow, the flow may become turbulent in the start of the fin leading edge. (Schlichting and Kestin, 1979, p. 11 - 19)

For a laminar boundary layer at flat plate the local momentum boundary layer thickness can be approximated with Blasius solution (3.7) (Blasius, 1908). The local Nusselt number for isothermal and constant heat flux flat plate laminar boundary layer was derived by Pohlhausen (1921) and Gauler (1974) and is given by the equation (3.8) (VDI e. V., 2010, Chapter G4). The local Fanning friction factor for turbulent plate is given by the equation (3.9) (Cengel and Cimbala, 2013, Table 10.4). The characteristic length in the flat plate equations is the distance from the leading edge.

$$\delta = 5.0\sqrt{\frac{\nu x_c}{V_\infty}} \tag{3.7}$$

$$Nu_{x_c} = \begin{cases} 0.332 Re_{x_c}^{\frac{1}{2}} Pr^{\frac{1}{3}} \text{ for isothermal} \\ 0.460 Re_{x_c}^{\frac{1}{2}} Pr^{\frac{1}{3}} \text{ for constant heat flux} \end{cases} \tag{3.8}$$

$$f = \frac{0.664}{Re_{x_c}^{\frac{1}{2}}} \tag{3.9}$$

The local momentum boundary layer thickness for turbulent flat plate flow, derived from the $\frac{1}{7}$ power-law velocity profile and wall shear from turbulent pipe flow, is given by the equation (3.10) (Schlichting and Kestin, 1979). The local Fanning friction factor for a turbulent flat plate boundary layer is given by the equation (3.12) Schlichting and Kestin (1979). For a turbulent flat plate boundary layer, the local Nusselt number, derived from the skin friction (3.12) with Chilton-Colburn analogy, is given by the equation (3.11) (Incropera et al., 2011, Chapter 7.2.2.).

$$\delta = 0.37 \frac{x}{Re_{x_c}^{\frac{1}{5}}} \tag{3.10}$$

$$Nu_{x_c} = 0.0296 Re_{x_c}^{\frac{4}{5}} Pr^{\frac{1}{3}} \tag{3.11}$$

$$f = \frac{0.0592}{Re_{x_c}^{\frac{1}{5}}} \tag{3.12}$$

The most notable features of the laminar solutions is the inverse square root dependence of the boundary layer thickness and friction factor and the square root dependence of the Nusselt number while for turbulent flows the dependence is in the fifth root. It is easy to see from correlations for laminar and turbulent flat plate boundary layers that the boundary layer growth for turbulent boundary layer is much faster than for laminar boundary layer. As a result of the enhanced turbulent mixing due to turbulent eddies, the friction factor and the Nusselt number are also higher for turbulent flow. It should, however, be noted that the error of the turbulent correlations may be as high as 25 % depending on turbulence and surface roughness. (Incropera et al., 2011, Chapter 7.2)

3.2.2 Fully-developed or developing channel flow

The Nusselt number for a fully-developed incompressible laminar pipe flow with constant fluid properties is 3.66 for constant heat flux and 4.23 for isothermal wall (Incropera et al., 2011, Chapter 8.4.1.). If the wall is not isothermal or constant heat flux the Nusselt numbers does not apply strictly. The Fanning friction factor for fully-developed laminar flow is given in equation (3.13) (Incropera et al., 2011, Chapter 8.1.3.).

$$f = \frac{16}{Re_{D_h}} \tag{3.13}$$

For fully-developed turbulent channel flow the Nusselt number can be approximated with a well known Dittus-Boelter correlation (3.14) (Incropera et al., 2011, Chapter 8.5). Another possibility is to use correlation (3.15) by Gnielinski (1976) which is regarded as a more accurate correlation (Incropera et al., 2011, Chapter 8.5). The Fanning friction factor in the equation can be approximated with fully-developed smooth wall solution (3.16) (Incropera et al., 2011, Table 8.4) or with Moody's chart (White, 2009, Figure 6.13).

$$Nu_{D_h} = 0.023 Re_{D_h}^{\frac{4}{5}} Pr^{\frac{1}{3}} \tag{3.14}$$

$$Nu_{D_h} = \frac{\frac{f}{2}(Re_{D_h} - 1000)Pr}{1 + 12.7\sqrt{\frac{f}{2}}(Pr^{\frac{2}{3}} - 1)} \tag{3.15}$$

$$4f = (0.79Re_{D_h} - 1.61)^{-2} \tag{3.16}$$

3.3 The effect of fins on the flow field

The boundary layer development in the case of the flat plate can be either laminar or turbulent depending on the Reynolds number and the level of turbulence at the leading edge The critical Reynolds number for low turbulence flow can be considered to be 5×10^5 after which the flow transitions into a turbulent flow. However, increased turbulence levels at the start of the flat plate lowers the critical Reynolds number and the turbulent boundary layer may form earlier. (Incropera et al., 2011, Chapter 7.2) A figure of the developing flat plate boundary layer is given in the Fig. 3.2.

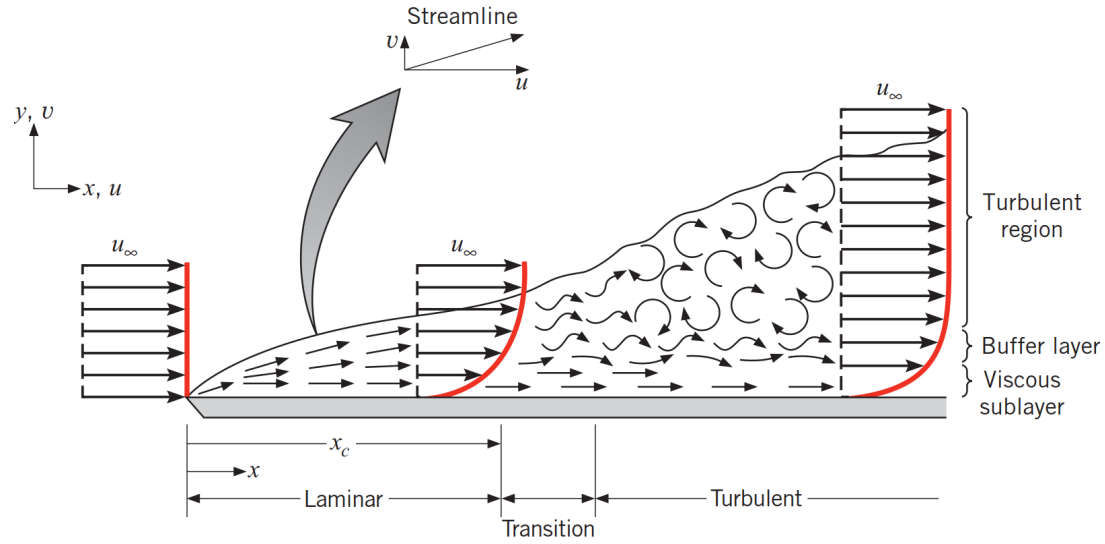

Figure 3.2. *Boundary layer development in external flow. (Incropera et al., 2011, Chapter 6.3)*

Rough estimation of the transition point to the turbulent boundary layer can be calculated from Reynolds number definition by using the critical Reynolds number to calculate point of transition x. For a low turbulence free stream a good approximation would be $Re_{x_{crit}} = 5\times10^5$. After the critical Reynolds number the boundary layer rapidly increases in thickness as a turbulent boundary layer is formed. (Incropera et al., 2011, Chapter 7.2)

If the fins are sufficiently long for the boundary layers at the opposing walls of the fin gap to merge, the flow becomes a fully-developed channel flow. This can happen either by the merging of the laminar boundary layers or if the turbulent boundary

layers have formed by the merging of the turbulent boundary layers. The critical Reynolds number for the boundary layer merger may be approximated by setting the boundary layer thickness as half of the gap between fins. In reality transition to fully developed channel flow occurs slightly at downstream as the flow has to accommodate to the transition from a flat plat flow to a channel flow. This, however, is a rather rough approximation and is likely to give an inaccurate transition point. (Incropera et al., 2011, Chapter 8.1) A figure of a simple developing internal flow is given in Fig. 3.3.

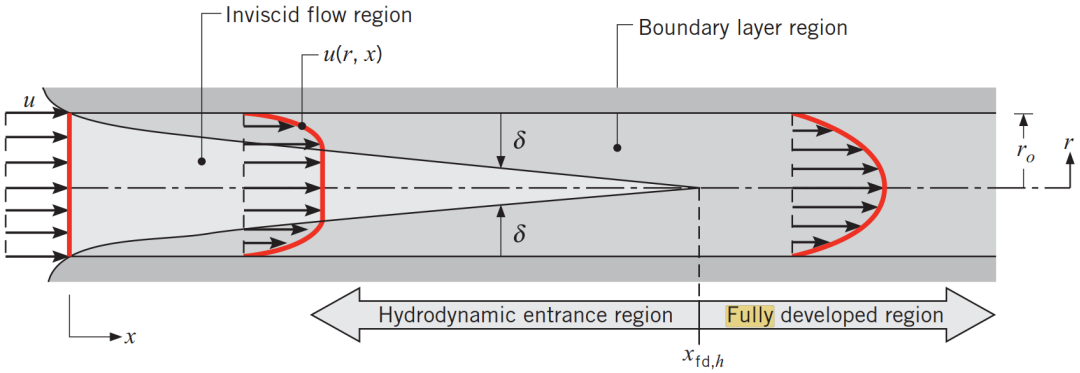

Figure 3.3. *Boundary layer development in internal flow. (Incropera et al., 2011, Chapter 8.1)*

The channel flow can be either turbulent or laminar depending on the Reynolds number. For a simple internal flows and Reynolds numbers below 2300 the flow is most likely laminar and for Reynolds numbers above 4000 the flow is most likely turbulent. (Incropera et al., 2011, Chapter 8.1) The fully-developed channel flows in this study are more likely to be turbulent than laminar as the Reynolds numbers are at range of 3000 - 40 000. However, as the flow in heat exchanger core is more complex than a simple flat plate boundary flow or a fully-developed channel flow, the Reynolds numbers given here might not be the best estimates of the nature of the flow.

As the fins are principally flat plates, some preliminary approximation of the heat transfer coefficient and friction factor may be gained from the flat plate correlations. The fin pitch is also the geometry which affect the hydraulic diameter the most in the finned tubes and as such the fin pitch is most likely determining the flow dynamics in the finned tubes.

3.4 The effect of the tubes on the flow field

In addition to supporting the whole heat exchanger and providing heat transfer area, the tube bank in the finned tube heat exchangers affects the flow dynamics by channelling the flow between the tubes. Thus the tube bank accelerates and decelerates the flow as the cross-sectional area normal to the flow changes in the heat exchanger core. A simplified flow field in the tube banks is shown in Fig. 3.4

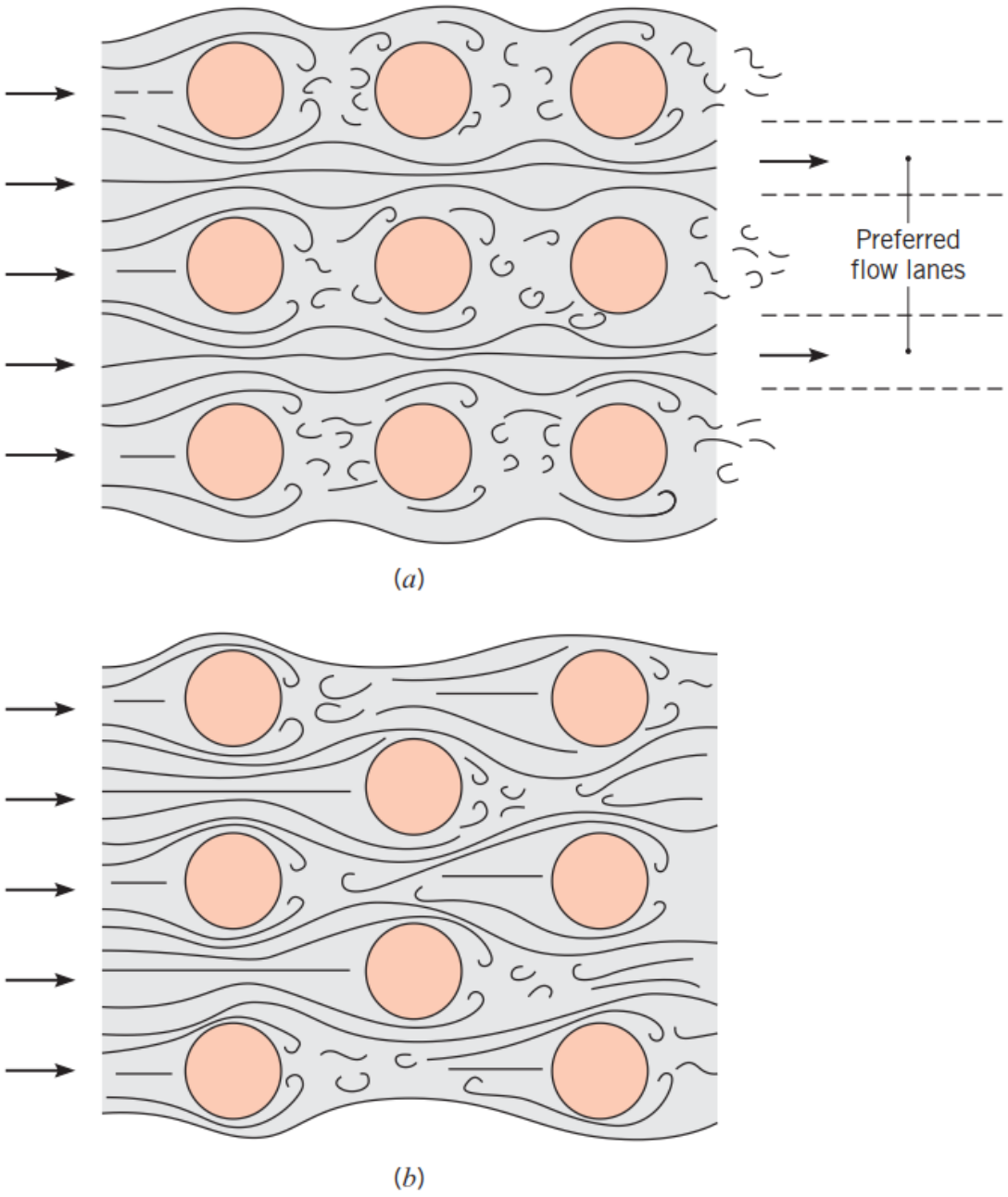

Figure 3.4. *Flow field in the tube banks. Figure a presents in-line and the figure b presents staggered tube bank (Incropera et al., 2011, Chapter 7.6)*

First, when the flow collides with the tube bank front, the main flow starts to accelerate due to the change in cross-sectional area according to the momentum equation (4.2). At the stagnation point all of the kinetic energy has been turned into pressure energy and the pressure is highest. The velocity is at maximum at about 90° from the stagnation point where the pressure gradient is approximately zero. After that, the free stream starts to decelerate and the pressure increases accordingly. After an arbitrary point where the momentum transfer is not strong enough compared to the positive pressure gradient associated with the deceleration,

the flow separates forming a recirculation zone behind the tube. For staggered tube banks this process occur at every tube lane but in in-line tube banks the effect is not as pronounced at the tubes in downstream as the main flow is not directly colliding with the every tube front. The flow separation and viscous drag at the tubes also increases turbulence downstream which results in increased heat transfer and friction factor. (Incropera et al., 2011, Chapter 7.6)

Gnielinski has given correlation (3.17) for both in-line and staggered tube arrangements. The weighted average of laminar and turbulent Nusselt number Nu_l is given by the equation (3.18). (VDI e. V., 2010, Chapter G7)

$$Nu_{bundle} = f_a Nu_{l,\psi} \tag{3.17}$$

$$Nu_{l,\psi} = 0.3 + \sqrt{Nu^2_{l,laminar} + Nu^2_{l,turbulent}} \tag{3.18}$$

The laminar and turbulent Nusselt numbers in the equation (3.17) are given by the equations (3.20) and (3.19). (VDI e. V., 2010, Chapter G7)

$$Nu_{l,turbulent} = \frac{0.037 Re^{\frac{4}{5}}_{\psi,l} Pr^{\frac{1}{3}}}{1 + 2.443 Re^{-\frac{1}{10}}_{\psi,l} (Pr^{\frac{2}{3}} - 1)} \tag{3.19}$$

$$Nu_{l,laminar} = 0.664 Re^{\frac{1}{2}}_{\psi,l} Pr^{\frac{1}{3}} \tag{3.20}$$

The characteristic Reynolds number for tube bundles is given by equation (3.21). (VDI e. V., 2010, Chapter G7)

$$Re_{\psi,l} = \frac{\rho V_{max} (\frac{\pi D}{2})}{\psi \mu} \tag{3.21}$$

The form factor f_A is given by the equation (3.22) for in-line arrangement and by the equation (3.23) for staggered arrangement. The $a = \frac{S_T}{D}$ and $b = \frac{S_L}{D}$ in the equations are the dimensionless transverse and longitudinal pitches respectively which are non-dimensionalised with tube diameter. (VDI e. V., 2010, Chapter G7)

$$f_{a,in-line} = 1 + \frac{0.7}{\psi^{\frac{3}{2}}} \frac{\left(\frac{b}{a} - 0.3\right)}{(\frac{b}{a} + 0.7)^2} \tag{3.22}$$

$$f_{a,staggered} = 1 + \frac{2}{3b} \tag{3.23}$$

The void fraction ψ in the in-line form factor equation is given by the equation (3.24). Correlation is valid for Reynolds numbers between 10 - 10^7. (VDI e. V., 2010, Chapter G7)

$$\psi = 1 - \frac{\pi}{4a} \text{ for } b \geq 1 \text{ and } \psi = 1 - \frac{\pi}{4ab} \text{ for } b < 1 \tag{3.24}$$

The correlation for pressure drop is given in the equation (3.25) but the f and χ has to be checked from (Incropera et al., 2011, Figure 7.14-15).

$$\Delta P = N_L \chi \frac{1}{2} \rho V_{max}^2 f_b \tag{3.25}$$

As shown above, the correlations for the tube bundle heat transfer and pressure drop are rather complicated, and no simple correlation was found from literature. Additionally, the correlations are most likely developed for turbulent flow typically encountered in engineering applications. The fins in finned tube heat exchangers may affect the simple tube bundle heat transfer and pressure drop due to boundary layer formation between fins and as such the equations given may not be of much use for finned tube heat exchangers.

3.5 Literature review

Before 90s, almost all studies done for finned tube heat exchangers were experimental studies as the geometry is quite complex to solve with simple analytical or semi-analytical calculations. After 90s, as the computational resources increased, it became possible to solve the Navier-Stokes (N-S) equations in engineering applications. After that, there have been a handful of conjugate heat transfer simulations studies for the finned tube heat exchangers, which allows the visualisation of the flow field and its effect on the local heat transfer to be studied more in detail. This would otherwise be very difficult or impossible with experimental methods. Almost all studies available for H-type finned tubes are for staggered tube bank arrangements while this study is only for in-line H-type finned tube banks and as such the literature review could be more thorough.

When going through studies by other authors it should be noted that the experimental methods are subject to multiple measurement and human errors which might negatively impact the accuracy of the observations. Especially the documentation of the experimental methods are crucial as the only way to reproduce the experiments are strictly similar operation conditions. (Webb, 2005) The CFD solutions are, in addition, subject to a numerical and modelling errors. Especially the modelling error due to turbulence modelling might have a quite high impact on the accuracy of the CFD solutions. (Versteeg and Malalasekera, 2007, Chapter 10) As such, all studies, whether experimental or CFD, should be compared with the possible errors in mind.

Chen et al. (2015) made a wind tunnel experiment for 6 different H-type finned tube geometries. Chen noted that the fin efficiency decreased as the air velocity in the smallest cross-section, fin height and fin width increased. Heat transfer coefficient was found to increase with an increase in fin pitch while the effect of the other parameters did not show a clear trend. The pressure drop was found to increase as fin pitch decreased and fin width and fin height increased. Chen also proposed correlations for Nusselt and Euler numbers and fin efficiency given in the equations (3.27) and (3.26) and (3.28). This study was also used as validation for the CFD model in this study.

$$Eu = \frac{\frac{dp}{N_L}}{\frac{1}{2}\rho V_{max}^2} = 19.14 Re_D^{-0.57} \left(\frac{S_L - \delta_f}{D} \right)^{1.32} \tag{3.26}$$

$$Nu_D = \frac{hD}{k} = 0.053 Re_D^{0.745} \left(\frac{D}{P} \right)^{-0.212} \left(\frac{S_L - \delta_f}{P} \right)^{-0.294} \left(\frac{S_T - \delta_f}{P} \right)^{0.155} \tag{3.27}$$

$$\eta_f = 7.41 V_{max}^{-0.12} \left(\frac{S_L - \delta_f}{D} \right)^{-2.32} \left(\frac{S_T - \delta_f}{D} \right)^{-0.198} \tag{3.28}$$

Schmidt has given a following correlation (3.29) for the Nusselt number for a finned tube bundles similar to ones in this study (VDI e. V., 2010, Chapter M1). It should be noted, however, that this correlation is an average of several cases and the cases are most likely highly turbulent. The correlation is checked against CFD solutions in validation section. The A_{tube} in the equation is the heat transfer area if there were no fins.

$$Nu_D = 0.20 Re_D^{0.6} \left(\frac{A_h}{A_{tube}} \right)^{-0.15} Pr^{\frac{1}{3}} \tag{3.29}$$

In book by Thulukkanam (2013, Chapter 4.4.) the effect of the various finned tube parameters are discussed. The in-line arrangement compared to the staggered arrangement provided about 70 % lower heat transfer and pressure drop for similar operation conditions. The first tube is found to have a 50-80 % higher heat transfer coefficient than the average for four rows in in-line arrangements. The tube pitch was found to have no effect on the heat transfer coefficient while the pressure drop increases with decreasing fin pitch.

Jin et al. (2013) has conducted a rather comprehensive multivariable CFD study of the H-type single gilled tubes with Reynolds number of 15 000. All Nusselt numbers in the article are the Nusselt numbers calculated with the convective heat

transfer coefficient h not overall heat transfer coefficient $U = \eta_0 h$. Yin has noted that increasing the fin thickness, while simultaneously keeping the fin pitch constant, increases the Nusselt number and pressure drop. According to Yin, this suggests that the fin thickness should be minimised to the manufacturing limit as long as heat transfer requirement is met. The fin slit was found to have a negligible effect on the all variables but with a trend that increased fin slit increases Nusselt number and decreases pressure drop. The fin height was varied by varying both transverse and longitudinal heights simultaneously. The increase in the fin pitch was noted to increase the Nusselt number and to decrease the pressure drop. The longitudinal and transverse pitches and fin height were studied quite differently by Yin than in this study. Yin increased the tube pitches while keeping the fin height constant or the fin height was varied while keeping the tube pitches constant. This resulted in a fin gaps of 0 and 25 mm and tube pitches between 84 mm and 130 mm. The increase in fin height increased the Nusselt number and pressure drop. The increase in transverse pitch was found to decrease the Nusselt number and the pressure drop. The increase in longitudinal pitch was found to increase both the Nusselt number and the pressure drop. The increase in the Reynolds number was found to increase the Nusselt number and to decrease the Euler number. The Euler number showed a significant rise at low Reynolds number. At high Reynolds numbers the Euler number converges to almost constant value. Yin also proposed correlations for Nusselt and Euler numbers, for a finned tube bank heat exchanger with 10 rows of tubes, given in the equations (3.30) and (3.31) which both were valid within 10 %. The study suggests that the actual value for Nusselt number should be about 10 % higher while the Euler number should be about 20 % higher for 6 tubes in row.

$$Nu_D = 1.66 Re_D^{0.585} \left(\frac{P}{D}\right)^{0.389} \left(\frac{s_f}{D}\right)^{0.165} \left(\frac{S_T}{D}\right)^{-1.108} \left(\frac{S_L}{D}\right)^{0.293} \left(\frac{L_f}{D}\right)^{-0.624} \left(\frac{\Delta_f}{D}\right)^{0.029} \tag{3.30}$$

$$Eu = 11.63 Re_D^{-0.157} \left(\frac{P}{D}\right)^{-0.693} \left(\frac{s_f}{D}\right)^{0.375} \left(\frac{S_T}{D}\right)^{-3.026} \left(\frac{S_L}{D}\right)^{-0.388} \left(\frac{L_f}{D}\right)^{1.835} \left(\frac{\Delta_f}{D}\right)^{-0.002} \tag{3.31}$$

Singh et al. (2017b) has studied the effect of the fin aspect ratio to the heat transfer and friction characteristics of the in-line finned tube heat exchanger. The first studied case was done to study the decrease of the fin tip thickness. In the second case, the aspect ratio of the fin was varied by increasing the fin base thickness while decreasing the fin tip thickness. The Nusselt number calculated from the overall heat transfer coefficient was found to decrease up to 15 % in the first case while for the second case it slightly increased for low aspect ratios. The Euler number was

found to decrease slightly for both cases with lower aspect ratios. The efficiency index $\frac{Nu}{Eu}$ was found to increase for both cases but for the first case it topped up while for the second case it kept increasing as the aspect ratio was increased. The area-goodness factor behaved in a similar manner. Simultaneously, the mass for the first case decreased almost 30 % while for the second case the mass decrease was almost 10 %.

Singh et al. (2017a) has also studied alternate fin shapes. The fin shapes in the study are rectangular, polynomial and sinusoidal fins. The polynomial and sinusoidal fins were found to have higher heat transfer and pressure drop for given inlet velocity. However, the transverse tube pitch was simultaneously decreased from 75 mm transverse pitch of rectangular fin to 70 mm transverse pitch for polynomial and sinusoidal fin. The lower flow area resulted in higher velocities in the heat exchanger core, which increased both heat transfer and pressure drop. As the heat exchanger core was dimensioned for equal total heat transfer and pressure drop with correlations developed in the study, the heat exchanger with polynomial and sinusoidal fins were found to have 2 % and 4 % lower masses, respectively.

Wang and Chi (2017) has done experiments on multiple plain finned tube cases with diameters lower than the finned tubes in this study. Wang showed that fin pitch does not have a noticeable effect on the friction factor and j-factor for a given Reynolds number. The tube diameter was also found to have a negligible effect on the friction factor and j-factor. Notably, the Fanning friction factor and Colburn j-factor were close to CFD solutions in this study.

Zhong et al. (2017) has studied the effect of geometric parameters, of the H-type finned tube, to the heat transfer and pressure drop characteristics with CFD. Nusselt and Euler number correlations were made for 120 cases with a response surface methodology. General agreement of the correlations were within 10 % of the CFD values.

Wang et al. (2016) has studied the effect of the geometric parameters, of the H-type finned tube heat exchanger with three tubes, to the heat transfer and pressure drop characteristics with CFD. The contribution of each parameter to the Colburn j-factor and Fanning friction factor was assessed with Taguchi method. The fin pitch, fin height and fin thickness was found to have the most significant effect in the area-goodness factor. In the end, the area-goodness factor (H.1) was optimised with Taguchi method by choosing the optimum value for each single parameter. The influence of the geometric parameters was found to be additive in regards of the area-goodness.

Jang et al. (1996) has studied the effect of the number of the tube rows in the pressure drop and Nusselt number of the in-line and staggered finned tube banks. The Nusselt number for the staggered tube banks was found to be considerably higher while the pressure drop was only slightly higher. The area averaged Nusselt number was found to decrease with the number of tube rows.

Erek et al. (2004) has studied the effect of the ellipticity of the tubes to the thermal-

hydraulic characteristics of the finend tubes. Unfortunately, the CFD model was developed for only one in-line tube row which by visual inspection seems to exaggerate the results compared to the case with more tubes in a row. However, the tubes with ellipticity of 0.7345 was found to perform the best compared to the circular tubes and tubes with ellipticity of 0.4064.

There has also been number of studies in the fin enhancement methods. Joardar and Jacobi (2008) studied the effect of winglets in the finned tube heat exchangers. The volume goodness given in the equation (H.2) with winglets was found to be higher at the whole Reynolds number range. Leu et al. (2004) studied the effect of the angle of the vortex generators in the flow structure and thermal-hydraulic performance with dye injection and CFD. Especially interesting phenomenon was the formation of the visible large scale vortices at the low Reynolds numbers range due to the interaction between the tubes and winglets which vanished into a smaller scale structures with the higher Reynolds numbers.

4. COMPUTATIONAL FLUID DYNAMICS

As the fluid dynamics is usually quite complex subject with complex geometries and flow patterns, the analytical solution is many times impossible. For some simple problems, with enough simplifications, useful solutions can be derived by directly solving the governing equations. However, as the mathematical methods for solving the non-linear partial differential equations are not sufficiently advanced to solve the N-S equations directly, the exact analytical solutions, in many cases, are impossible to solve. Fortunately, as the computational resources, numerical methods and turbulence models have evolved over the years, CFD allows solving many problems with exact solutions if correct boundary conditions and models can be provided. (Versteeg and Malalasekera, 2007, Chapter 3)

4.1 Governing equations

The air flow through the finned tube heat exchanger can be expressed with the three conservation equations. For a steady-state CFD calculation they are the conservation of mass (4.1), the conservation of momentum (4.2) (i.e. Navies-Stokes (N-S) equations) and the conservation of energy (4.3). The formal and rigorous derivation of these equations is available at the following reference (Peric, 2002, Chapters 1.3, 1.4 and 1.5).

$$\frac{\partial(\rho u_i)}{\partial x_i} = 0 \tag{4.1}$$

$$\frac{\partial(\rho u_j u_i)}{\partial x_j} = \rho f_i - \frac{\partial p}{\partial x_i} + \frac{\partial \tau_{ij}}{\partial x_j} \tag{4.2}$$

$$p\frac{\partial u_i}{\partial x_i} = \frac{\partial}{\partial x_i}\left(k\frac{\partial T}{\partial x_i}\right) + \tau_{ij}\frac{u_i}{x_j} \tag{4.3}$$

The equations are given in Einstein's Cartesian index notation with the i and j going from 1 to 3 presenting the Cartesian coordinates and the components of the vectors in a direction of x, y and z.

4.2 Turbulence

While the full N-S equations includes the effects of the turbulence, the solving of the all the turbulence length and time scales would require a very high grid density and short time scales. As the calculation time and memory consumption is roughly proportional to the cell count and inversely proportional to the time step size, solving the N-S equations for turbulent flows in engineering applications, without accounting for the effects of the turbulence with a simpler time-averaged turbulence models, requires very high computational resources. (Pope, 2009, Chapter 9) Although some turbulence models are said to be better, they usually perform well only in situations for which they have been optimised. Choosing the best turbulence model for the situation requires expertise in the fluid flow problem in question. (Versteeg and Malalasekera, 2007, Chapter 10.4)

The current turbulence models are based on an assumption that each fluctuating quantity can be divided into a mean and a fluctuating part ($\theta = \overline{\theta} + \theta'$) which is known as the Reynolds decomposition. After substituting the Reynolds decomposition into the governing equations and averaging them, one ends into a same kind of equations as (4.3) and (4.2) equations with some extra fluctuating terms accounting for the turbulence. (Pope, 2009, Chapter 4.1) There is no analytical solution for the fluctuating terms so those have to be modelled by empirical relations from the measurements or direct numerical simulation (DNS). In addition, most turbulence models assume turbulence to be isotropic which is not the case even for the simplest turbulent flows, however, it is usually a quite good approximation. (Pope, 2009, Chapter 4.2)

The difficulties in turbulence modelling comes from the fact that the turbulence is time-dependant and random, and N-S equations (4.2) are non-linear. Even more difficulties arise from the pressure gradient term which is both non-local and non-linear if it is obtained from Poisson equation. One should also realise that the pseudo steady-state turbulence models such as the models obtained with Reynolds decomposition cannot present a real flow as it is and all solutions with turbulence models should be validated. (Pope, 2009)

Currently there are quite a many different turbulent models in use including but not limited to Spalart-Allmaras, k-ϵ, k-ω and Reynolds stress turbulence models (Pope, 2009, Chapters 10 and 11). As the turbulence model mainly used in this study was k-ω SST, the formulation from ANSYS Fluent is going to be briefly presented in the equations (4.4) and (4.5). More information on the terms can be found from ANSYS Fluent user manual. (Ansys Inc., 2016, Shear-Stress Transport SST k-ω). For convenience, the variables presented in turbulence models are mean variables even thought the over-line is dropped from them.

$$\frac{\partial}{\partial x_i}(\rho k_T u_i) = \frac{\partial}{\partial x_j}\left(\Gamma_k \frac{\partial k_T}{\partial x_j}\right) + G'_k - Y'_k + S'_k \tag{4.4}$$

$$\frac{\partial}{\partial x_i}(\rho\omega u_i) = \frac{\partial}{\partial x_j}\left(\Gamma_\omega \frac{\omega}{x_j}\right) + G'_\omega - Y'_\omega + D'_\omega + S'_\omega \tag{4.5}$$

In the equations (4.4) and (4.5) k_T is the turbulent kinetic energy, ω is the specific rate of dissipation and Γ is the effective diffusivity. In both equations the first term in the left hand side represents the rate of change, the second term represents convection of the variable. At right hand side the first term represents diffusion while the G', Y', S' and D' represents production, dissipation, source and cross-diffusion respectively.

When using the turbulence models the velocities and temperature in the governing equations are mean values for a sufficiently long time scale and the fluctuation is accounted by increased diffusivity. Thus the kinematic viscosity and the thermal diffusivity in the N-S equations is replaced by the sum of turbulent and laminar diffusivities $\nu + \nu_t$ and $\alpha + \alpha_t$. Additionally, the effect of the turbulence in the energy equation is accounted with the turbulent energy Prandtl number $Pr_t = \frac{\nu_t}{\alpha_t}$ which in ANSYS Fluent for $k - \omega$ SST turbulence model defaults to 0.85.

There are also alternative methods to solving the turbulence such as Large-Eddy Simulation (LES) which solves more time and length scales and models only the short timescales and small length scales. LES is a transient model and as such it is computationally more intensive. LES also has much higher requirements for mesh quality and density which results in longer computation times. (Pope, 2009)

4.3 Grid generation

Grid generation is one of the most time consuming aspects of the CFD work-flow. The grid can be constructed from any kind off cells if the control volume discretisation is used. For example 2D grid may consist of rectangles or triangles and 3D grid may consist of hexahedrons, tetrahedrons or prisms. Hexahedrons and rectangles are considered to be structured and the triangles and tetrahedrons are considered to be unstructured from the grid generation point of view. The structured hexahedral or rectangle meshes are preferred mesh types as they require less elements for a same solution than unstructured meshes. (Versteeg and Malalasekera, 2007, Chapter 11)

There are many quality factors for the grid quality which should be as high as possible (Versteeg and Malalasekera, 2007, Chapter 1.2). In ANSYS Fluent, according to the manual, the most important quality parameters are skewness, orthogonal quality and aspect ratio of the cells (Ansys Inc., 2016, Mesh quality). Sometimes trade-offs has to be made and they may or may not adversely affect the solution procedure and solution. However, ANSYS Fluent is quite tolerant for poor quality meshes due to optimisations and corrections in the solver code but they still affect the accuracy of the solutions (Ansys Inc., 2016, Robustness on Meshes of Poor Quality).

For a solver to be able to resolve the high gradients near walls (this is especially important for viscous drag and heat transfer prediction as they both are related

to the gradients at wall) the mesh has to be properly refined at the regions with high gradients. For example, the usual practice is to compress the boundary layer cells close to surface to resolve high gradients in boundary layers. This compression is called a boundary layer mesh. The free flow usually doesn't require high grid density as there are no steep gradients, and less elements may be used there to save computational resources. (Versteeg and Malalasekera, 2007, Chapter 11)

When determining whether the near wall grid is dense or coarse enough the whole flow field has to be solved first to calculate dimensionless wall distance y^+ at wall which is given by the equation (4.6). When using $k-\epsilon$ turbulence model with standard wall functions y^+ should be from 30 to 500 but preferably closer to 30 (Versteeg and Malalasekera, 2007, Chapter 10.4). All k-ω based turbulence models requires y^+ to be preferably lower than 1 as they resolve whole boundary layer (Versteeg and Malalasekera, 2007, Chapter 10.4). In ANSYS Fluent there is possibility to use a blend of integration to the wall and logarithmic law for k-ω turbulence model which is much more insensitive to the near wall refinement which should make meshing somewhat easier (Ansys Inc., 2016, y_+-Insensitive Wall Treatment ω-Equation). However, to get an accurate solution the grid should be refined to the $y^+ = 1$ level while simultaneously using a proper wall formulation.

$$y_+ = \frac{u_* y}{\nu} \tag{4.6}$$

In the equation (4.6) the u_* is a friction velocity which is given by the equation (4.7) and y is a distance of cell centroid normal to a nearest wall. The friction velocity is given in the equation (4.7). (Versteeg and Malalasekera, 2007, Chapter 9.4).

$$u_* = \sqrt{\frac{\tau_w}{\rho}} \tag{4.7}$$

Another aspect of a good grid is to align the cells with the flow when using upwind schemes. When mesh is aligned with the flow direction, the false diffusion due to the discretisation schemes is minimised. However, in many cases flow may be very complex and the grid alignment is not possible at given time resources. (Versteeg and Malalasekera, 2007, Chapter 5.6)

4.4 Boundary conditions and simulated physics

In addition to the governing equations given earlier, the problem in question has radiative heat transfer which could be accounted with the Stefan-Boltzmann's equation. However, the radiative heat transfer was not enabled in CFD calculations as it was regarded to be of a minor importance. This was checked in validation of the CFD setup. Additionally, buoyancy was regarded as of minor importance as the Richardson number (4.8) $Ri = \frac{Gr_L}{Re_L^2}$ was less than 0.04 in all calculated cases, thus the gravity was not enabled. (Incropera et al., 2011, Chapter 9.3)

$$Ri_L = \frac{Gr_L}{Re_L^2} = \frac{\frac{\beta g \Delta T_{max} L^3}{\nu^2}}{\left(\frac{\rho V_{max} L}{\eta}\right)^2} \tag{4.8}$$

Turbulence models also cause its own problem in giving boundary conditions as the turbulence quantities at the inlet are usually not known, and only way to have proper boundary conditions with turbulence is to extent the computational domain in upstream until the flow entering the domain of interest can be regarded as fully-developed. However, this is usually not possible with given computational resources and the turbulence levels at the inlet has to be approximated by using values from, for example, fully developed turbulence in pipe or some guidelines for low, medium or high turbulence. Luckily, two equation turbulence models quite quickly assume a correct turbulence levels if a too high values for turbulence quantities are chosen due to turbulence dissipation in the two equation models. When choosing the turbulence levels it should also be noted that in practical applications the velocity is not constant for given cross-section which causes shear stresses in flow which increases the turbulence. If constant velocity boundary condition is chosen, and there is some finite distance to the heat exchanger core, the turbulence should be artificially set too high as the turbulence dissipation quickly diminishes the turbulence levels.

To decrease computational load, all possible symmetry planes should be utilised as resolving mirror domains only provide multiples of same answer as long as solution is fully converged and independent of time while increasing the computation resources twofold for each mirror plane. The symmetry boundary condition sets all gradients and normal components to zero at boundary and thus there is no flux of any quantity over the symmetry plane.

While comparing the solution with experimental data not only the boundary conditions have to be similar but the simulated physics has also be similar to a physics of an experiment. For example in this study as heat transfer is a quality of interest, the radiation should be enabled when comparing the solution to the experimental values. However, as its magnitude is most likely quite low, due to low temperature levels, compared to the convective heat transfer it may be omitted in the parametric studies to decrease computational load. Additionally, experiments are usually performed with lower temperature levels than engineering applications which decreases radiative heat transfer. For this reason, the overall heat transfer coefficient from those experiments should be lower than industrial correlations.

4.5 Data reduction

For a data reduction, dimensionless numbers for heat transfer and pressure drop were used to form correlations. For example, for heat transfer Nusselt number (2.13) and Colburn j-factor (2.14) while for friction Euler number (2.17), Darcy's and Fanning friction factors (2.18) are quite general dimensionless numbers. In this study, multivariable least squares correlations are developed for Nusselt number (2.13), Colburn

j-factor(2.14), Euler's number for one finned tube (4.9) and Fanning friction factor (4.10) as a function of Reynolds number. Especially interesting dimensionless numbers are Colburn j-factor and Fanning friction factor as they are of same order of magnitude and their division is rather constant in typical Reynolds number range for a given geometry (Shah and Sekulic, 2003, 10.3.1.1.). As the Prandtl number is practically constant 0.69 in all calculated cases, a typical literature value, for example from Dittus-Boelter correlation (3.14), for Prandtl number power of $\frac{1}{3}$ can be used to convert the Nusselt number correlation for a different Prandtl number.

$$Eu = \frac{\frac{\Delta P}{N_L}}{\frac{1}{2}\rho V_{max}^2} \tag{4.9}$$

$$f = \frac{\frac{1}{A}\int_A \tau_w dA}{\frac{1}{2}\rho V_{max}^2} \tag{4.10}$$

The Fanning friction factor was solved by using the equation (2.16) as those data quantities were more readily available. The friction factor could also be calculated with integrals at post-processing with the equation (4.10) but then the form drag and possible expansion and contraction losses in the heat exchanger core due to the tubes and fins is not accounted in the Fanning friction factor.

For calculation of these dimensionless numbers, data has to be extracted from a converged CFD solution. The total heat transfer may be extracted as an area integral with the equation (4.11), the pressure drop as an area average with the equation (4.12), the outlet temperature as a mass flow average with the equation (4.13) and the fin efficiency from the equation (3.1) by noting from Newton's law of cooling (2.12) that the convective heat transfer coefficient is defined as $h = \frac{q}{T_x - T_f}$ which results in the equation (4.14) for fin efficiency.

$$Q = -\int_A qdA\Big|_{\text{tube inner wall}} = \int_A \rho V c_p T dA\Big|_i - \int_A \rho V c_p T dA\Big|_o \tag{4.11}$$

$$\Delta p = \frac{1}{A}\int_A pdA\Big|_i - \frac{1}{A}\int_A pdA\Big|_o \tag{4.12}$$

$$T_o = \frac{1}{\dot{m}}\int_A \rho V T dA\Big|_o \tag{4.13}$$

$$\eta_f = \frac{\int_A q_w dA}{\int_A q_w \frac{T_x - T_w}{T_x - T_f} dA} \tag{4.14}$$

In the equation (4.14) for fin efficiency q_w is the heat flux at wall, T_w is the tem-

perature of fin base, T_f is the fin surface temperature and T_x is the evaluation temperature of the fluid at corresponding x-coordinate. All other quantities are easily extracted from CFD solution but the temperature at a given x location poses some difficulties due to there is no unambiguous temperature at given position downstream of core entrance which can be easily extracted from a CFD solution. However, a rather good approximation can be formed by utilising the heat balance for the fluid (2.4) and the heat transfer rate equation (2.5) and the dimensionless temperature difference at inlet and outlet compared to the finned tube base temperature may be written with the equation (4.15).

$$\begin{aligned} \frac{UA_h}{c_p\dot{m}} = \frac{Ubx}{c_p\dot{m}} = \ln\left(\frac{T_i - T_w}{T_x - T_w}\right) = \Theta_x \\ \frac{Ub}{c_p\dot{m}} = \frac{\Theta_x}{x} \end{aligned} \tag{4.15}$$

As the value of the Θ_x at heat exchanger outlet L is known as all temperature are known after CFD calculation the equation (4.15) may be solved to formulate the equation (4.16) for the fluid temperature in heat exchanger core.

$$\begin{aligned} \Theta_x &= \Theta_L \frac{x}{L} \\ T_x &= (T_i - T_w)e^{\Theta_L \frac{x}{L}} + T_w \end{aligned} \tag{4.16}$$

This approximation of the temperature distribution in a heat exchanger core is exact only when the fluid has a constant specific heat capacity, and heat transfer coefficient is uniform over the heat transfer surface and heat transfer area is directly proportional to a distance from the heat exchanger core inlet i.e $A_h = xb$. While these might sound unreasonable assumptions, in the end the error averages out and this results in a much more realistic temperature distribution compared to using average temperature between inlet and outlet for calculating the fin efficiency.

5. MODEL DESCRIPTION

For a flow through the finned tube heat exchanger, there are no analytic solutions for variable geometric parameters. The empirical correlations given in literature are developed for a limited range of designs and unknown inlet conditions while simultaneously averaging the correlation to give even somewhat correct values for a range of different geometries. These are not the best options for studying the effects of the geometric parameters to the finned tube thermal-hydraulic performance. Thus multiple cases are calculated with the commercial CFD software ANSYS Fluent study the effects of the geometric parameters more in-depth. Additionally, correlations for Nusselt number and Colburn j-factor, and Euler number and Fanning friction factor for each case is developed to compare the cases in heat exchanger dimensioning section 8.2 with a given limiting boundary conditions.

5.1 Reference design

H-type finned tube design consists of a tubes with attached fins with a longitudinal slit between the fins to ease the manufacturing. A simple picture of a finned tube assembly is given in a Fig. 5.1. The dimensioning parameters used in CFD are given in the Fig. 5.2.

In the Fig. 5.1 there are six tubes spanwise N_L, three tubes in width N_T and 15 fins to show the general finned tube assembly. The frontal area where the flow enters the heat exchanger core is shown in front (normal to z) while the upper and lower part with fin edges (normal to x) would be as close to casing as possible. The tube ends (normal to y) shown would have headers and bends to distribute the saturated water and to connect the tubes to form a long pipe.

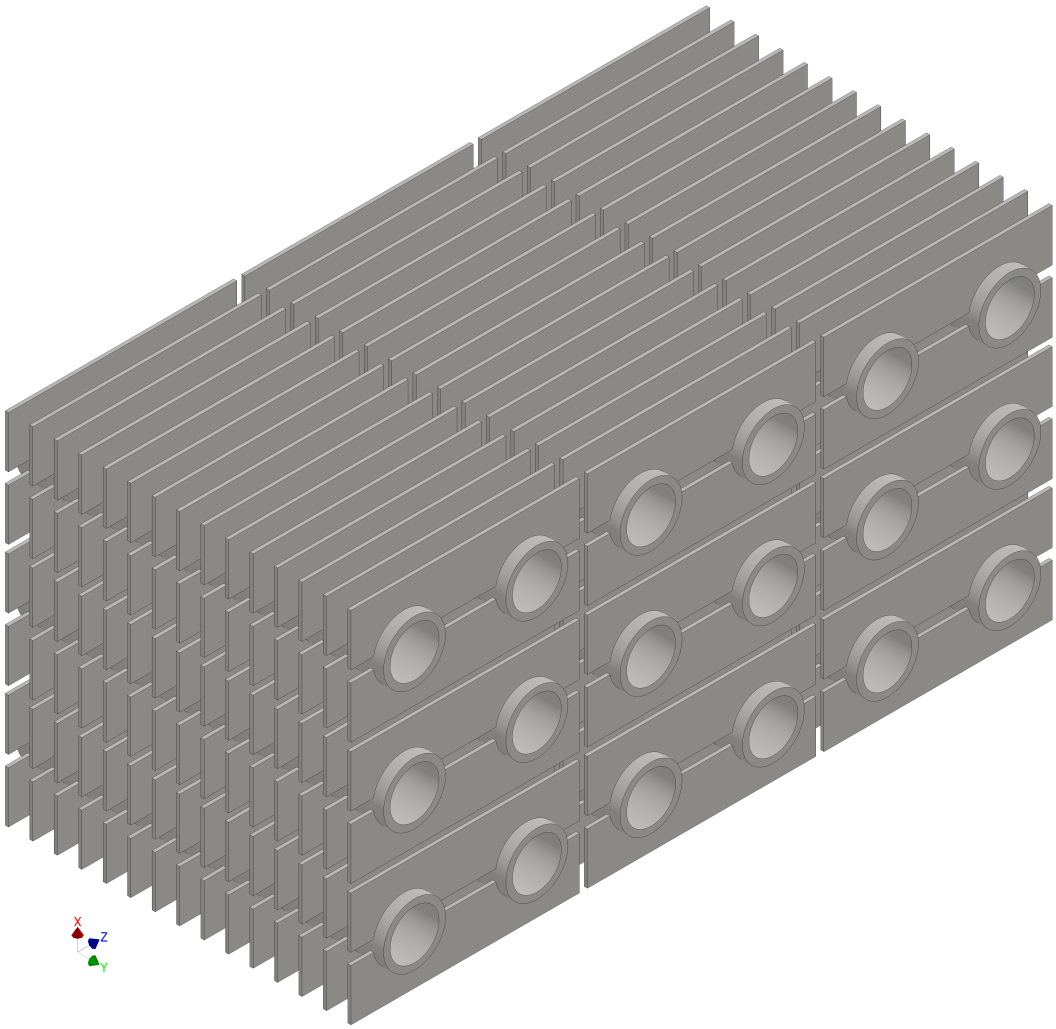

Figure 5.1. *A simple finned tube assembly*

The Fig. 5.2 shows the dimensions of the finned tube for one fin symmetry. A table with the geometric parameters which has been varied in this study can be found from the Appendix A

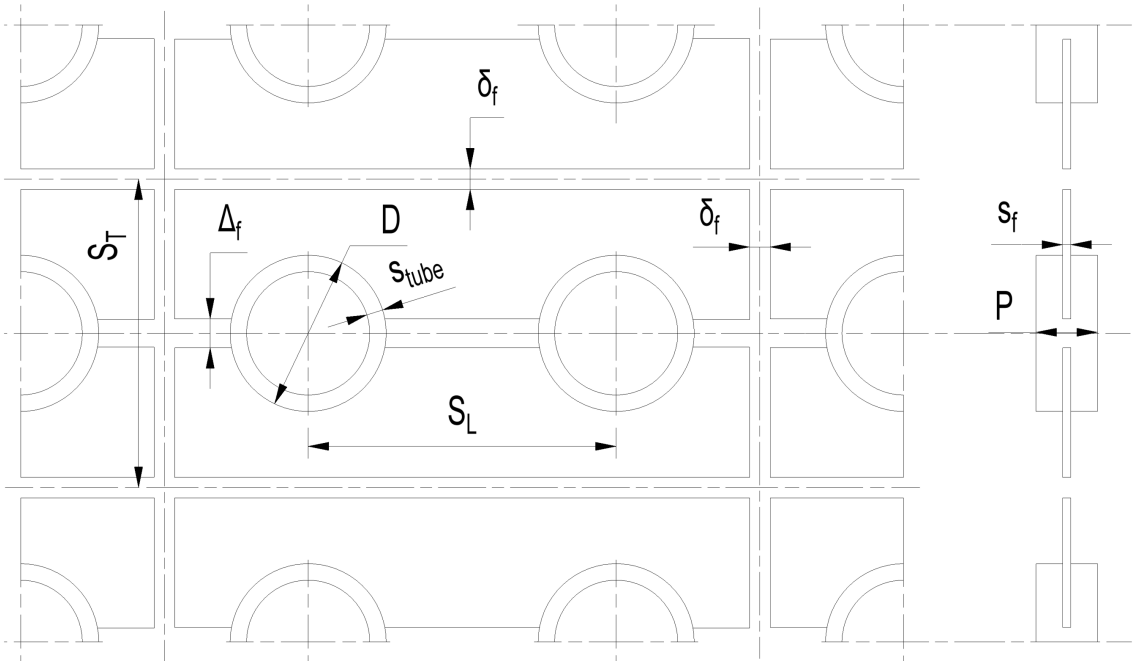

Figure 5.2. *Finned tube dimensioning drawing*

The Table 5.1 gives the names, notation, reference value and the range of the parameters used in this study. The table is only for CFD calculations in this study but the validation case used in the model validation section were within the range.

Table 5.1. *Description of the geometric parameters used in study*

Name	Notation	Reference (mm)	Range (mm)
Tube outer diameter	D	38	28-52
Fin pitch	P	15	10-30
Transverse pitch	S_T	75	60-125
Longitudinal pitch	S_L	75	60-100
Fin thickness	s_f	2.5	1.5-3.5
Fin slit	Δ_f	7	4-14
Fin gap	δ_f	3	2-6
Tube wall thickness	s_w	4	4

5.2 Calculation domain

The geometry was modelled with ANSYS Design Modeller. The basic geometry is similar to the one given earlier in the Fig. 5.2. As there were multiple cases, the model was developed as a parametric model to speed-up the geometry processing.

For the calculation domain, all possible symmetries were utilised to minimise the calculation time and memory usage. Thus the geometry was split between fin symmetry plane, tube symmetry plane and pitch symmetry plane resulting in a geometry given in Fig. 5.3.

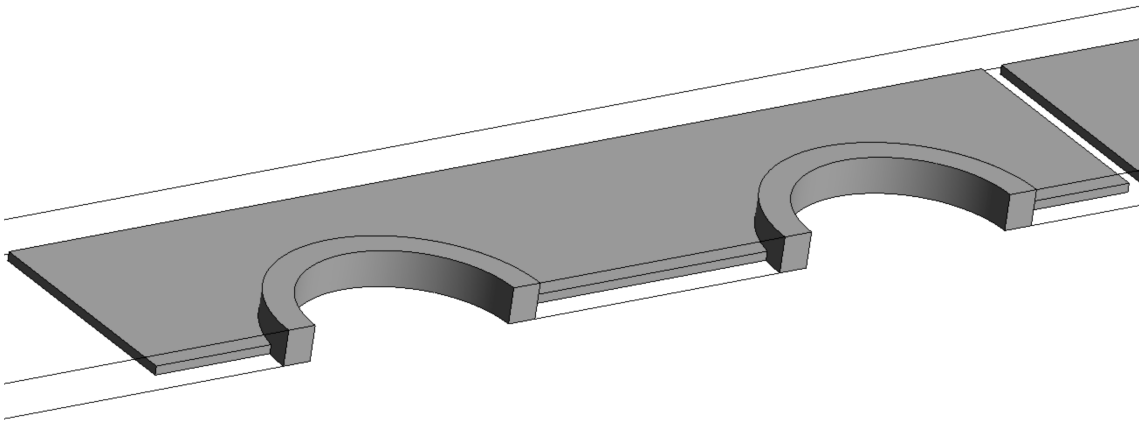

Figure 5.3. *CFD calculation domain*

The inlet region was extended 5 tube diameters upstream to avoid the effects of the inlet region on the quantities of interest. Similarly the outlet region was extended 10 tube diameters downstream to avoid backflow at outlet and to ensure that flow field is not affected by the abrupt cutting of the domain at downstream.

To model the developing region, 6 tubes was considered to be sufficient to capture the effect of the developing region while keeping computational requirements at minimum. As seen further there should have been more tubes to really get fully-developed profiles at last fins. However, as the most of the fins are in the developing region in heat exchangers in this study, this was seen as sufficient average of the fin performance. The number of tubes in row was not varied in this study as the memory requirement for more tubes would have been too high. Another way would have been to model fully-developed conditions for a fin system by using periodic boundary conditions for the inlet and outlet but, as most of the fins are in reality at the developing region, this idea was discarded.

5.3 Computational mesh

The computational mesh was generated by using the commercial software ANSYS ICEM. All meshes for the geometries were constructed as hexahedral mesh by using a blocking technique with O-grids for a better mesh quality around tubes. As there were multiple cases and the mesh generation is very time consuming, a parametric meshing script was generated to speed-up the mesh generation. The blocking technique produces all hexahedral mesh which was mostly flow aligned. After the script only slight modifications had to be done to improve skewness in the corners of the O-grid. The maximum skewness of meshes reported by ANSYS Fluent was lower than 0.4 and the orthogonal quality reported by ANSYS Fluent was higher than 0.8 which might be regarded as a very good mesh. The aspect ratio for the boundary layer elements was under 100 while for most other elements it was well below 10.

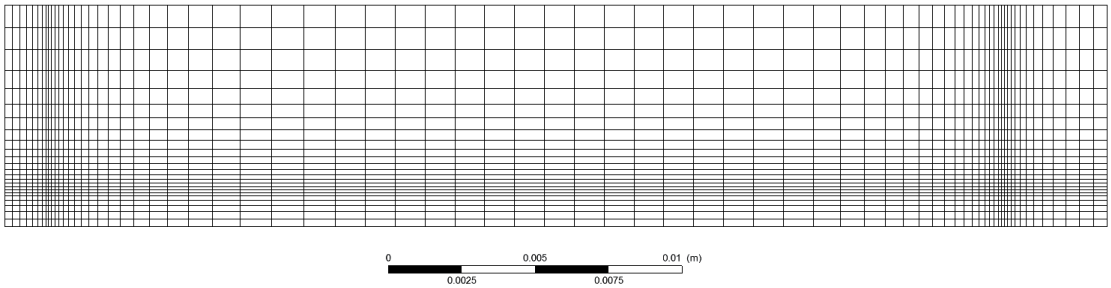

Figure 5.4. *Mesh at inlet*

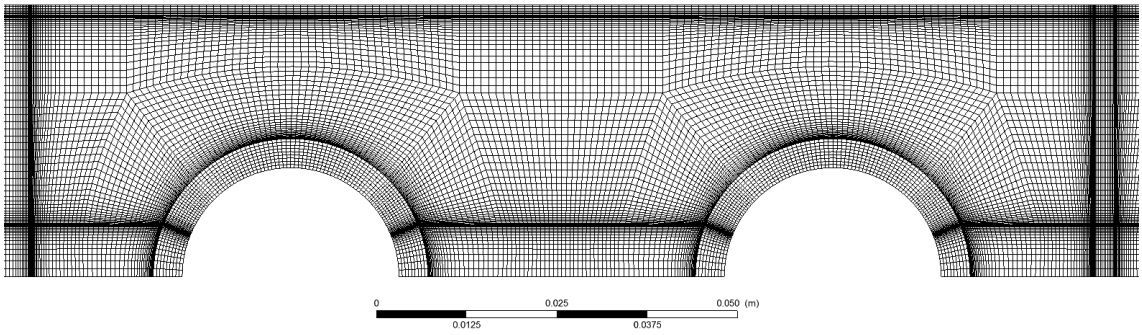

Figure 5.5. *Mesh from top*

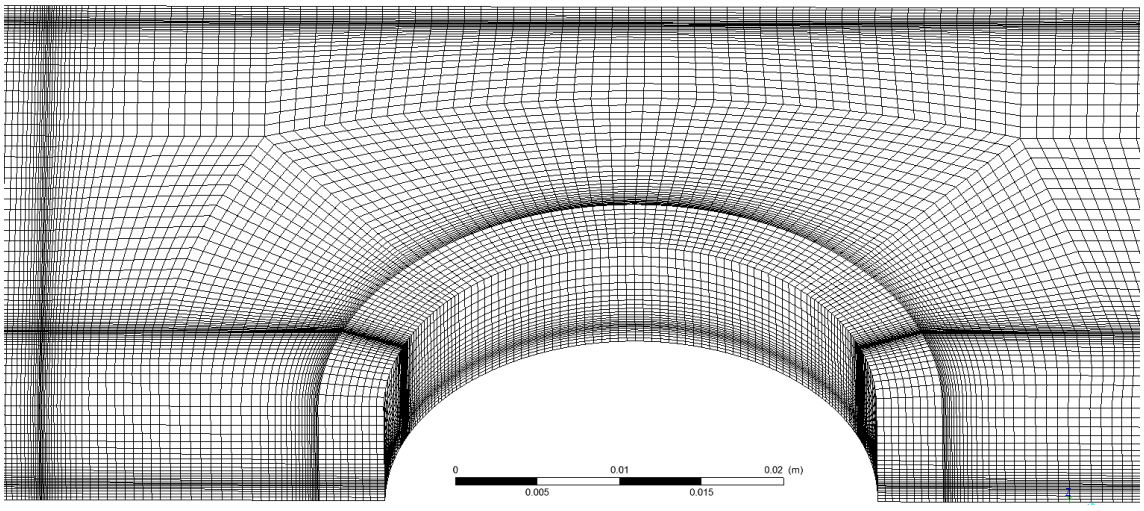

Figure 5.6. *Mesh side-view*

The blocked mesh distribution at all three directions is given in the Figs. 5.4, 5.5 and 5.6. The choice of meshing parameters is discussed more in-depth at section for mesh independency.

5.4 Solution method and models

For solving the partial differential equations for continuity, momentum, energy and turbulence, a coupled solver was selected due its reliable convergence characteristics and fast convergence with pseudo-transient formulation. All discretisation schemes were chosen as second-order upwind scheme. Pressure was discretised with second-order scheme. For gradient scheme, a Green-Gauss node-based scheme was chosen due to its superior performance with distorted meshes such as the corners of the O-grid. Additionally, the double precision solver was used to minimise numerical errors. Choices to speed-up convergence are given in the appendix B.

In addition to monitoring the residuals, the total heat transfer, pressure drop, average outlet temperature and fin average temperatures were monitored for convergence. Solution was deemed as converged and with an acceptable linearisation error when all residuals had fallen into a range between $1e^{-7} - 1e^{-6}$ which resulted in convergence of the monitored values. Additionally the fulfilment of given boundary conditions was checked from the solutions with an addition of checking mass, momentum and energy imbalances which all were well below 1 %.

k-ω SST turbulence model was chosen as a primary turbulence model. The k-ω SST is regarded to be a one of the best two equation turbulence models for wall bounded flows and flows with separation by ANSYS as it uses k-ω formulation near the wall while in the free shear region the model blends into a standard k-ϵ turbulence model. k-ω SST also has more realistic sensitivity to the free stream turbulence values compared to the standard k-ω turbulence model. (Ansys Inc., 2016, Shear-Stress Transport (SST) k-ω Model). The viscous heating, curvature correction and production limiter were enabled to account for streamline curvature at tubes and to prevent excessive production of turbulent kinetic energy at stagnation point.

Method validation cases were also calculated with the k-ϵ Realizable turbulence model for comparison. k-ϵ Realizable has additional modelling compared to the standard k-ϵ which gives better results with swirling flows. This turbulence model is also regarded as one of the best available two equation turbulence models by ANSYS. (Ansys Inc., 2016, Realizable k-ε Model) Enhanced Wall Treatment (EWT) was used as a wall formulation for k-ϵ Realizable with pressure-gradient and thermal effects corrections. The viscous heating, curvature correction and production limiter were enabled to account for streamline curvature at tubes and to prevent excessive production of turbulent kinetic energy at stagnation point.

5.5 Boundary conditions

The inlet conditions of heat exchangers in this study, can roughly be divided to two possibilities. The first case is the inlet from the exhaust gas duct which usually has fully-developed pipe flow before the expansion cone and after that very erratic flow behaviour as the jet collides with the finned tube bank. The second possibility is a multiple finned tube bank heat exchanger where the finned tube bank exit

upstream produces high levels of turbulence for the second tube bank due to the shear stresses associated with the flattening of the velocity profiles. In this study, the inlet region was, however, considerably simplified, and an uniform velocity profile with low turbulence levels was chose. The low turbulence levels might result in about 40 % lower heat transfer at the first tubes according to (VDI e. V., 2010, Chapter G7) which should result in lower heat transfer rates for the simulations compared to the engineering applications.

All fluid domains in this study are air and all solid domains were carbon steel. As the cases in this study involves only slight pressure variation and low Mach numbers across the computational domain, the air properties can be assumed to vary only with the temperature. A constant operational pressure of $p_{operational} = 101325Pa$ may be used in evaluating the fluid properties as the flow can be considered incompressible. The correlations and their errors for air properties are given in the Table E.1.

The solid was modelled as a carbon steel with constant properties. The properties used in this study for carbon steel are 7850 $\frac{kg}{m^3}$, 502.48 $\frac{J}{kgK}$ and 45.0 $\frac{W}{mK}$ for density, specific heat capacity and heat conductivity respectively. It should be noted that as the computation was done as a steady-state computation, only the heat conductivity matters to the final solution.

The inlet boundary condition is given as velocity inlet which requires giving the velocity vector, temperature and turbulence quantities at the inlet. The inlet boundary conditions are given in the equation (5.1). All profiles were assumed to be uniform for the sake of convenience as velocity had to be changed frequently.

$$\begin{aligned} V &= V_i \\ T &= 623 \text{ K} \\ I &= 1 \text{ \%} \\ \frac{\mu_t}{\mu} &= 2 \end{aligned} \tag{5.1}$$

The outlet boundary condition was chosen as a pressure outlet which requires giving the static gauge pressure at the outlet. Additionally, as there might be a backflow at the outlet during a solution procedure, realistic backflow values should be provided to speed-up convergence. The boundary condition for outlet is given in the equation (5.2).

$$\begin{aligned} p_{gauge} &= 0 \\ T &= 550 \text{ K} \\ I &= 5 \text{ \%} \\ \frac{\mu_t}{\mu} &= 10 \end{aligned} \tag{5.2}$$

For the wall adjacent fluid cells a no-slip boundary condition is used. The boundary conditions for wall cells adjacent to fluid cells are given in the equation (5.3). The energy boundary condition was given by coupling the fluid and solid domains.

$$\begin{aligned} u\Big|_{wall} &= 0 \\ v\Big|_{wall} &= 0 \\ w\Big|_{wall} &= 0 \\ \varepsilon\Big|_{wall} &= 0 \\ \omega\Big|_{wall} &= \infty \\ k_T\Big|_{wall} &= 0 \\ T\Big|_{\text{fluid wall}} &= T\Big|_{\text{solid wall}} \\ k\frac{\partial T}{\partial n}\Big|_{\text{fluid wall}} &= k\frac{\partial T}{\partial n}\Big|_{\text{solid wall}} \end{aligned} \tag{5.3}$$

The wall inside the tubes was set to a constant temperature. This corresponds to the infinite heat transfer coefficient inside the tubes.

5.6 Mesh independence

As all finite volume CFD solutions requires a computational mesh and as computational mesh introduces a discretisation error due to solving the continuous equations in a discrete domain, a mesh independence study should be performed. A purpose of the mesh independence study is to evaluate the required mesh density needed for a solution where the discretisation error is within a chosen allowed error. This does not, however, eliminate the model errors.

In this study the mesh independence was evaluated by varying the maximum edge length of computational cell close to fins and the first layer thickness of the boundary layer mesh. The maximum edge length of a computational cell ranged from 0.5 mm to 2.5 mm while the first layer size ranged from 0.04 mm to 1.5 mm. The ratio of

growth between the adjacent cells was selected as 1.15. It should be noted that the boundary layer refinement combined with the growth ratio also affects the cell edge length near the walls.

The inlet and outlet regions were allowed to expand up to 4.0 mm and 5.0 mm respectively to save computational resources. The choice was quite arbitrary but after couple of choices it was regarded that only the mesh density near inlet and outlet of the fin region where the gradients are higher was important and farther away even coarser mesh might have been sufficient.

The mesh independence study was performed for the case 1 given in appendix A. The inlet velocity was set to 8 $\frac{m}{s}$ ($Re_D \approx 14200$) while keeping the other boundary conditions as given earlier in the section 5.5 for boundary conditions. The turbulence models was chosen as the k-ω SST according to the validation section 5.7. The validation and the mesh independence was conducted at the same time with the method validation case as the choice of the turbulence model might affect the required mesh density.

The Figs. 5.7 and 5.8 represent the effect of the mesh refinement on the pressure drop and total heat transfer refinement with different boundary layer first layer thicknesses. The x-axis presents mesh cell count while y-axis presents pressure drop and total heat transfer respectively while boundary layer first cell thickness is given in the legend. As it can be seen from the figures 5.7 and 5.8 the boundary layer first cell size is much more important parameter in minimising the discretisation error than the successive refinement of the whole mesh. After boundary layer first cell thickness of 0.1 mm the heat transfer and pressure drop is rather constant regardless of the cell edge length.

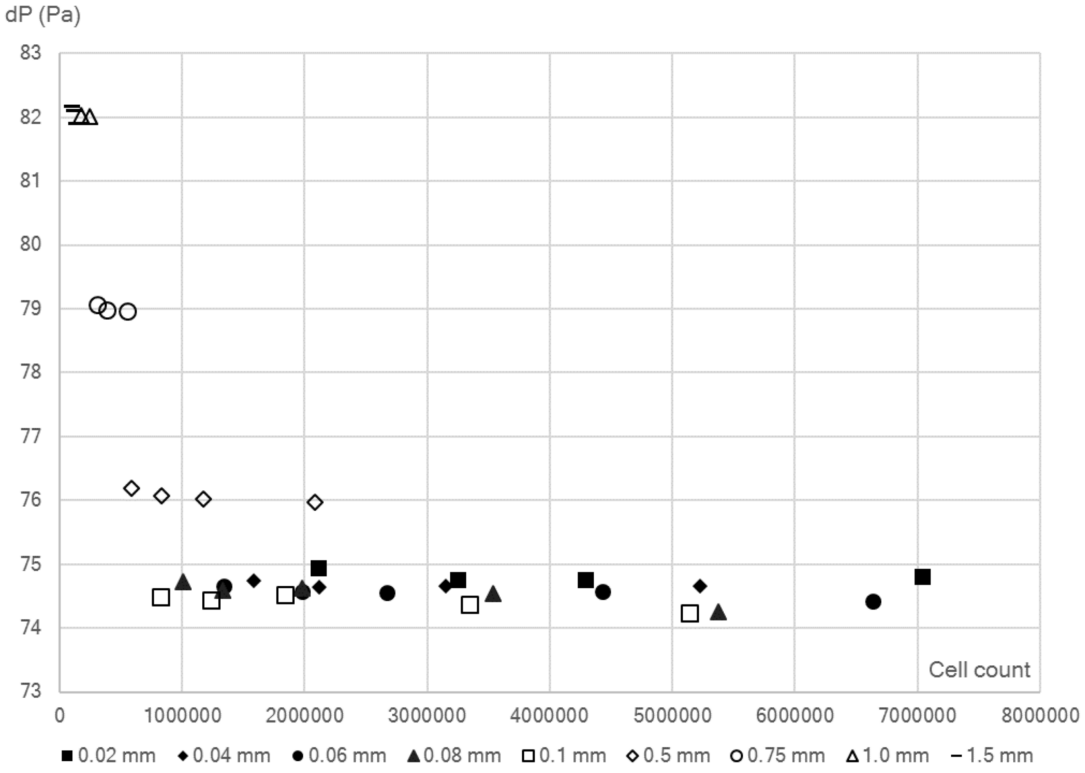

Figure 5.7. *The effect of the cell edge length refinement on the pressure drop over the fin system with the boundary layer first cell thickness given in legend.*

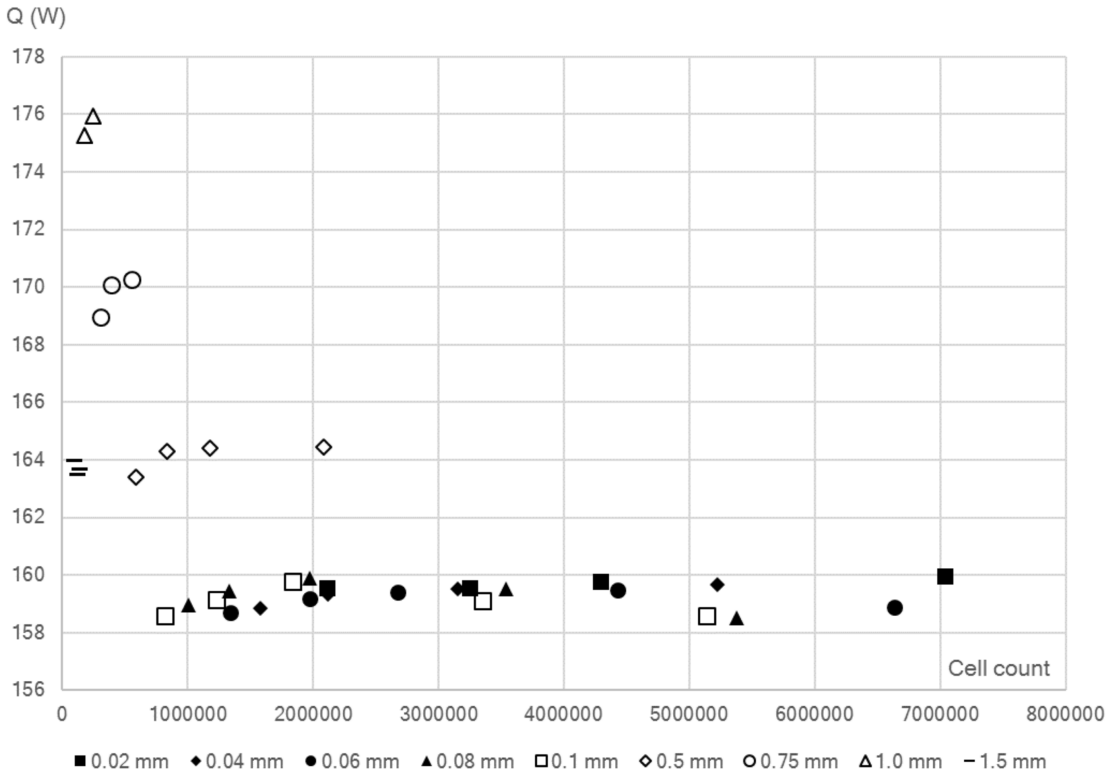

Figure 5.8. *The effect of the cell edge length refinement on the total heat transfer over the fin system with the boundary layer first cell thickness given in legend.*

The figures 5.9 and 5.10 represent the effect of the boundary layer refinement on the pressure drop and total heat transfer refinement with cell edge lengths. Figures are actually duplicates of the earlier figures with different legends but they were presented to visualise the effects of the boundary layer thickness refinement and edge length refinement separately. As it can be seen from the figures 5.9 and 5.10 after the cell edge length 1.5 mm or less, the total heat transfer and pressure drop are rather constant.

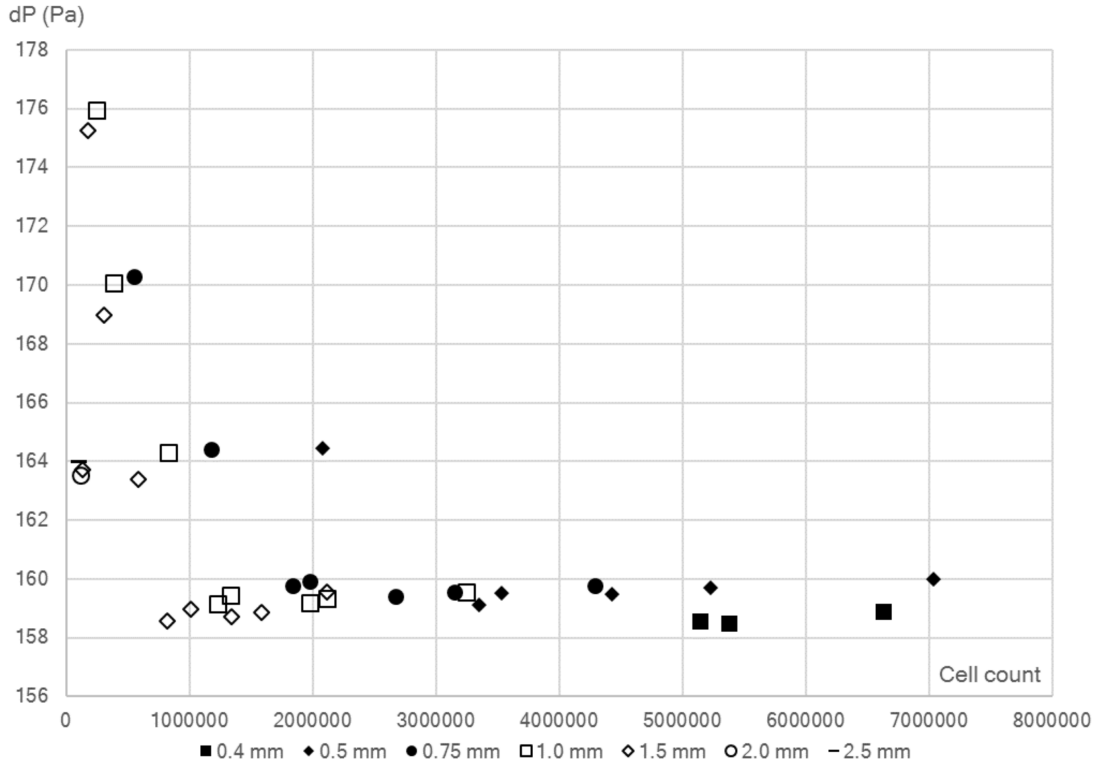

Figure 5.9. *The effect of the boundary layer first cell thickness refinement on the pressure drop over the fin system with the cell edge length given in legend.*

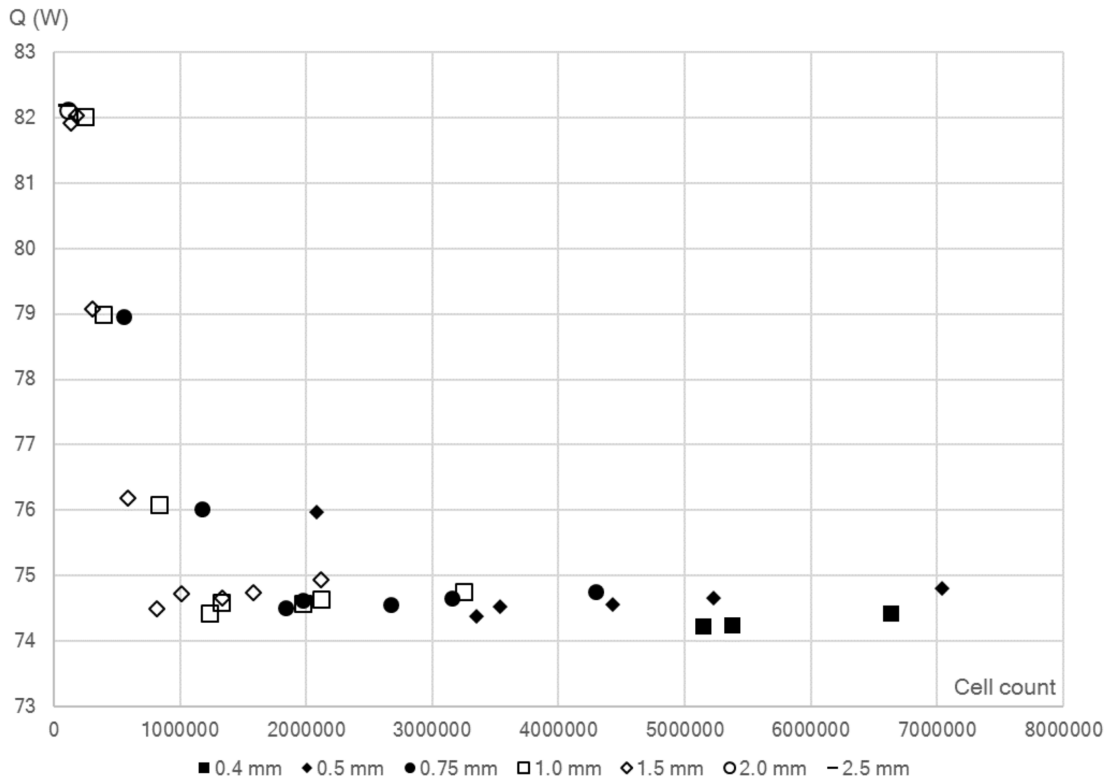

Figure 5.10. *The effect of the boundary layer first cell thickness refinement on the total heat transfer over the fin system with the cell edge length given in legend.*

From the mesh independency study it can be concluded that by choosing 0.1 mm first layer thickness for boundary layer and cell edge length of 1.0 mm the solution has quite low discretisation error which in this kind of optimisation study can be regarded as sufficiently small. The y^+ for this mesh refinement and 8 $\frac{m}{s}$ inlet velocity was maximum of 2 while the most of the wall adjacent cells were below 1.

It should be noted as higher velocities than 8 $\frac{m}{s}$ are used in this study for making a correlations over wide Reynolds number range, the higher velocity solutions have higher discretisation error due to the higher y^+ values and lower first boundary layer cell size should have been used for those cases. As it can be seen from the earlier figures 5.7, 5.10, 5.7 and 5.8 too low boundary layer refinement causes a slight overestimation in both heat transfer and pressure drop which means that all values above maximum velocity corresponding to the 8 $\frac{m}{s}$ in this case are overestimated in both heat transfer and pressure drop. However, as the required mesh count would have increased really fast with higher boundary layer refinement, this error was not deemed to be too significant as the most of the solutions were in a proper y^+ range and correlations should average the results to some extend.

5.7 Method validation

The calculation method was validated to the experimental wind tunnel study by Chen et al. (2015). It should be noted that radiation was not modelled in these studies and as such all heat transfer rates should be lower than in experiments. The geometry was otherwise similar to the CFD cases calculated in this study but the finned tube layout was single gilled tube instead of the double gilled tubes. The constant parameters were tube diameter of 38 mm, transverse tube pitch of 98 mm, longitudinal tube pitch of 92 mm, gap between fins of 3 mm, slit width of 13 mm, fin thickness of 2.5 mm and tube thickness of 4 mm. The fin pitch was varied from 12.7 mm at case A to 19.05 mm at case B. A dimensioning drawing of the geometry is given in Fig. 5.11

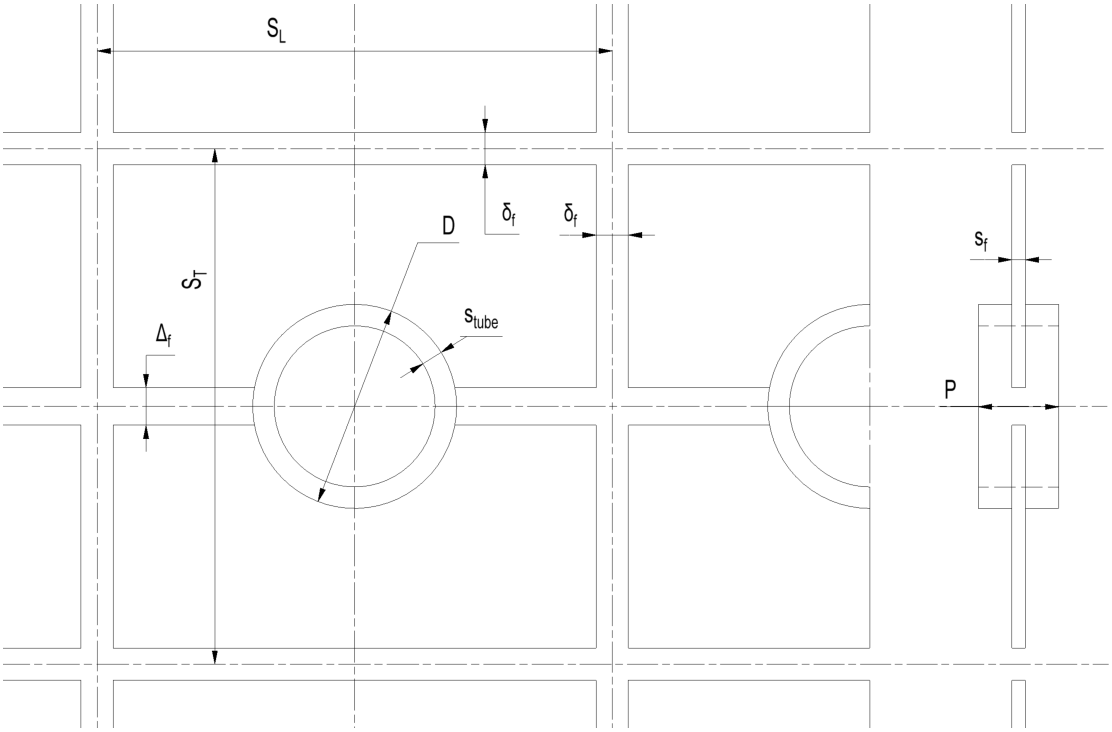

Figure 5.11. *Geometry validation case.*

Only two tubes were tested experimentally which rises some questions about applicability of the CFD for such a low flow length where correct estimation of the point of transition might have a considerable effect on the heat transfer and pressure drop and this is known to be challenging for simple two equation turbulence models.

To validate the model, the correlations (3.27), (3.26) and (3.28) and the correlations for Nusselt number (3.29) and fin efficiency (3.1) given in (VDI e. V., 2010, Chapter M1) were compared to the CFD data. The Nusselt number correlation by Schmidt is developed for highly turbulent industrial applications and thus it should be somewhat higher than in these low turbulence cases (VDI e. V., 2010, Chapter M1).

As seen from the figures 5.12, 5.13 and 5.14 the CFD calculation are mostly on the same range as experimental data for the case A with the lowest fin pitch. The k-ω SST seems to be better turbulence model for heat transfer prediction and slightly worse for pressure drop prediction. Euler number shows highest discrepancies from the experimental data wit the lowest Reynolds numbers being in the range of experiment while the higher Reynolds numbers gave higher pressure drop than the pressure drop from the Chen's correlation. This geometry had quite a low fin pitch and as such it may affect the development of the flow conditions in a way that flow becomes fully-developed much faster than for the cases with higher fin pitch. Additionally, it should be noted that the k-ϵ Realizable gives higher heat transfer coefficient than the experimental values which is somewhat nonphysical as radiation is not modelled and it will most likely increase the total heat transfer.

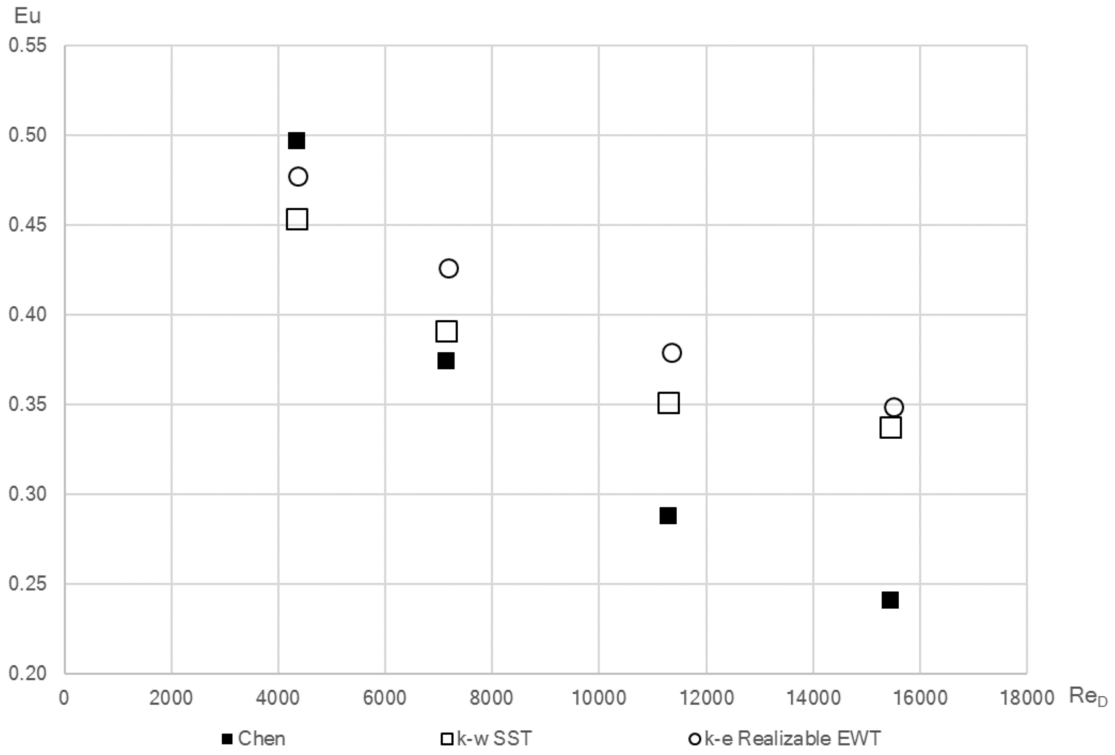

Figure 5.12. *Euler number for validation case A.*

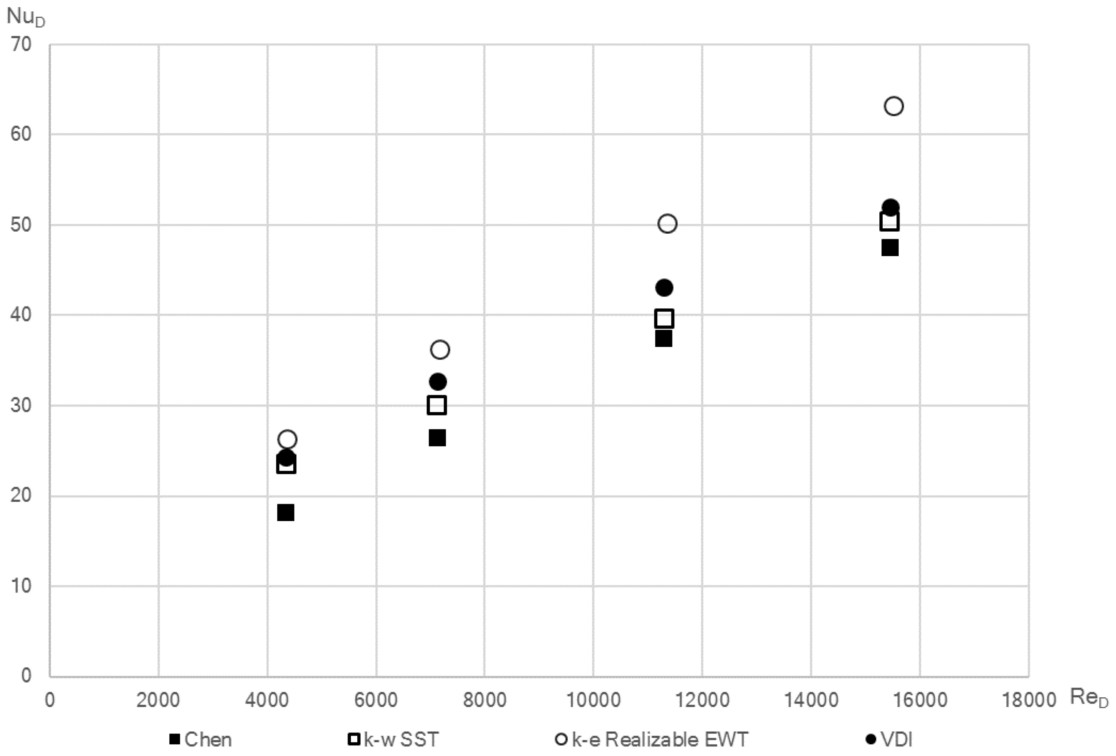

Figure 5.13. *Nusselt number for validation case A.*

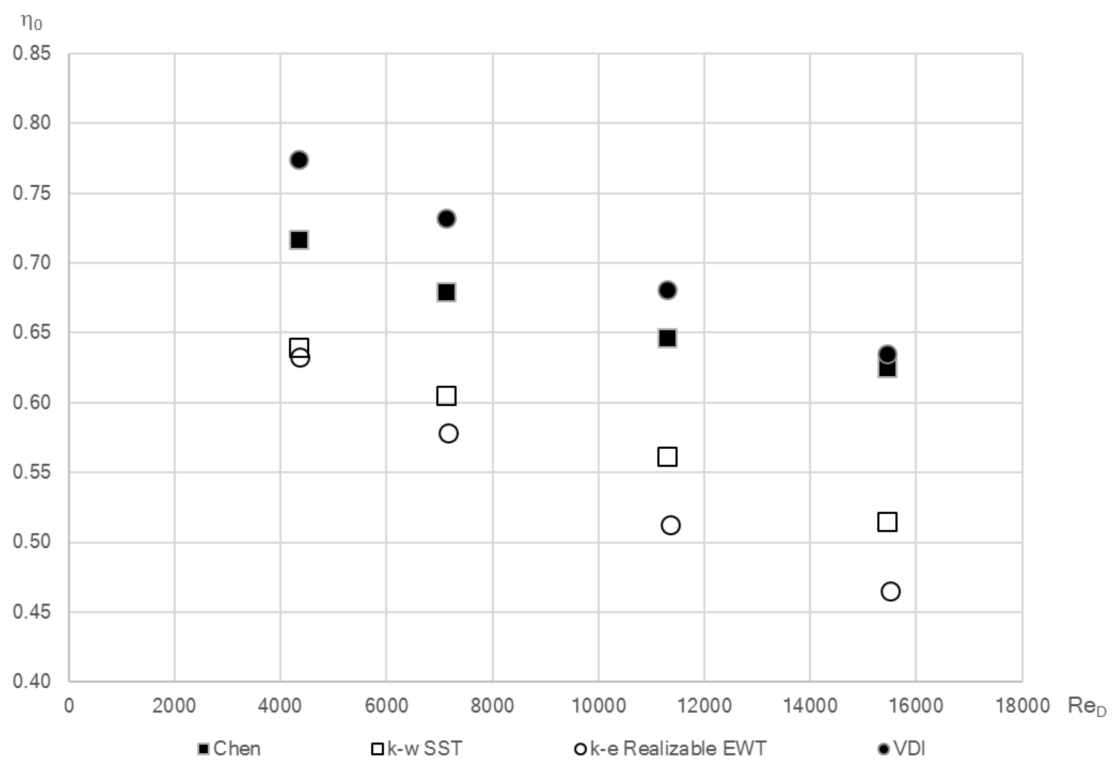

Figure 5.14. *Surface efficiency for validation case A.*

The figures 5.15, 5.16 and 5.17 show similar trend as before even though pitch is somewhat higher. For this pitch the k-ω SST agrees with the experimental data very well. Again, Euler number shows different Reynolds number dependency than the correlation by Chen. The heat transfer coefficient prediction is really close to measured values for k-ω turbulence model. In addition, the VDI correlation seem to be in same range although with different Reynolds number power.

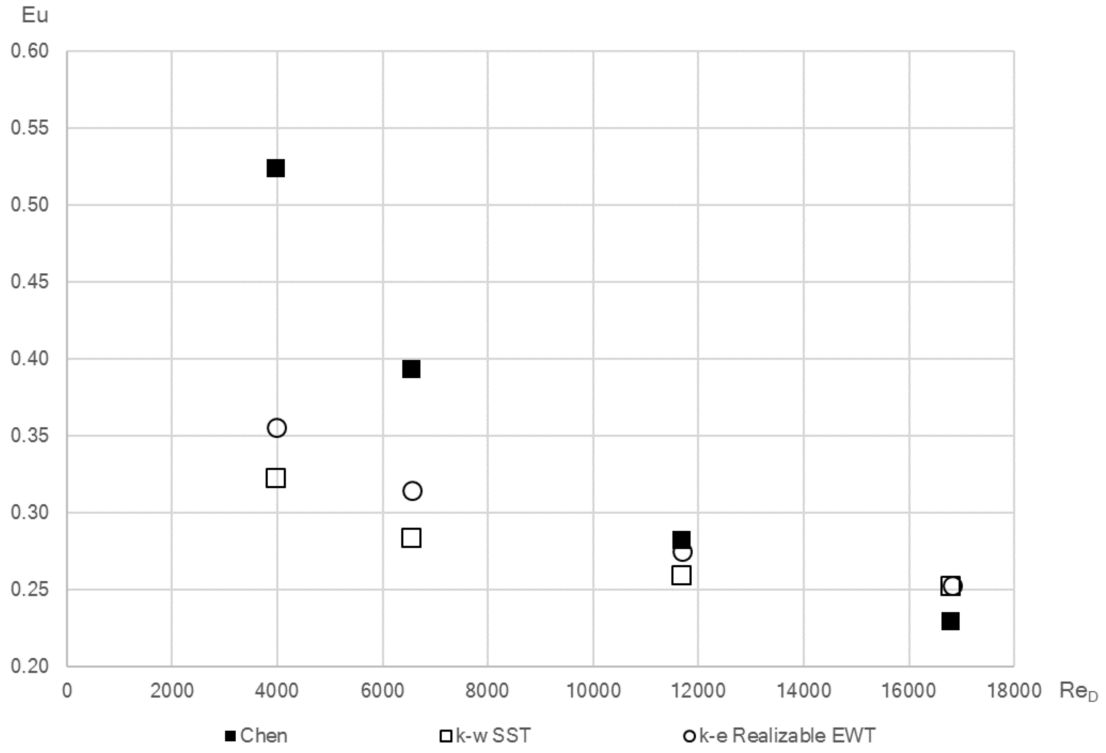

Figure 5.15. *Euler number correlation for validation case B.*

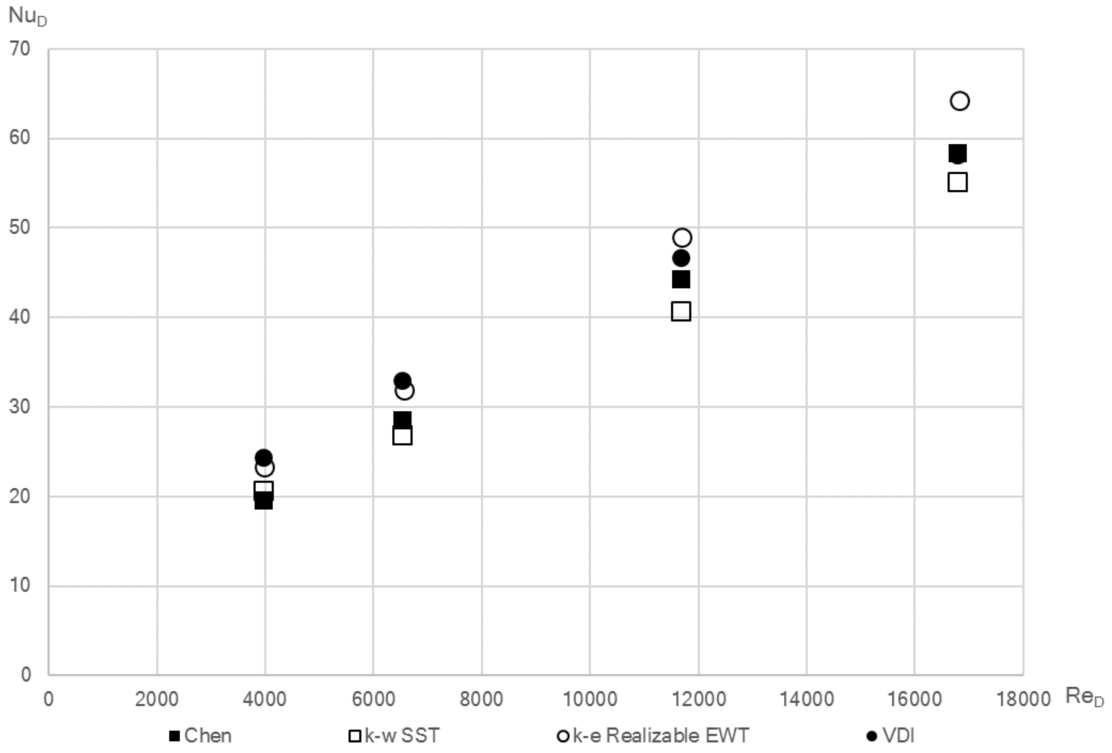

Figure 5.16. *Nusselt number correlation for validation case B.*

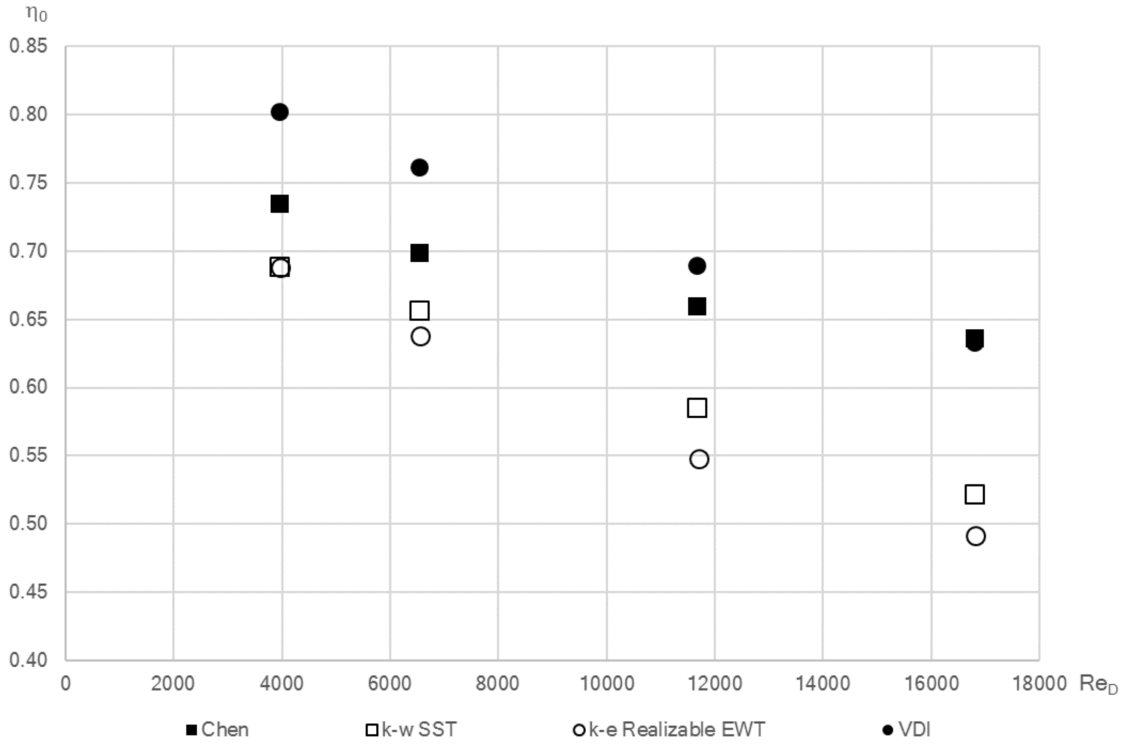

Figure 5.17. *Surface efficiency for validation case B calculated from correlation by Chen, CFD and correlation by VDI.*

Neither k-ω SST or k-ϵ are especially good in predicting Euler number. It should, however, be noted that the Chen had quite different correlation for Euler number with pressure drop increasing in the power of 1.6 while some studies give values closer to 1.8 which is the case for these CFD calculations (Kays and London, 1964). The heat transfer coefficient prediction seems to be within 10 % k-ω SST while k-ϵ gave values 20 % higher than the measured values. The fin efficiency gave quite low values for the CFD calculations which could be associated with wrong thermal conductivity used in the CFD calculations as the material of the fins was not reported in the article. Overall, k-ω SST seems to be a better turbulence model in simulating finned tube heat exchanger thermal-hydraulic characteristics.

6. FLOW FIELD VISUALISATION

The flow field visualisation is useful as it gives insight on the overall behaviour of the flow, and it allows the validation of the CFD calculation to some extent. There are multiple ways to visualise the CFD solutions including but not limited to contour plots at the surfaces, vector presentation of vector quantities and streamlines launched from the places of interest. CFD-Post by ANSYS was used in visualising the CFD solution.

In this study due to a sheer amount of the data from multiple cases only the case 1 in appendix A is visualised. Other cases are mostly similar in geometry and as such the solutions gives similar visualisations as calculation methods and the mesh were similar. The boundary conditions was given as in section 5.5 for boundary conditions while the the inlet velocity was chosen as 8 $\frac{m}{s}$. Due to limited resources six tubes in streamwise direction was chosen as sufficient to capture the flow behaviour in a typical heat exchanger applications. The locations of the planes used in visualisation is given in Fig. 6.1.

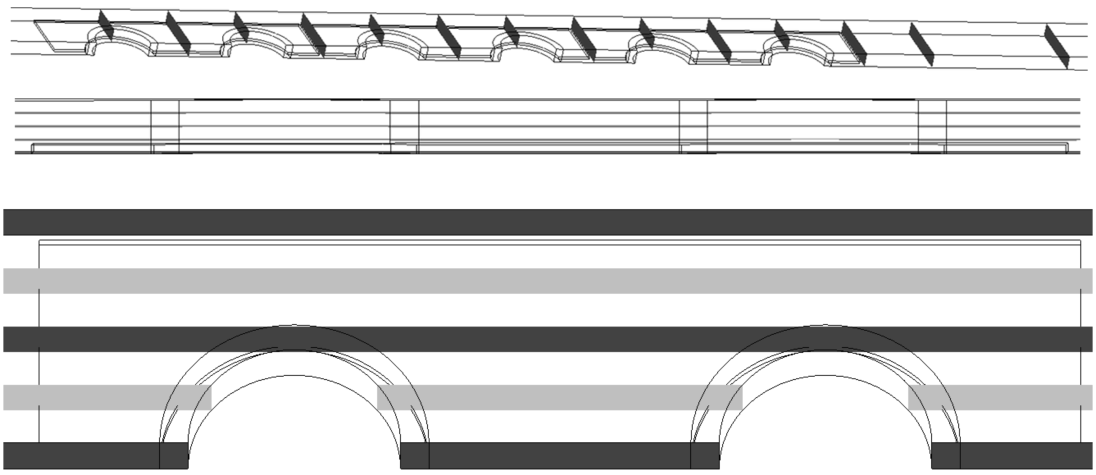

Figure 6.1. *Visualisation planes used in this study.*

The pressure contour is given in the Fig. 6.2 at symmetry plane between the fins as the pressure does not change much normal to the fins. The stagnation point where the velocity decreases to zero at at the front of the first tube is also more evident in the symmetry plane between fins.

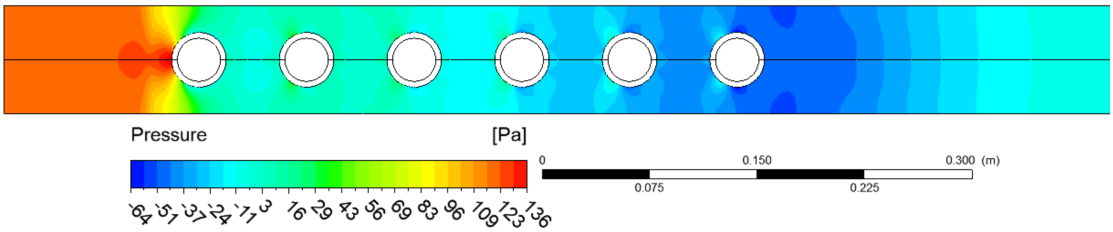

Figure 6.2. *Pressure contour at the symmetry plane between the fins.*

6.1 Velocity contours

The velocity contours give an overall view of the flow behaviour and shows the large scale structures of the flow. Only noticeable large scale structures in this study are the recirculation region between the tubes ant the recirculation region after the last tube. In the next figures the velocity contours are given normal to the fins, tangential to the fins and in different positions in streamwise direction. In addition, all velocities are streamwise velocity components.

The streamwise velocity contours normal to fins are given in Fig. 6.3. It can be seen that the flow represents a duct flow between the tubes quite fast. However, while it is not as evident from the figure, the flow between fins does not assume fully-developed flow at this low streamwise length. The expected recirculation region between the tubes and after the last tube is also present in the figure.

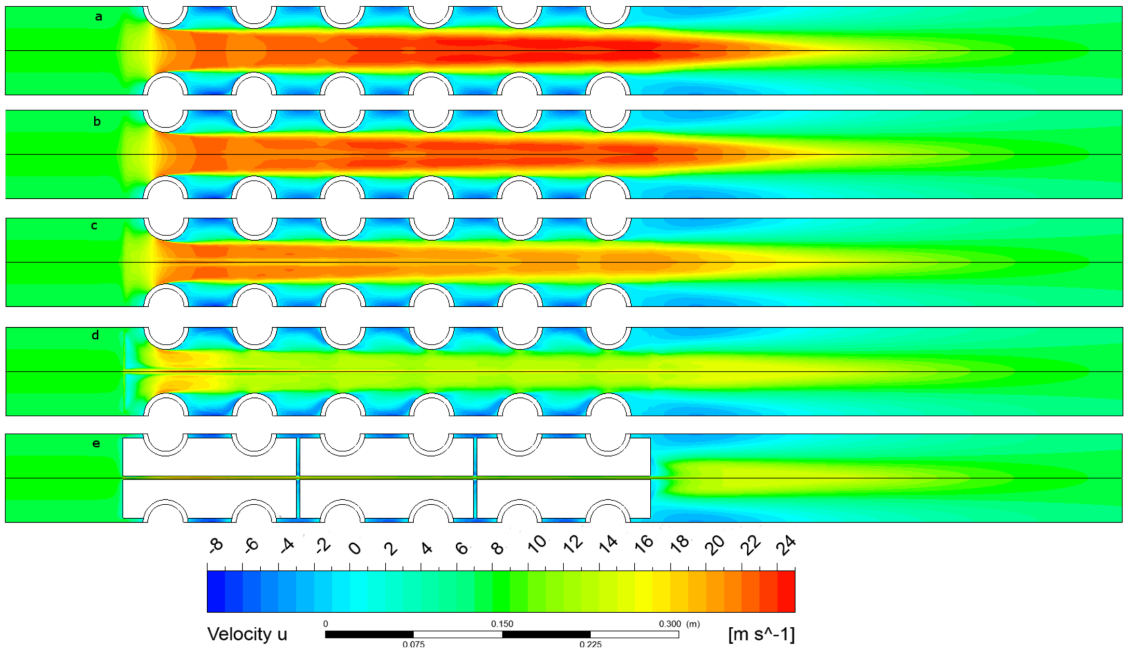

Figure 6.3. *Streamwise velocity contours normal to fins at different positions between fins. Picture a at $\frac{4}{8}$ times fin pitch, b at $\frac{3}{8}$ times fin pitch, c at $\frac{2}{8}$ times fin pitch, d at $\frac{1}{8}$ times fin pitch and e at fin symmetry plane.*

The streamwise velocity contours at different spanwise positions are given in the Fig. 6.4. It can be seen that the flow represents a duct flow between the fins quite early in flow length. The expected recirculation region between the tubes and after the last tube is also present in the figure.

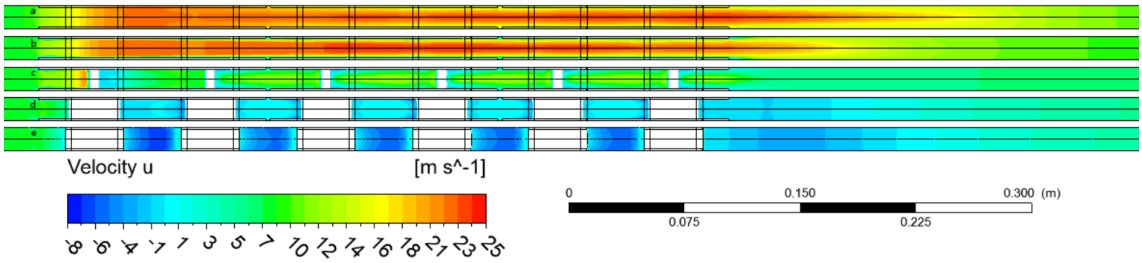

Figure 6.4. *Streamwise velocity contours at different spanwise positions. Picture a at transverse tube symmetry plane, b at $\frac{3}{8}$ times transverse pitch, c at $\frac{2}{8}$ times transverse pitch, d at $\frac{1}{8}$ times transverse pitch and e at transverse symmetry plane.*

The streamwise velocity contours at different spanwise positions at the middle of the tubes are given in the Fig. 6.5. The Fig. 6.5 show similar trend as earlier Figs. 6.3 and 6.4. At the first tube the low velocity region at the fin edge is still developing while at the second and the third tubes it diminishes until it disappears completely into a developing flow. The boundary layer development at tube wall and the fin wall is also shown in this figure. It can be seen that the velocity contours between 4th and 5th and 5th and 6th tubes have slightly different shape which means the flow is still developing.

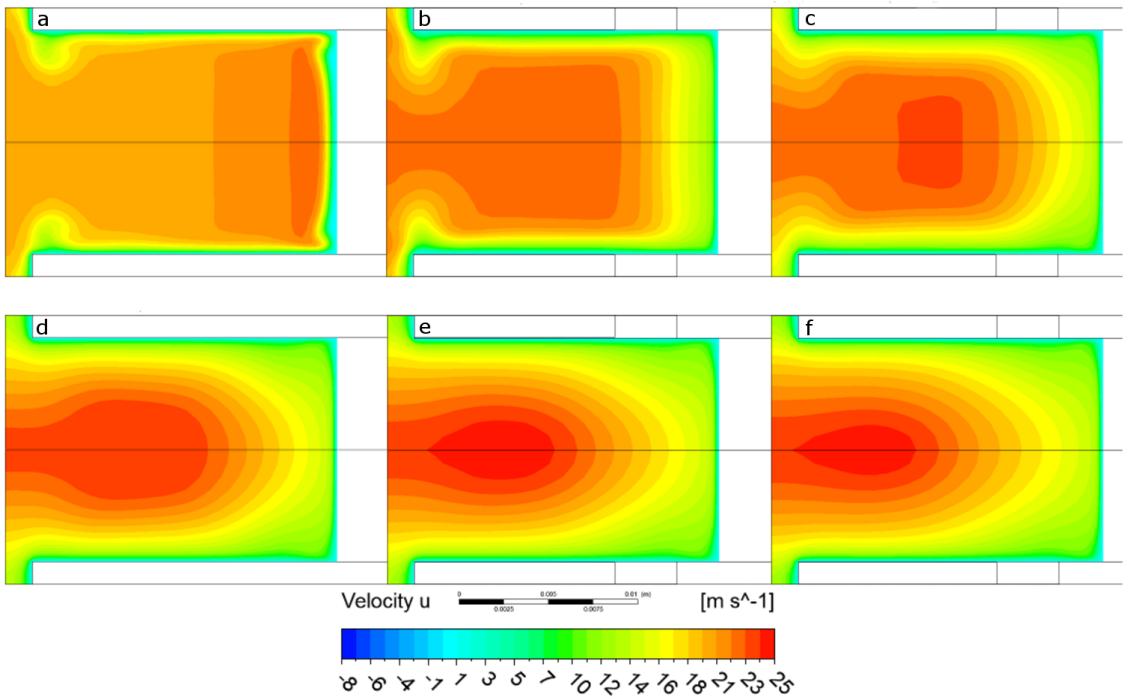

Figure 6.5. *Streamwise velocity contours at different streamwise positions between tubes. Picture a at 1st tube, b at 2nd tube, c at 3rd, d at 4th tube, e at 5th tube and f at 6th tube.*

The streamwise velocity contours at different streamwise positions between the tubes are given in Fig. 6.6. An interesting feature in the contours is at the fin edge where there is a low velocity region associated with a some kind of tip vortex which diminishes quite fast in the downstream. In downstream there is also a clear boundary layer development. Closer to the tube, the proximity of the tube dominates the flow pattern much more than the fin pitch. It can also be seen that the flow is still developing between the two last tubes.

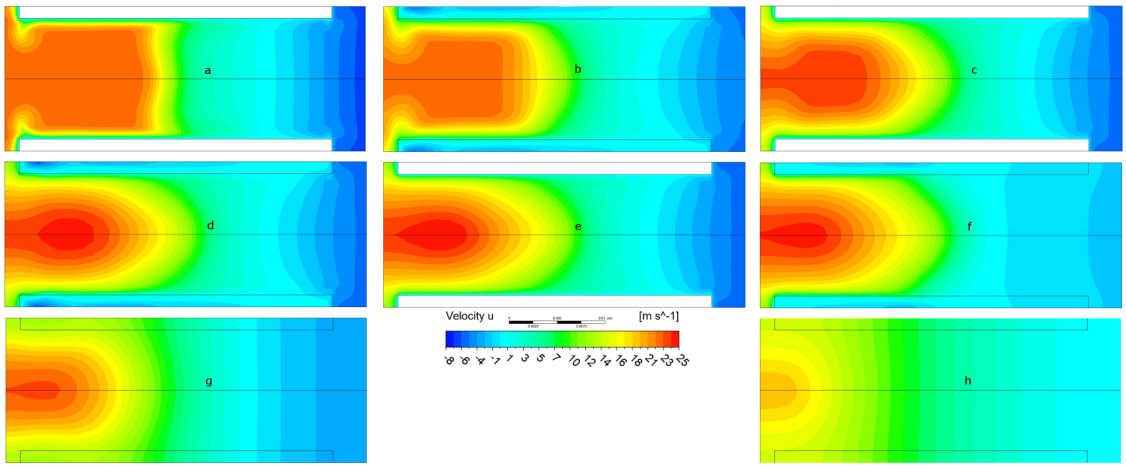

Figure 6.6. *Streamwise velocity contours at different streamwise positions between tubes. Picture a between 1st and 2nd tubes, b between 2nd and 3rd tubes, c between 3rd and 4th tubes, d between 4th and 5th tubes, e between 5th and 6th tubes, f just after last fin, g half longitudinal pitch downstream from last fin and h* $\frac{3}{2}$ *longitudinal pitches downstream from last fin.*

6.2 Temperature contours

Temperature contours can be used for visualising the overall temperature distribution in the flow. The distribution of the temperature and the development of the thermal boundary layers can be used for estimating the effectiveness of the heat transfer and the degree of mixing in the flow.

Fig. 6.7 shows the temperature distribution normal to the fins at different positions. Contour 6.7a suggests that the temperature drop due to heat transfer does not penetrate very well into free flow at symmetry plane between the fins. Contour 6.7c shows a rather high temperature drop penetration at fin edges, which is expected as there is slightly more heat transfer area normal to the fins due to minor gap between the fins. Contour 6.7d shows the low temperature region at the leading edge of the fin associated with recirculating region. The recirculation region between the tubes also shows low temperature levels due to low mixing with the duct flow between the tubes which means that there is low heat flux at the fin surface between the tubes.

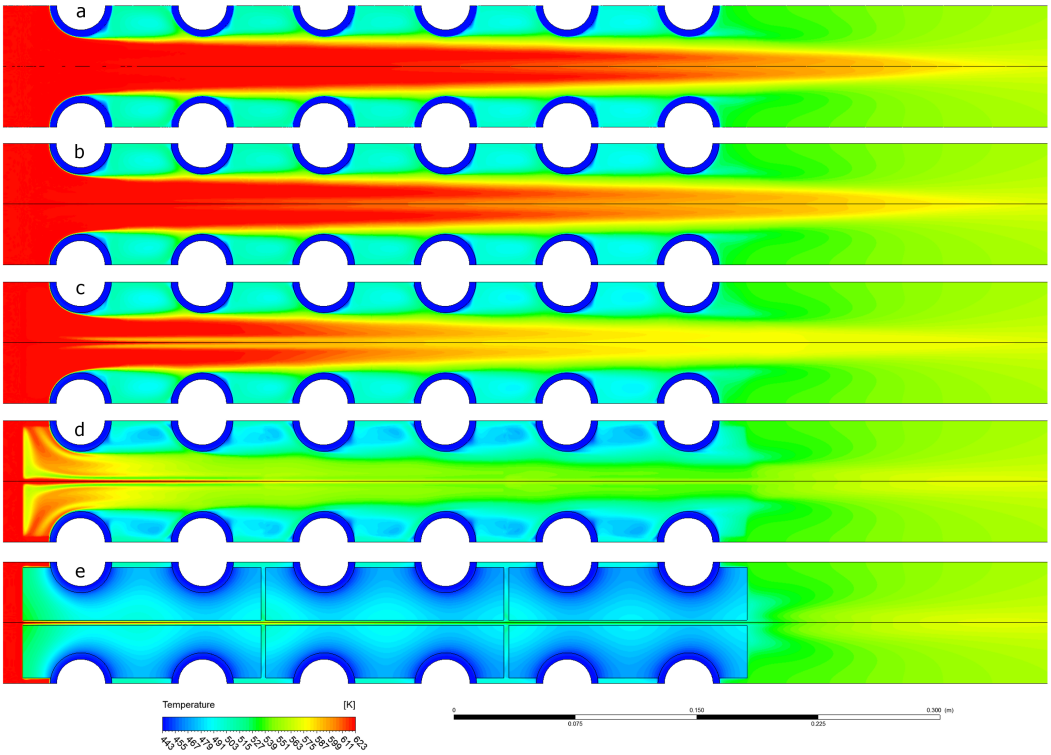

Figure 6.7. *Temperature normal to fins at different positions between fins. Picture a at* $\frac{4}{8}$ *times fin pitch, b at* $\frac{3}{8}$ *times fin pitch, c at* $\frac{2}{8}$ *times fin pitch, d at* $\frac{1}{8}$ *times fin pitch and e at fin symmetry plane.*

Figure 6.8 shows the streamwise temperature distribution at different spanwise positions. Figures 6.8a&b show a rather slow development of the thermal boundary layer. The core which is at the inlet temperature disappears just before the 5th tube. However, the temperature distribution is still developing at the trailing edge of the last finned tube. All figures also show the low temperature region due to recirculation caused by the sudden contraction at the fin system inlet.

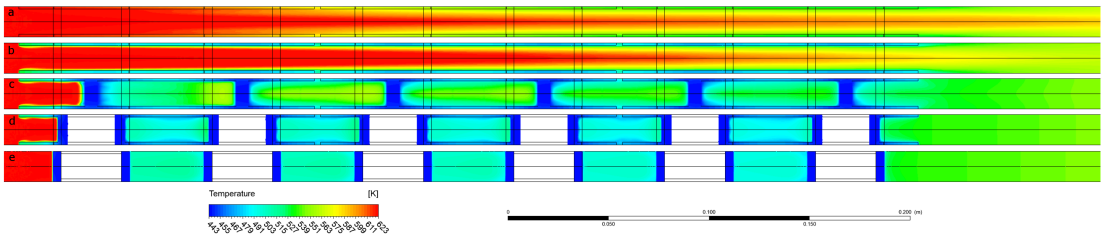

Figure 6.8. *Temperature contours at different spanwise positions. Picture a at transverse tube symmetry plane, b at* $\frac{3}{8}$ *times transverse pitch, c at* $\frac{2}{8}$ *times transverse pitch, d at* $\frac{1}{8}$ *times transverse pitch and e at transverse symmetry plane.*

By comparing the streamwise temperature contours at the Fig. 6.9 and velocity contours at the Fig. 6.5, it is evident, that after the accelerating region the temperature diffusivity is higher than momentum diffusivity as expected from Prandtl

number of 0.7 and low turbulence levels at inlet which lead into low turbulent diffusivity. It is hard to tell from this contour whether the temperature boundary layer is fully-developed as the heat transfer lowers the temperature at the core region.

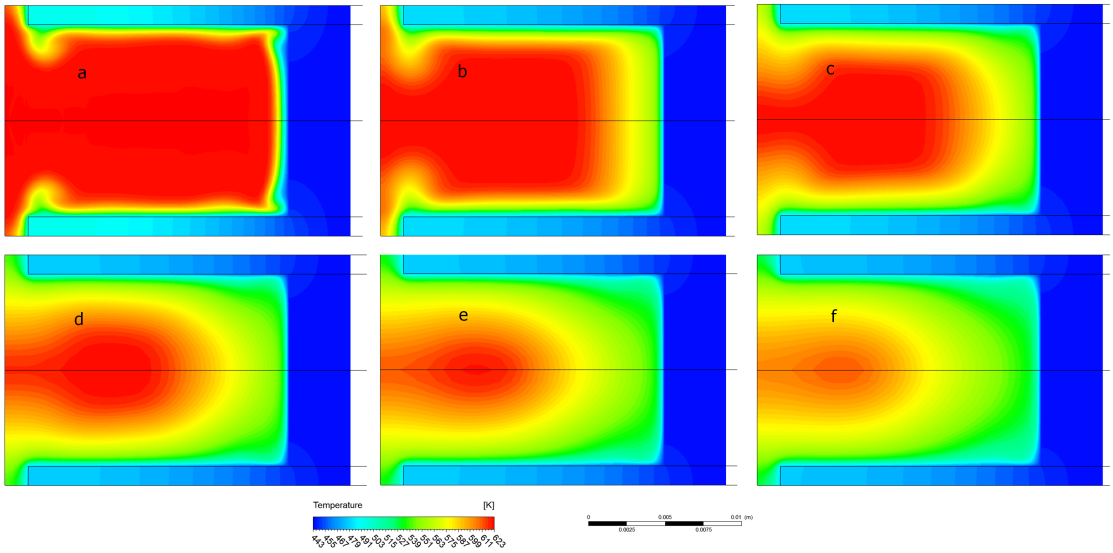

Figure 6.9. *Temperature contours at different streamwise positions between tubes. Picture a at 1st tube, b at 2nd tube, c at 3rd, d at 4th tube, e at 5th tube and f at 6th tube.*

The temperature contours at different spanwise positions between tubes are given in Fig. 6.10. Again, the contours are very similar to the velocity contours in the Fig. 6.6 but the development is slightly faster due to Prandtl number of 0.7 and low turbulence levels.

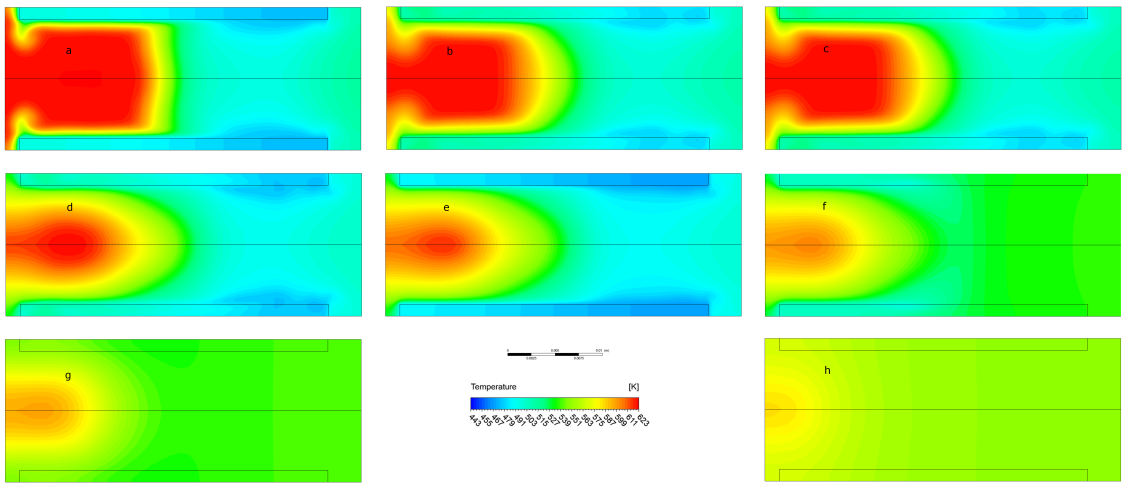

Figure 6.10. *Temperature contours at different streamwise positions between tubes. Picture a between 1st and 2nd tubes, b between 2nd and 3rd tubes, c between 3rd and 4th tubes, d between 4th and 5th tubes, e between 5th and 6th tubes, f just after last fin, g half longitudinal pitch downstream from last fin and h* $\frac{3}{2}$ *longitudinal pitches downstream from last fin.*

6.3 Velocity vectors and streamlines

Velocity vectors help to visualise the overall flow pattern and the developing flow in the channel between tubes. Vectors are also good way to visualise the jet-like behaviour after the finned tube system. The streamlines are used to visualise the recirculation region as the mass exchange between the main flow and recirculation region can be approximated with the number of streamlines entering and leaving the recirculation region and the number of cycles in recirculation region before leaving.

Figure 6.11 shows velocity vectors at multiple streamwise positions. Before the fin system the velocity profile has not changed almost at all. After that the flow starts to accelerate due to the diminishing flow area. There is a noticeable deviation in the velocity profile at the first tube compared to the other tubes which can be explained by higher v-velocity component caused by the first tube as it forces the flow between the tubes. Otherwise, the flow develops whole length of the finned tube system as the centre line velocity visibly increases even with decreasing density due to heat transfer. After the finned tube system the velocity profile evens out as a discharging jet.

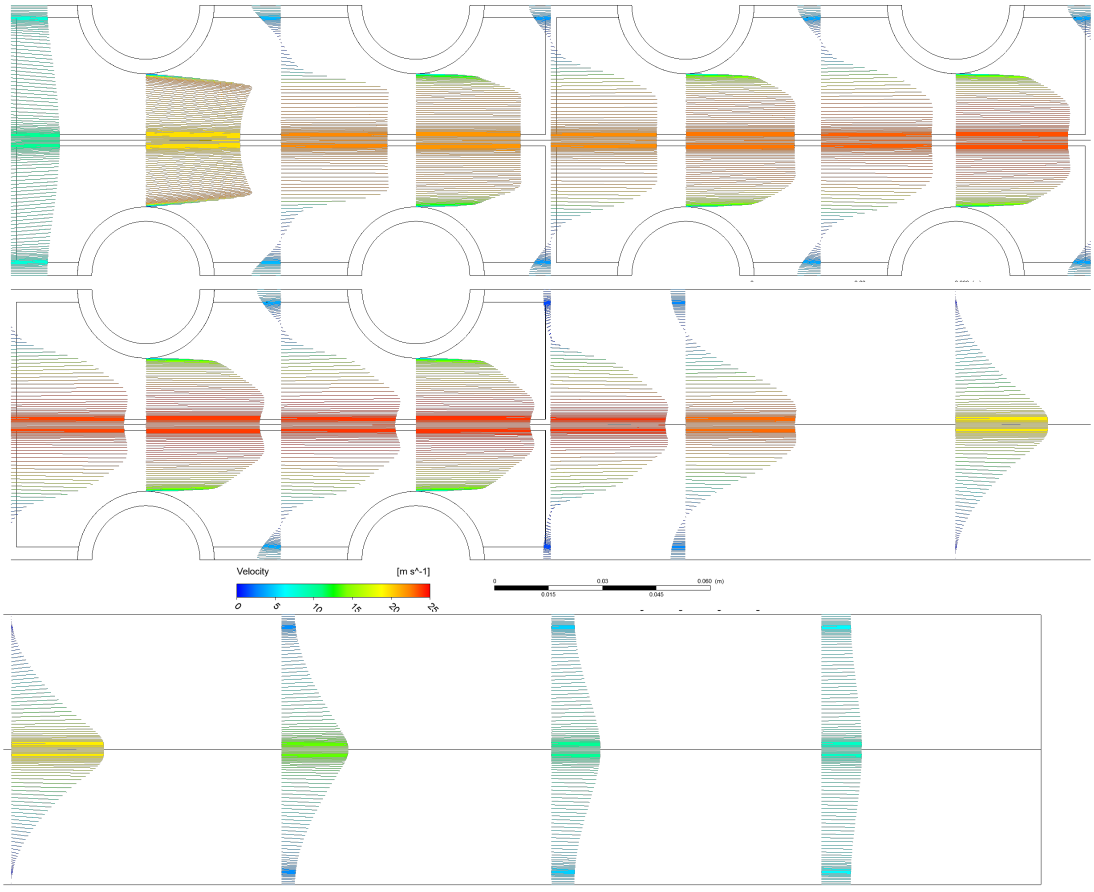

Figure 6.11. *Velocity vectors at symmetry plane between fins. Flow direction is from left to right and from up to down. The vectors after fin system are placed one longitudinal pitches apart from each other and the last row starts with the same vectors as the second row ends.*

The Fig. 6.12 shows the streamlines launched from the first recirculation region between the first and second tubes. There is very little mass transfer between the duct flow between the tubes and the recirculation regions as four streamlines never leave the circulation region and the other six circulate the whole region at low velocity at least once before leaving. Additionally, most of the streamlines that arrive to the circulation region originate close from the fin surface. This suggests that the heat transfer in the recirculation region is diffusion dominated as convection only transfers low temperature fluid in to the recirculation region. The heat transfer between the tubes could be increased by increasing the mixing with the main flow pattern. This might not be easy to achieve for in-line tube arrangement unless some kind of flow guides are used which might negatively impact the soot blowing.

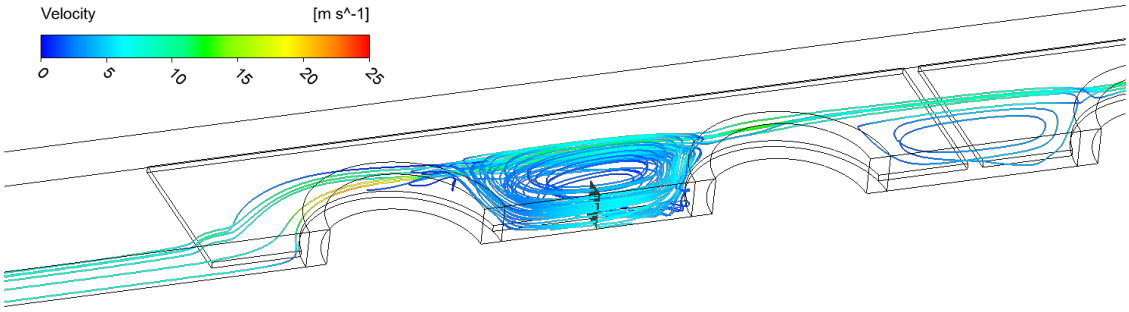

Figure 6.12. *Streamlines launched forward and backward from the first circulation region between tubes.*

Figure 6.13 shows streamlines at leading edge of the first fin. There is a noticeable recirculation region just at the leading edge of the first fin due to sudden contraction causing additional pressure loss. It might be possible to reduce this by sharpening the leading fin edge but this is not studied in this study. Most of the contraction, however, occurs due to tubes and as such sharpening the fins might actually have quite conservative effect on the pressure drop.

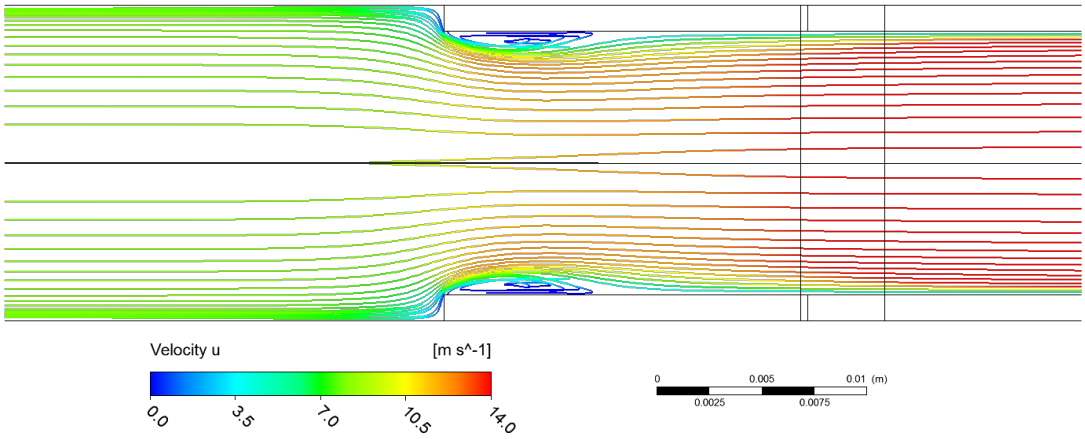

Figure 6.13. *Streamlines launched backward from a line at first tube in $\frac{3}{8}$ transverse pitch position.*

6.4 Surface contours at fin and tube surface

The dimensionless temperature $\frac{T_x - T_{fin}}{T_x - T_{wall}}$ where T_x is given by equation (4.15) gives an overall view of the fin efficiency in this geometry. The surface heat flux contours give the overall fin performance as it directly shows from where the most of the heat is transferred to the finned tube system. The wall shear contour gives and overall view which parts of the finned tube system contributes the most to the viscous pressure drop.

Figure 6.14 shows the dimensionless temperature difference at the surface of the first fin. Only the first fin has distinctly different temperature profile due to the high heat transfer on the leading edge as the tube forces the flow between the tubes. Other fins have very similar temperature profiles to the fin surrounding the second tube in the picture.

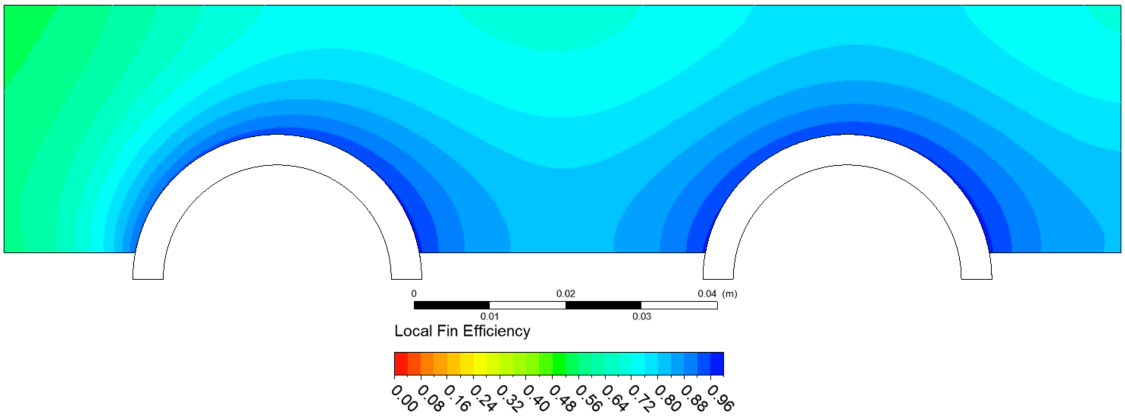

Figure 6.14. *Dimensionless temperature difference at the surface of the first fin. Flow direction is from left to right.*

Figure 6.15 shows the heat flux at the surface of the fin and the tube. The difference in the temperature profile surrounding the leading edge of the first fin in the Fig. 6.14 is easy to explain with the higher heat flux at the leading edge. Otherwise, the fin area between the tubes shows a rather low heat flux while the fin at the area where the main flow occurs, shows medium heat flux. The highest heat flux occurs at the tube front surface. Another interesting feature is that the fin behind the last tube has a rather high heat flux compared to the fin area between the tubes. While the heat flux scale was truncated to the zero at the low end, small areas of the blue area with zero heat flux had actually slightly negative heat flux.

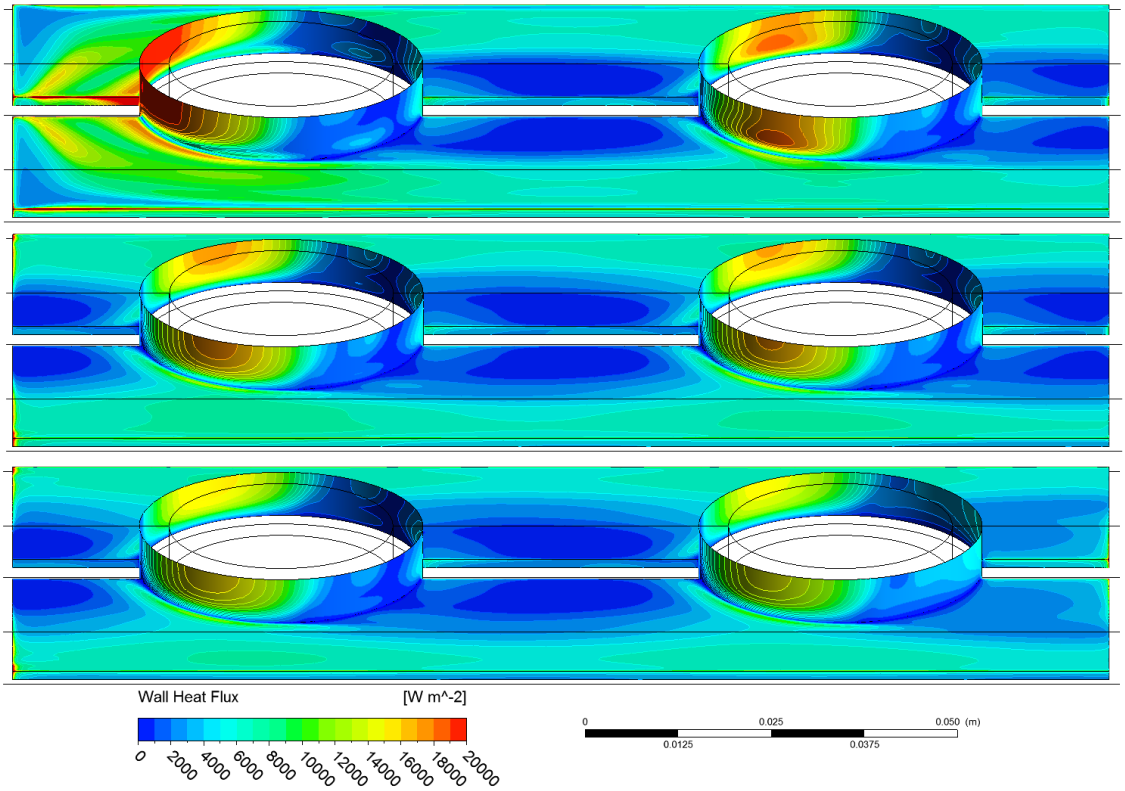

Figure 6.15. *Heat flux at the surface of the fin and the tube. The flow direction is from left to right and fins are arranged in order from up to down.*

Shear stress contours in the Fig. 6.16 show a similar pattern as the heat flux contour as expected. In all situations the heat transfer seems to follow the shear stress, however, the shear stress seems to lag somewhat to downstream.

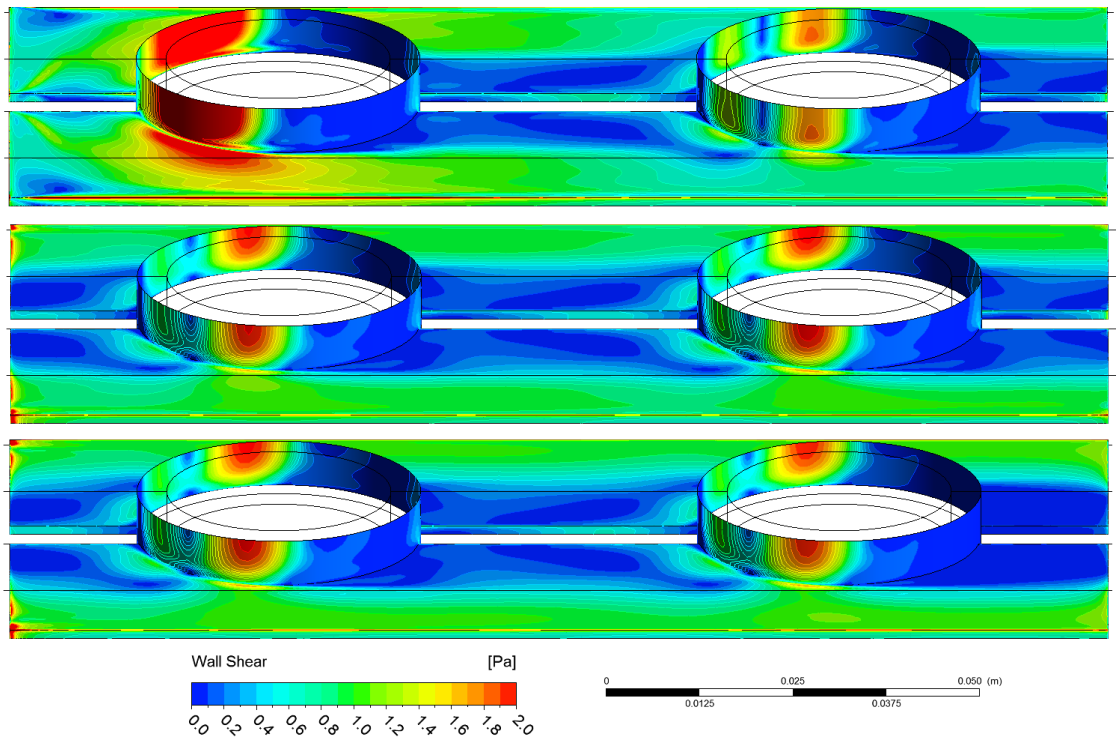

Figure 6.16. *Shear stress at the surface of the fin and the tube. The flow direction is from left to right and fins are arranged in order from up to down.*

6.5 Velocity profiles

The velocity profiles for a 3D flow may not be as helpful as for simple 2D flows but they are nevertheless useful in assessing whether the flow is laminar or turbulent in nature. The velocity profile for simple laminar flow assumes a parabolic profile (6.1) while the turbulent profile can be given as a power law (6.2) (White, 2009, Chapter 4.10). Usually a power of $\frac{1}{7}$ is used in turbulent profile but it is known that it might be as low as $\frac{1}{5}$ for low Reynolds number turbulent flow. The temperature profiles are given in the Appendix C while the boundary layer development is given in the Appendix D.

$$\frac{V}{V_{center}} = 1 - \left(\frac{2z}{P}\right)^2 \tag{6.1}$$

$$\frac{V}{V_{center}} = \left(1 - \frac{2z}{P}\right)^{\frac{1}{n}} \tag{6.2}$$

Figure 6.17 shows the velocity profiles at the each tube, a $\frac{3}{8}$ transverse pitch away from tube symmetry. At first tube the velocity profile is similar to the flat plate

boundary layer. At the tube 4 the opposite profiles meet at the symmetry plane and the velocity profile is somewhat similar to the turbulent pipe flow. Further away in downstream the turbulent velocity profile develops and the velocity gradient at wall decreases slightly but with 6 tubes the fully-developed region is never achieved.

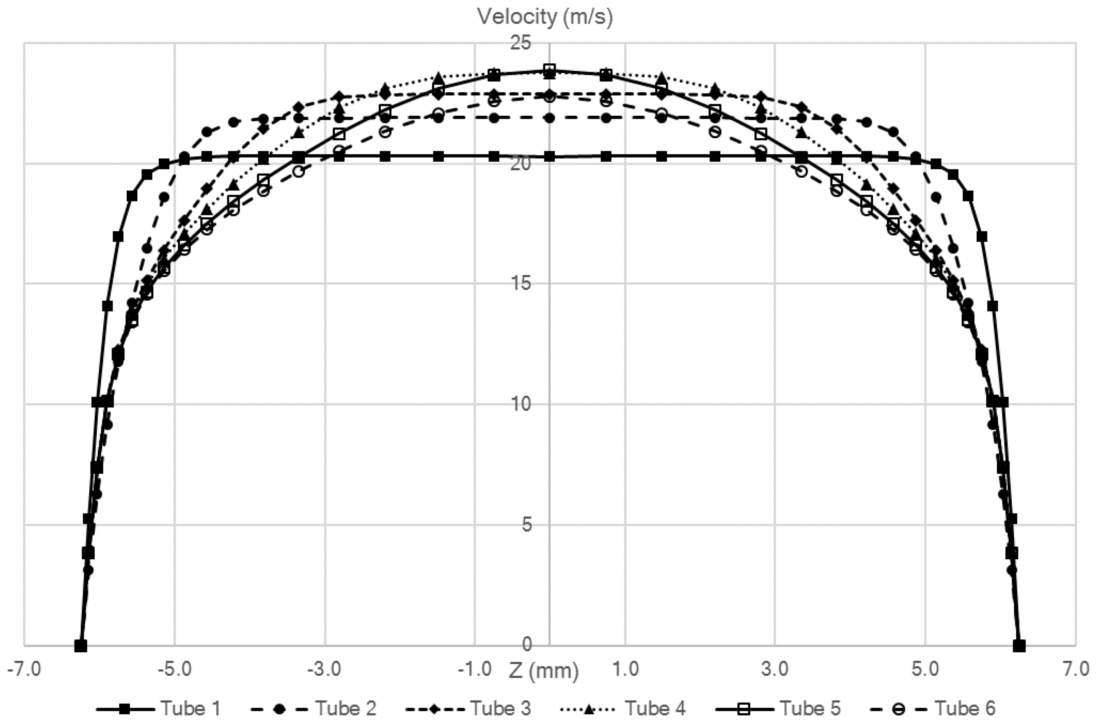

Figure 6.17. *Velocity profiles at $\frac{3}{8}$ transverse pitch away from tube symmetry line at each tube.*

The Fig. 6.18 shows the dimensionless velocity profiles at the two last tubes, a $\frac{3}{8}$ transverse pitch away from tube symmetry. The normalisation is done with fin pitch for z direction and centre line velocity for velocity at each tube. Additionally, the velocity profiles for simple 2D laminar flow and turbulent flows with 2 different powers are given for comparison. The closest match for power fit is achieved with the power of $\frac{1}{5}$ which corresponds the low Reynolds number turbulent flow such as this.

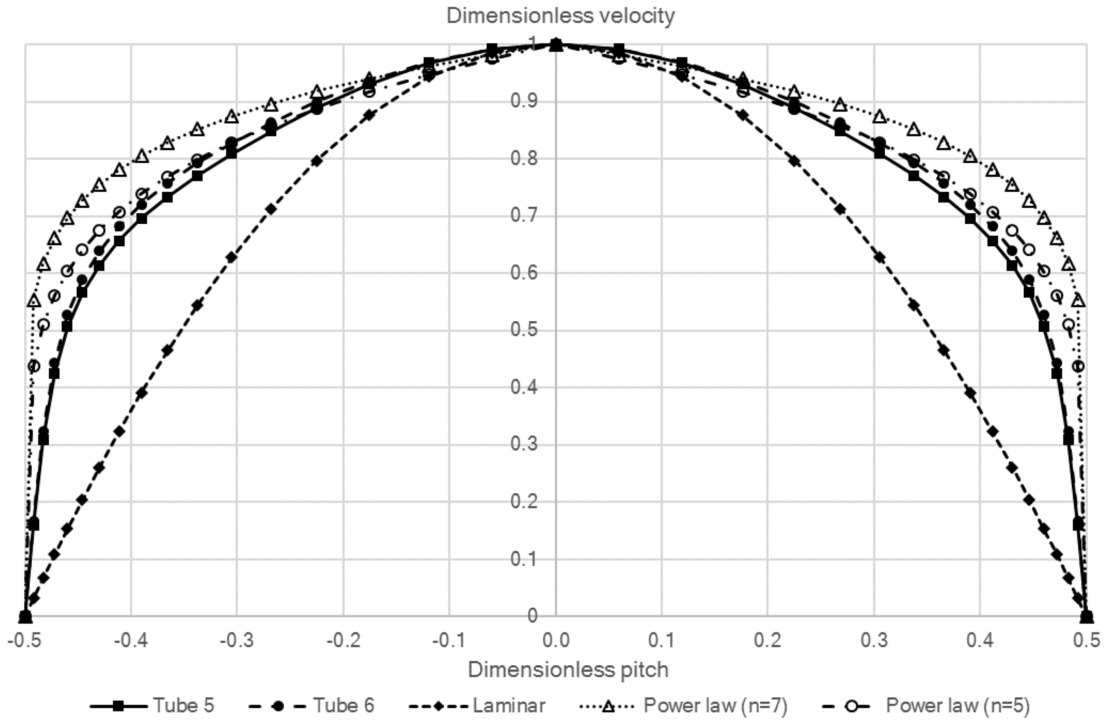

Figure 6.18. *Dimensionless velocity profiles at $\frac{3}{8}$ transverse pitch away from the tube symmetry plane at two last tubes.*

6.6 Darcy's friction factor and heat transfer coefficient

Darcy's friction factor at the fin surface was calculated from wall shear at $\frac{3}{8}$ transverse pitches away from tube symmetry line by using average velocity at the smallest cross section in the equation (6.3). The heat transfer coefficient was calculated according to the equation (2.12) by replacing the T_{infty} by T_x from the equation (4.16). This value is compared to the correlations from the laminar and turbulent flat plate flows and developing and fully-developed turbulent channel flows at the $\frac{3}{8}$ transverse pitches away from tube symmetry line.

$$f_D = \frac{4\tau_w}{\frac{1}{2}\rho V^2} \tag{6.3}$$

Friction factor and comparison to correlations are shown in Fig. 6.19. At the start of the finned tube system there is a significant deviation from the flat plate correlations due to recirculation region caused by sudden contraction at the fin leading edge. After the re-attachment, the flow develops with a similar slope to Blasius laminar solutions. The value similar to fully-developed friction factor from Moody's chart is assumed at 0.12 m which was the same point as the boundary layer thickness rapidly increases in the Appendix D.

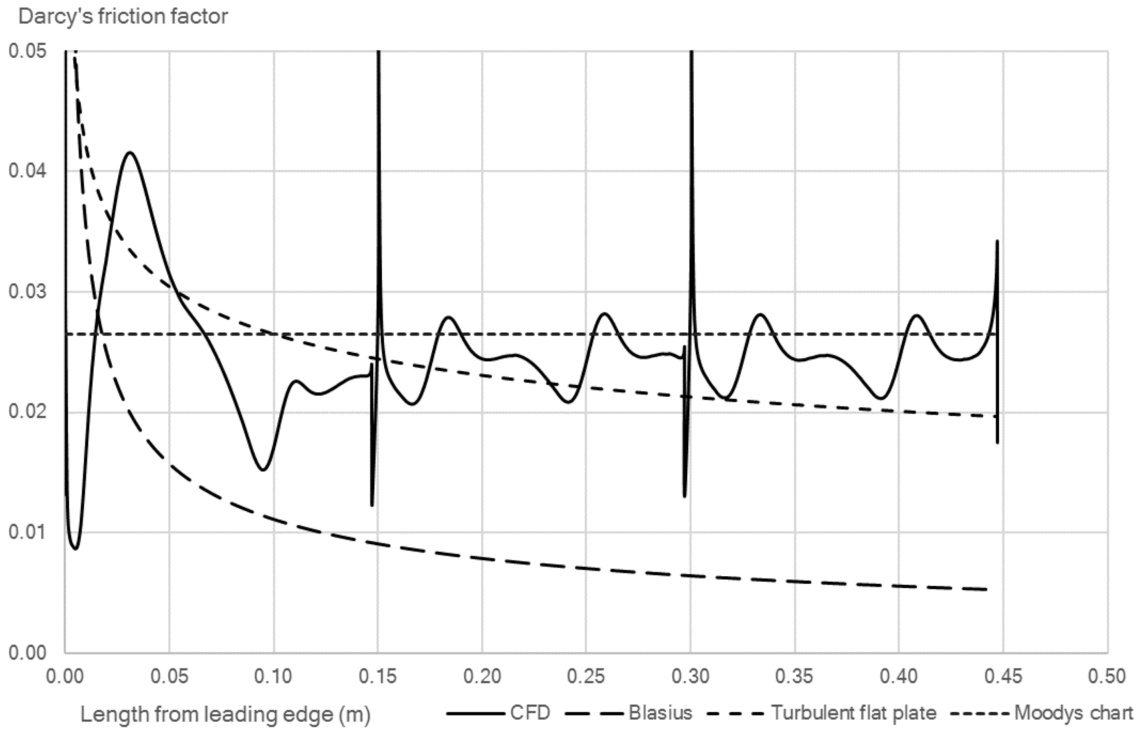

Figure 6.19. *Friction factor at $\frac{3}{8}$ transverse pitch from tube symmetry.*

The heat transfer coefficients from CFD and comparison to the correlations at $\frac{3}{8}$ transverse pitches from tube symmetry are presented in the Fig. 6.20. The heat transfer coefficient was calculated with the heat flux and fin temperature from the CFD solution with the temperature in streamwise direction approximated with the equation (4.16). For correlations the double of the fin pitch is used as characteristic dimension and the velocity in the smallest cross-section as the characteristic velocity. The friction factor used in Gnielinski correlation was extracted from CFD as an average friction factor. The closest match with CFD solution is achieved with Dittus-Boelter correlation. The Gnielinski correlation is for some reason way off while the CFD solution is somewhere between the flat plate laminar and turbulent correlations. However, it should be kept in mind that these correlations are not developed for a complex geometry like this.

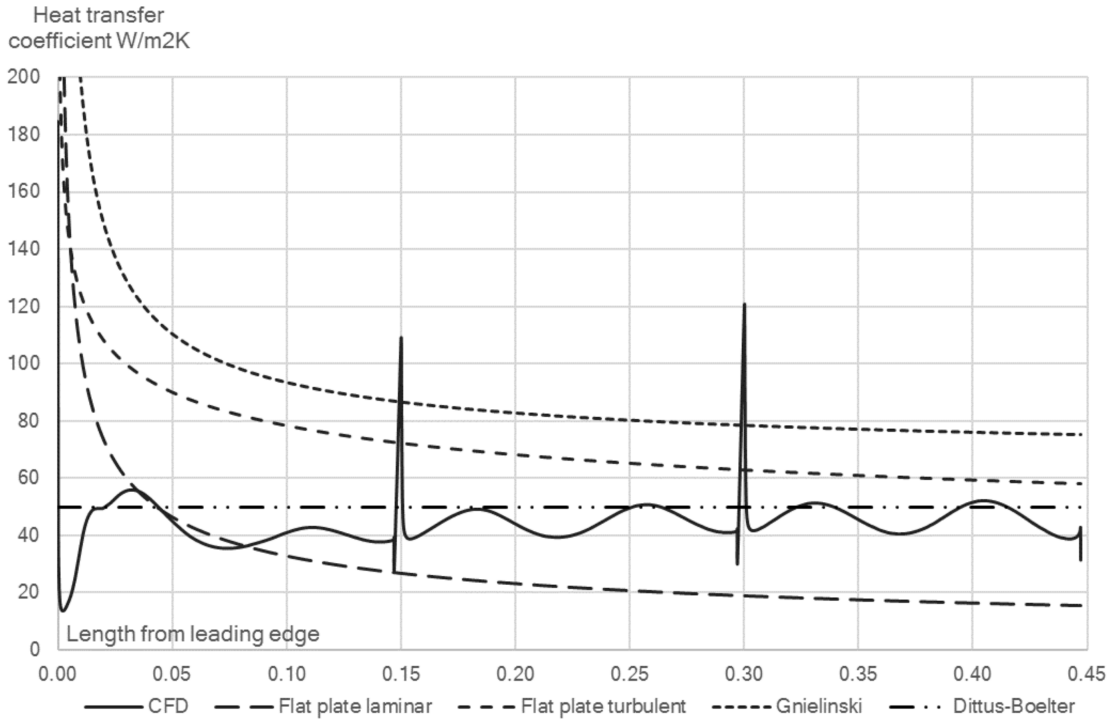

Figure 6.20. *Heat transfer coefficient at $\frac{3}{8}$ transverse pitch away from the tube symmetry plane.*

As the friction factor and the heat transfer coefficient in the channel between the tubes are relatively constant, after the developing region, it may be possible to approximate the thermal hydraulic performance of the in-line finned tube assembly with quite simple correlations. The fin area in the channel flow between the tubes has a rather constant heat transfer coefficient while the recirculation region has less than half of the heat flux of the fin area in the channel. Thus the conjugate heat transfer could be reduced in to calculating the fin temperature profile with a simple heat transfer coefficient correlation and integrating the resulting heat flux over the whole surface. The friction factor of the fin area at the channel between the tubes also seems to agree with the Moody's chart smooth wall values suggesting that the viscous drag could be approximated by integrating the friction over fin area at the channel between the tubes. Additionally, there would be pressure drop associated with a form drag which could be approximated with a cylinder form drag correlations.

6.7 Estimation of the inlet and outlet loss coefficients

As the inlet and outlet loss coefficients are needed in calculation of the Fanning friction factor of the heat exchanger core from the equation (2.16), the entrance and exit loss coefficients have to be estimated. There are figures in (Kays and London, 1964, p. 92-94) which can be used to develop correlations for different contraction ratios but there is no loss coefficient figure for a finned tube heat exchanger. As such

the flat duct and tube bundle figures are used to get best match for loss coefficients by matching the pressure data from CFD solution with the equation (2.16).

The Fig. 6.21 show the evolution of the static pressure through the computational domain of case 1 with 8 $\frac{m}{s}$ inlet velocity. The fin leading edge is at 100 mm after which there is first contraction at 103 mm as the flow is forced between the fins. The second contraction as the flow is forced between the tubes occurs between the 1st and 2nd tube at 172 mm. After the inlet effects the pressure gradient in the heat exchanger core is a relatively constant even when accounting slight contraction and expansion at the tubes.

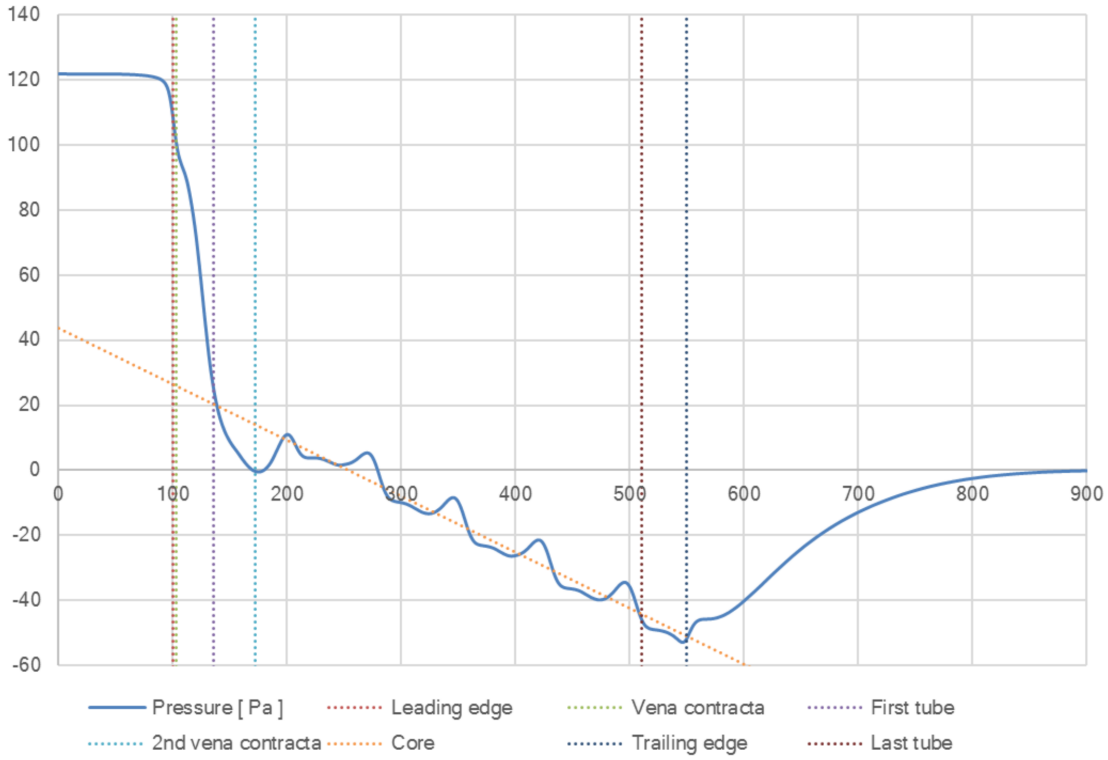

Figure 6.21. *The static pressure evolution through the finned tube heat exchanger core at 3/8 transverse pitches away from the tube symmetry.*

In the Table 6.1 the static pressure changes at inlet, heat exchanger core and outlet are presented. The reversible part of the static pressure drop is calculated according to the Bernoulli's equation (2.15). For the inlet and outlet the reversible part is due to the change in cross-section while for the core it is due to the change in density. The rest is irreversible static pressure drop which is accounted in the loss coefficient in the equation (2.16). (Shah and Sekulic, 2003, Chapter 6.2.1) The best fit for the loss coefficient was found with tube bank loss coefficients when the contraction ratio only for the tube contraction was used i.e. $\sigma_{loss} = \frac{S_T - D}{S_T}$ which in this case was 0.49. The inlet loss coefficient was 7 % higher and the outlet was 2 % lower than the correlation but as the inlet and outlet contributes only $\frac{1}{3}$ of total pressure drop the total error is only 2 % in pressure drop calculation.

Table 6.1. *The pressure changes due to reversible and irreversible mechanisms in the heat exchanger core.*

Position	$\Delta p(Pa)$	$\Delta p_{rev}(Pa)$	$\Delta p_{irrev}(Pa)$	K_c, Eu, K_e
Inlet	121.8	84.8	24.4	0.24
Core	65.0	-19.6	84.6	0.14
Outlet	-52.4	-76.7	24.3	0.26

The correlations for inlet and outlet loss coefficients are given in the equations (6.4) and (6.5). It should be noted that, while these may not be exact for all cases, the error is negligible due to the low contribution of the loss coefficients to the total pressure drop. Additionally, as the pressure drop increases in higher power as the heat transfer, the error in friction factor estimation does not affect that much to the heat exchanger dimensioning.

$$K_c = 0.42 - 0.335\sigma_{loss} \tag{6.4}$$

$$K_e = 0.965 - 1.895\sigma_{loss} + 0.875\sigma_{loss}^2 \tag{6.5}$$

7. THE EFFECT OF THE GEOMETRIC PARAMETERS

In the finned tube geometry considered in this study there were ten geometric parameters (tube per fin, tubes in row, tube diameter, longitudinal pitch, transverse pitch, fin pitch, fin thickness, slit width, the gap between fins and tube wall thickness) which could have been varied in this study. From those tube wall thickness was deemed to be insignificant for the heat transfer coefficient and friction factor and tubes in row was deemed unfeasible from the computational resource point of view.

In the Appendix H, all cases are plotted to get an overall picture of the variation of the dimensionless numbers. Most notably the fin efficiency seems to account the most of the variation in the overall heat transfer coefficient U i.e. the $h = \frac{U}{\eta_0}$ is rather constant for similar flow velocity in the smallest cross-section.

All figures of j-factor in this chapter has been plotted with the overall heat transfer coefficient defined as $U = \eta_0 h = \frac{Q}{A_h \Delta T_{lm}}$, a Reynolds number based on the tube diameter and properties at average fluid temperature. The heat transfer coefficient was chosen as $U = \eta_0 h$ as the effect of the combined heat conduction in the fin and the convective heat transfer outside the fin is usually the parameter of interest in heat exchanger thermal dimensioning. If the material of the fin is changed, the figures are no longer accurate, however, they would still give the overall direction of the change in the heat transfer.

The figures of Fanning friction factor has been calculated with the equations (2.16), (6.4) and (6.5) to separate the inlet and outlet effects from the frictional pressure drop. If the inlet and outlet effects would not have been subtracted from the total static pressure change, the averaged Fanning friction factor would have been valid only for the calculated case with six tubes in row. However, the friction factor still depends on the flow length due to the flow development and the friction factor may not bee strictly accurate if a different number of tubes in row is used. The equation (2.16) was chosen as the typical literature analogies (Reynolds and Colburn-Chilton), relating the heat transfer to the friction, use the surface friction to relate the heat transfer and friction. The Fanning friction factor calculated from the equation (2.16) still includes the form drag associated with the tubes and fins. The surface friction can be approximated (according to the results in this study) by assuming that the surface friction is around 25 % of the friction factor calculated from the equation (2.16).

7.1 The effect of the fin pitch

The fin pitch can be regarded as one of the most important geometric variables when finned tube geometry is considered. For low fin pitches the heat transfer area per volume is high producing a compact heat exchanger with flow similar to channel flow between the fins while for high pitches the behaviour of the heat exchanger is expected to approach that of a tube bank heat exchanger.

The Fig. 7.1 shows the Colburn number as a function of the Reynolds number. An interesting feature is the fact, that below Reynolds number of 10 000, 10 mm fin pitch intersects with 15 mm and 20 mm fin pitches. Most probably the 10 mm fin pitch would intersect even with 30 mm fin pitch if even lower Reynolds numbers were used. This suggests that the most compact finned tube heat exchangers have the highest heat transfer coefficient at low Reynolds numbers while for higher Reynolds numbers the higher pitches provides the highest heat transfer coefficient. However, it should be noted that while the low fin pitches might have lower heat transfer coefficient at high Reynolds numbers, the conductance per mass and volume is still usually higher due to a higher surface density.

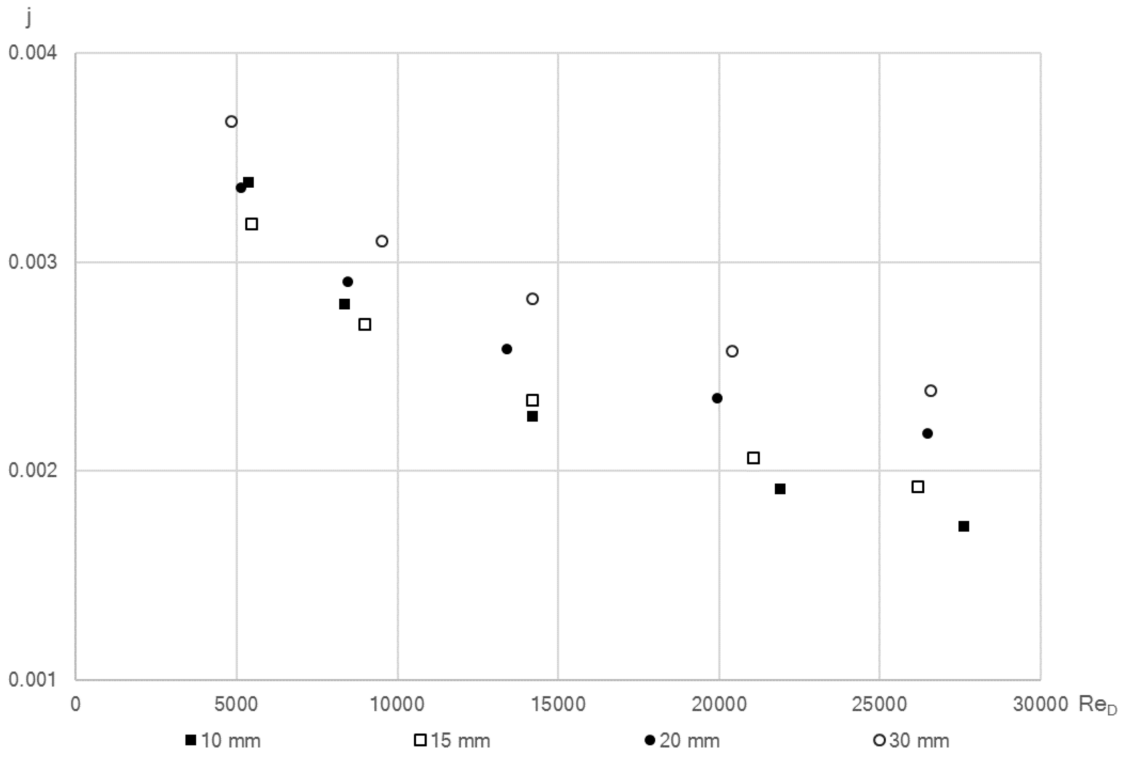

Figure 7.1. *Colburn number as a function of the Reynolds number for varying fin pitches.*

The Fanning friction factor shows similar trend to Colburn j-factor in Fig. 7.2. The most notable difference is the fact that while the Colburn j-factor decreases at higher Reynolds numbers, the Fanning friction factor decreases only slightly suggesting that the area-goodness decreases at higher Reynolds numbers. The odd behaviour

in both friction factor and j-factor where the lower pitch intersects with higher pitches is most likely due to using tube diameter as a characteristic dimension for the Reynolds number as it does not account the change in flow dynamics in any way. If the hydraulic diameter would have been used as a characteristic dimension, the lower pitches would have had lower Reynolds number and thus translating the curves to left. This would have given a figure with all pitches in order at whole Reynolds number range.

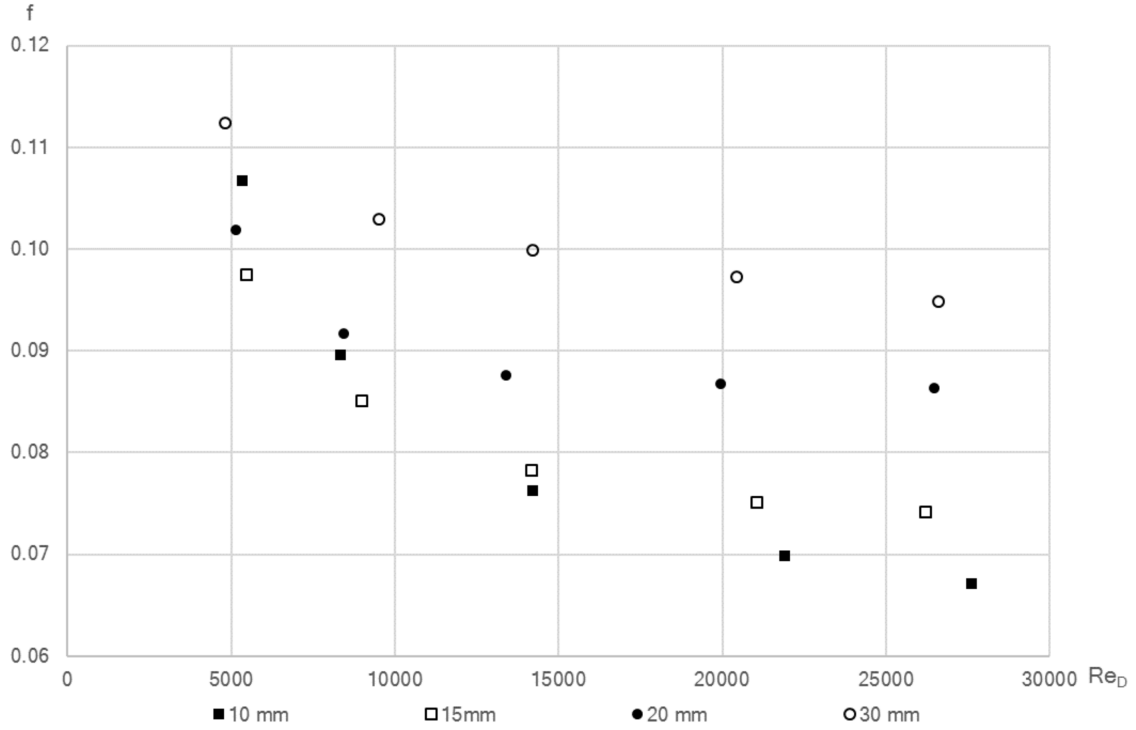

Figure 7.2. *Fanning friction factor as a function of the Reynolds number for varying pitches.*

7.2 The effect of the transverse pitch

Transverse pitch is another important parameter in finned tube design. Increasing of the transverse pitch directly increases the fin surface area which should lead into decrease of the fin efficiency. Increasing the transverse pitch also increases the mass ratio of the fin to tube which might be desirable in some situations.

The Fig. 7.3 shows the variation of the Colburn j-factor with the transverse pitch. As expected, the increased transverse pitch decreases the j-factor due to lower fin efficiency.

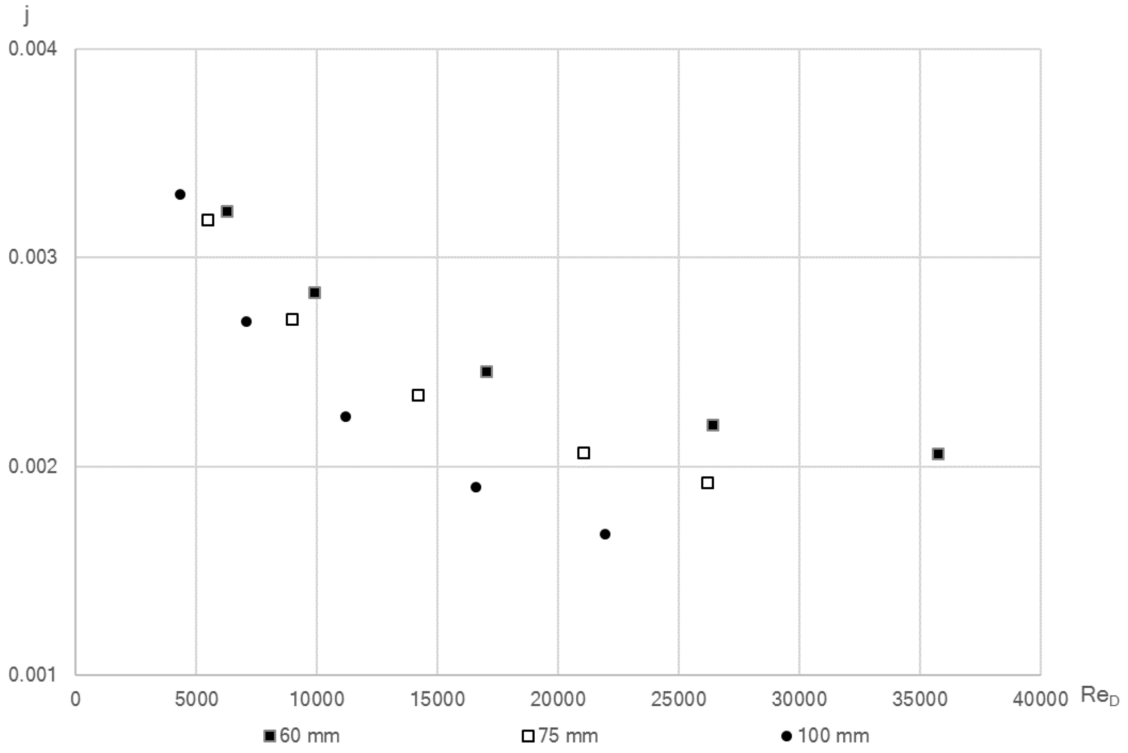

Figure 7.3. *Colburn j-factor as a function of the Reynolds number for varying transverse pitches.*

The variation of the Fanning friction factor for varying transverse pitches is shown in a Fig. 7.4. The general trend seems to be that the higher transverse pitches lead into a higher friction factor suggesting that the fin surface in the channel between the tubes dominates the friction characteristics of the finned tube design. Additionally, at high Reynolds numbers all transverse pitches seem to converge into a value between 0.07 and 0.08.

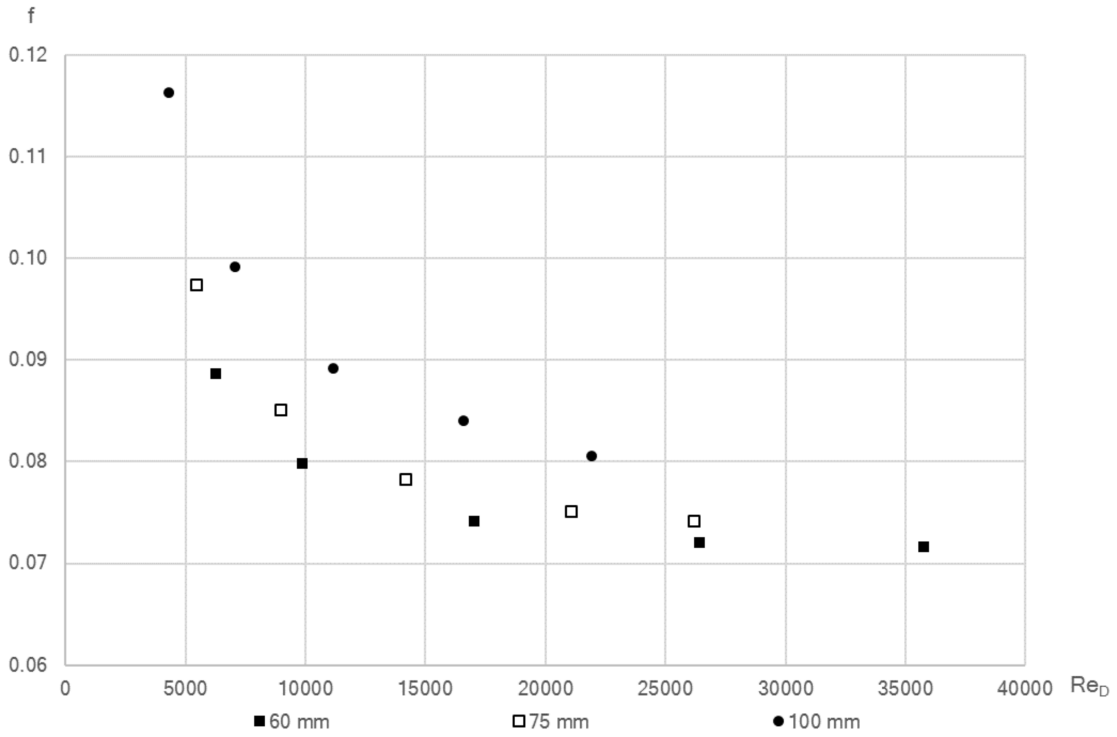

Figure 7.4. *Fanning friction factor as a function of the Reynolds number for varying transverse pitches.*

7.3 The effect of the longitudinal pitch

The longitudinal pitch in the fin-tube design acts similarly to the transverse pitch but some of the increased fin area will be shadowed by recirculation region between the tubes where the heat flux is lower due to lower temperature and velocity. Additionally, the longitudinal pitch affects the bend radius of the tubes for cross-flow heat exchangers which is an important parameter from the manufacturing point of view.

The Fig. 7.5 shows a similar trend for varying the longitudinal pitch as for varying the transverse pitch. Higher longitudinal pitches seems to decrease the area-averaged j-factor which is most likely due to a higher ratio of the developing region to the total flow length as the developing region has higher heat transfer coefficient.

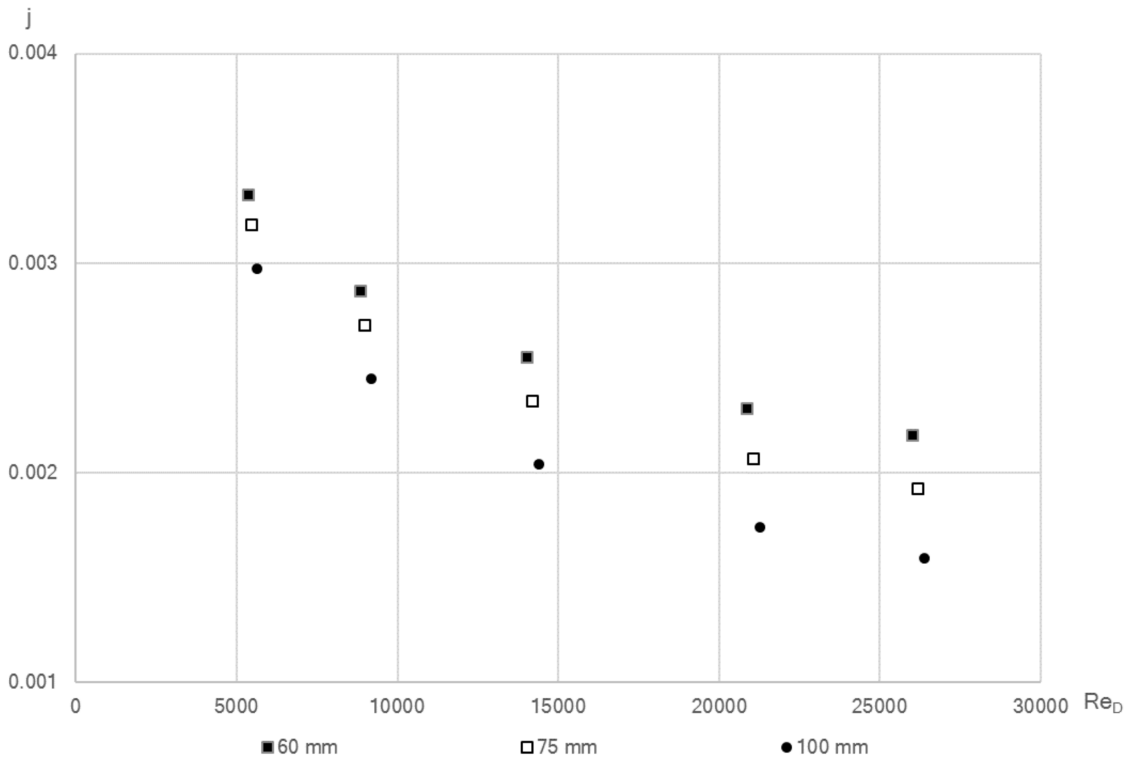

Figure 7.5. *Colburn j-factor as a function of the Reynolds number for varying longitudinal pitches.*

The friction factor increases as the longitudinal pitch is decreased as seen in Fig. 7.6. The longitudinal pitch has a direct impact on flow length when tube number is kept constant and as such it affects the fraction of the flow in developing region. The developing flow has much higher friction factor than the fully-developed flow which explains the fact that the area-averaged friction factor is higher for lower longitudinal pitches.

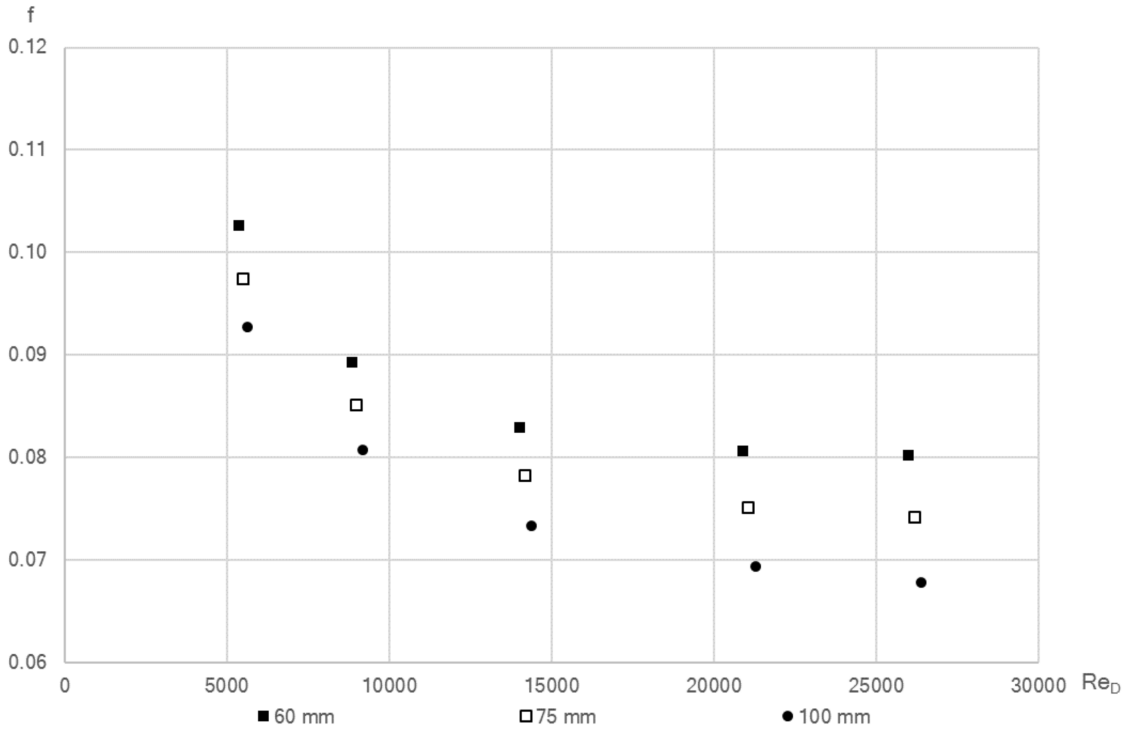

Figure 7.6. *Fanning friction factor as a function of the Reynolds number for varying longitudinal pitches.*

7.4 The effect of the tube diameter

The tube diameter is the most important parameter in the finned tube design the tube acts as a support to the whole finned tube heat exchanger while simultaneously usually being the most expensive part in the structure. The tube surface also acts as the primary heat transfer area. It also holds the medium to/from the heat is transferred from/to the outer side.

There seems to be a very similar trend to increasing the tube diameter as to decreasing transverse and longitudinal pitches in Fig. 7.7. This is expected as increasing the tube diameter and decreasing the tube pitches both decreases the ratio of the fin size to tube diameter. The effect is actually really close to the changing of the transverse pitch.

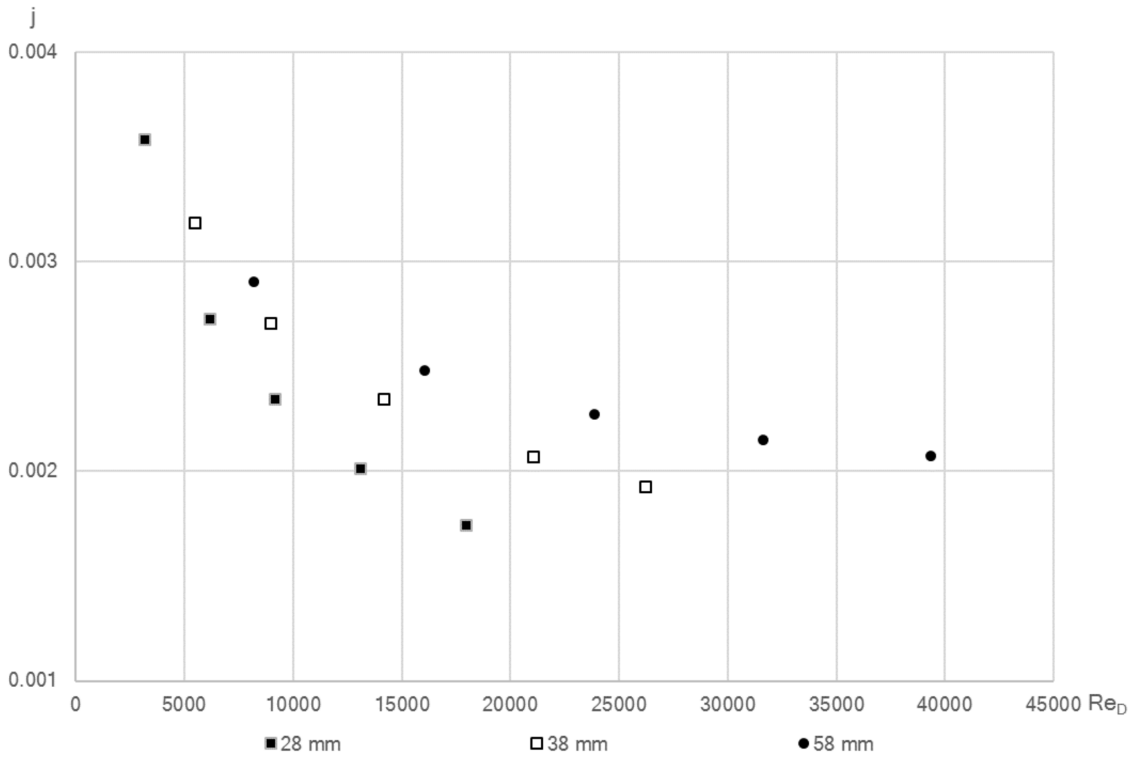

Figure 7.7. *Colburn j-factor as a function of the Reynolds number for varying tube diameters.*

Decreasing the tube diameter seems to affect very similarly to the increasing the transverse and longitudinal tube pitches. Figures 7.8, 7.6 and 7.4 suggests that the fin area in the channel between the tubes has a much higher influence to the friction and heat transfer characteristics of the finned tube system than the fin area in the recirculation region. This is expected as the velocity in the recirculation region between the tubes is much lower than in channel between the tubes, contributing less to the area averaged friction factor.

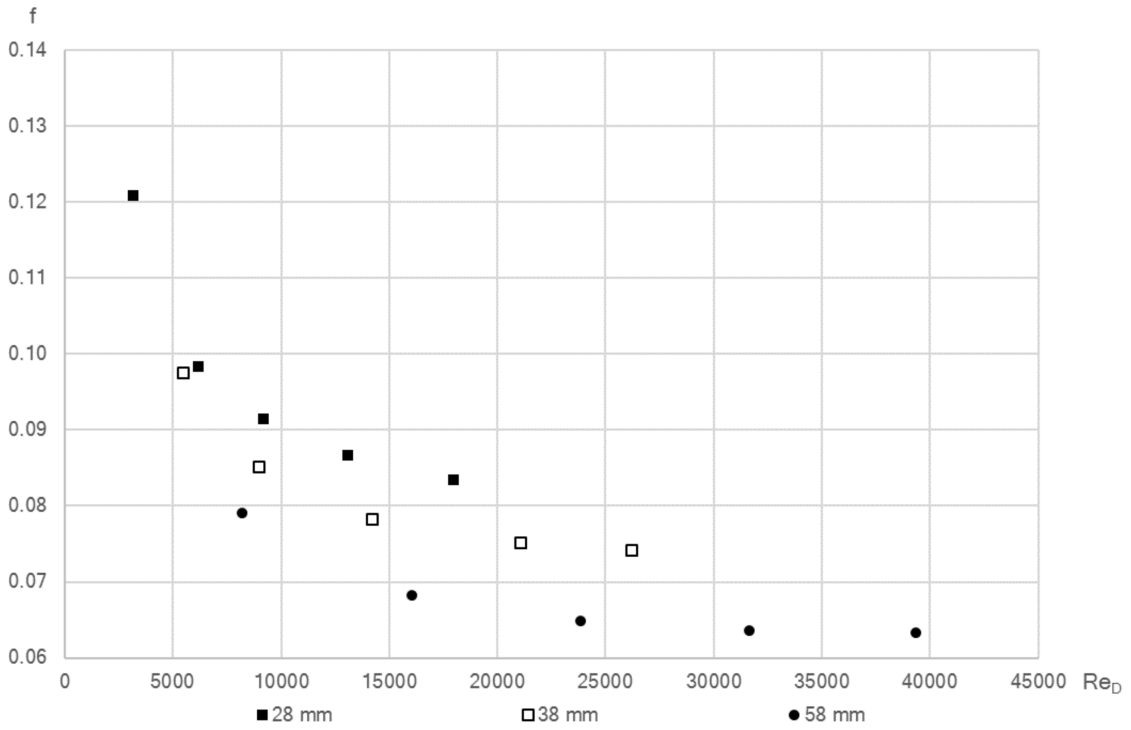

Figure 7.8. *Fanning friction factor as a function of the Reynolds number for varying tube diameters.*

7.5 The effect of the fin slit

If it is not feasible to make a single plate fin for the whole heat exchanger, the fin has to be cut from middle and afterwards welded to the tube. The width of the slit decreases wasted material slightly as the puncturing for tube consumes less material for wide slit. Slit width also directly influences the contact area for the fin which might affect the fin efficiency to a some degree. Wide fin slit also reduces the area between the tubes where heat transfer is expected to be less effective which might result in a higher conductance to mass ratio.

There seem to be a slight increase in the Colburn j-factor when increasing the slit width in Fig. 7.1. One cause might be a slight increase in the turbulence levels due to slits longitudinal edge is slightly closer to the channel flow between the tubes interacting it more. Another, a more likely cause, is that the increase in the slit width decreases the low heat transfer region between the tubes resulting in higher area averaged heat transfer coefficient. An interesting phenomenon occurs at highest Reynolds numbers where the smallest slit width actually results in a higher j-factor. This could be because only six tubes in height were simulated, and the first tube has the highest heat transfer. After averaging, the increase in heat transfer at first tube could counteract the increase in low heat transfer regions between the tubes. Another cause might be that the higher Reynolds numbers increases turbulent mixing which results in better mixing in the recirculation region. However, the effect is quite negligible and most likely within the modelling errors.

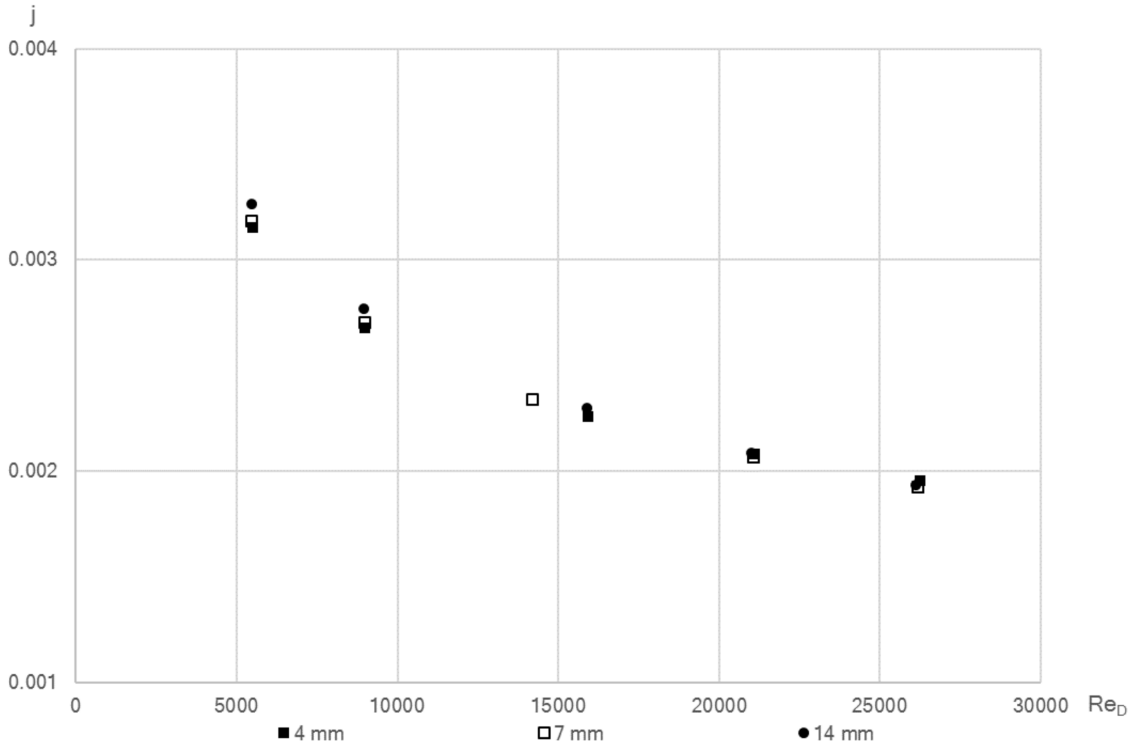

Figure 7.9. *Colburn j-factor as a function of the Reynolds number for varying fin slit widths.*

The variation of the Fanning friction factor with the variation in the fin slit width is given in Fig. 7.10. The higher slit width seems to increase the area averaged friction factor. This increase in the area averaged friction factor with increased slit width is most likely dominated by the decrease in low friction areas between the tubes. Again, similarly to the j-factor, the highest Reynolds numbers shows that the lowest slit width has higher friction factor than the medium slit width.

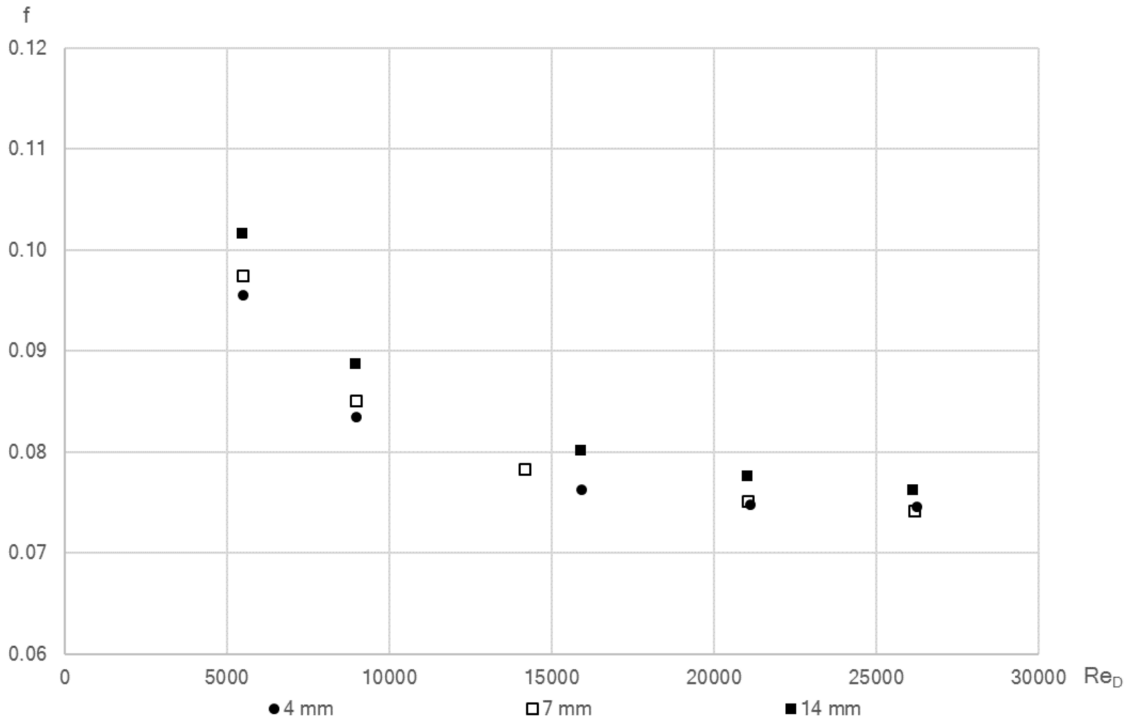

Figure 7.10. *Fanning friction factor as a function of the Reynolds number for varying fin slit widths.*

7.6 The effect of the gap between fins

The gap between fins is required because of the tolerances in manufacturing and assembly. As the gap decreases the total heat transfer area in the heat exchanger core it should be minimised if the maximum conductance per volume is a quantity of interest. There might be a minor turbulence promoting effect when the flow detaches from and attaches to the next fin when the gap is sufficiently high and as such it might increase surface performance slightly.

In this study the fins were perfectly aligned which is not the case in a typical heat exchanger core due to the manufacturing and assembly tolerances. The misalignment should lead into a higher form drag and increased turbulence due to sudden changes in the direction of the flow as it collides with slightly misaligned fins. Additionally, the boundary layer may be interrupted due to misalignment causing higher pressure drop and heat transfer.

The Fig. 7.11 shows that the gap between fins has almost no effect on the Colburn j-factor. The slight increase for higher gap widths is associated with the increased fin efficiency as the fin size is slightly decreased when the tube pitches are kept constant. In heat exchanger cores the misalignment is most likely to have a turbulence promoting and boundary layer interrupting effect thus increasing the j-factor but the phenomenon is not studied in this study.

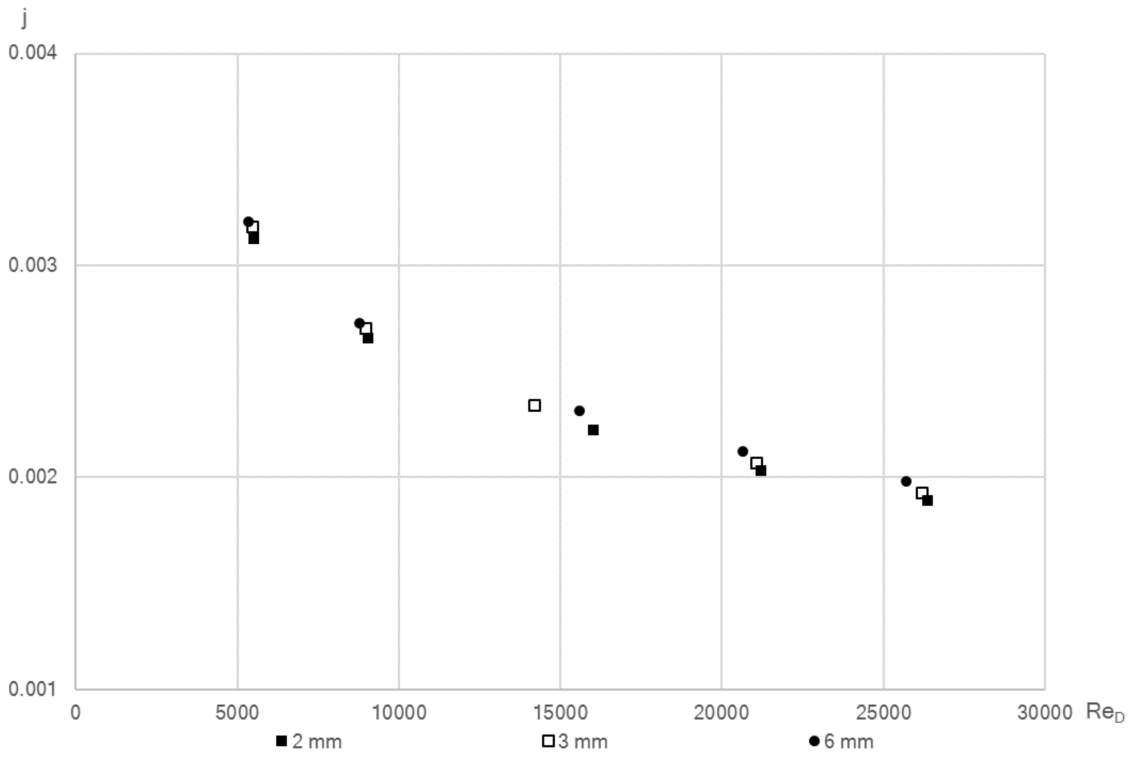

Figure 7.11. *Colburn j-factor as a function of the Reynolds number when varying the gap between the fins.*

The Fanning friction factor is also almost unaffected by the variation of the gap between the fins as shown in Fig. 7.12. Intuitively, the smallest fin gap should have the lowest friction factor as the surface area for which the friction factor is averaged is increased and this seems to be the case in the CFD solutions. The values are, however, too close together to make any conclusions of the effect of the fin gap.

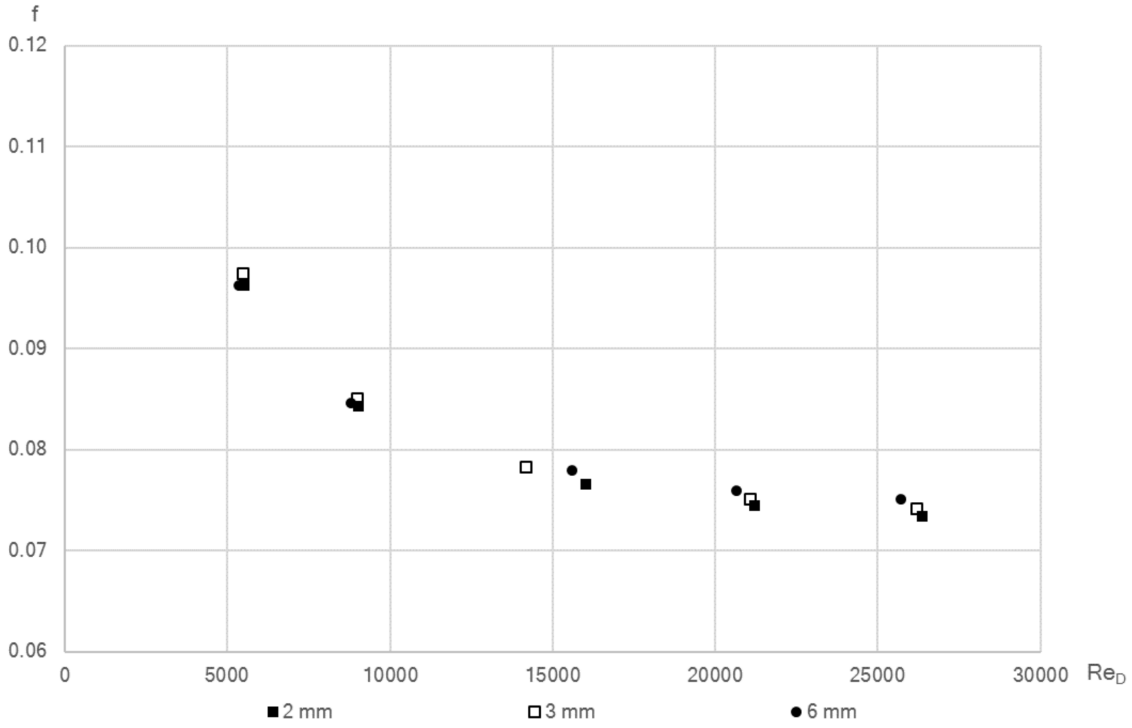

Figure 7.12. *Fanning friction factor as a function of the Reynolds number for varying fin slit widths.*

7.7 The effect of the fin thickness

The fin thickness is one of the most important parameter in the finned tube design from the thermal-hydraulic point of view. The fin thickness has a direct impact on the fin efficiency while otherwise it does not affect the finned tube design that much. There should be a slight increase in the form drag as the fin thickness is increased. The fin thickness usually has an optimum value for a given geometry but this optimum might differ depending the value to be optimised. For example, a mass optimum lead into a quite thin fin while a volume optimum lead into a somewhat thicker fin. In this study the channel between fins was kept constant to only study the effect of the fin thickness, in other words, the fin pitch was increased and decreased according to fin thickness. The different fin profiles were not studied in this study but usually a mass optimised fin profile has a thicker base than the tip as seen in the study by Singh et al. (2017b). This is a logical result as the heat rate at the fin base is higher than in the fin tip.

The effect of the fin thickness on the Colburn j-factor is shown in the Fig. 7.13. The higher fin thicknesses increases the j-factor as expected as the increase in the fin thickness increases the fin efficiency.

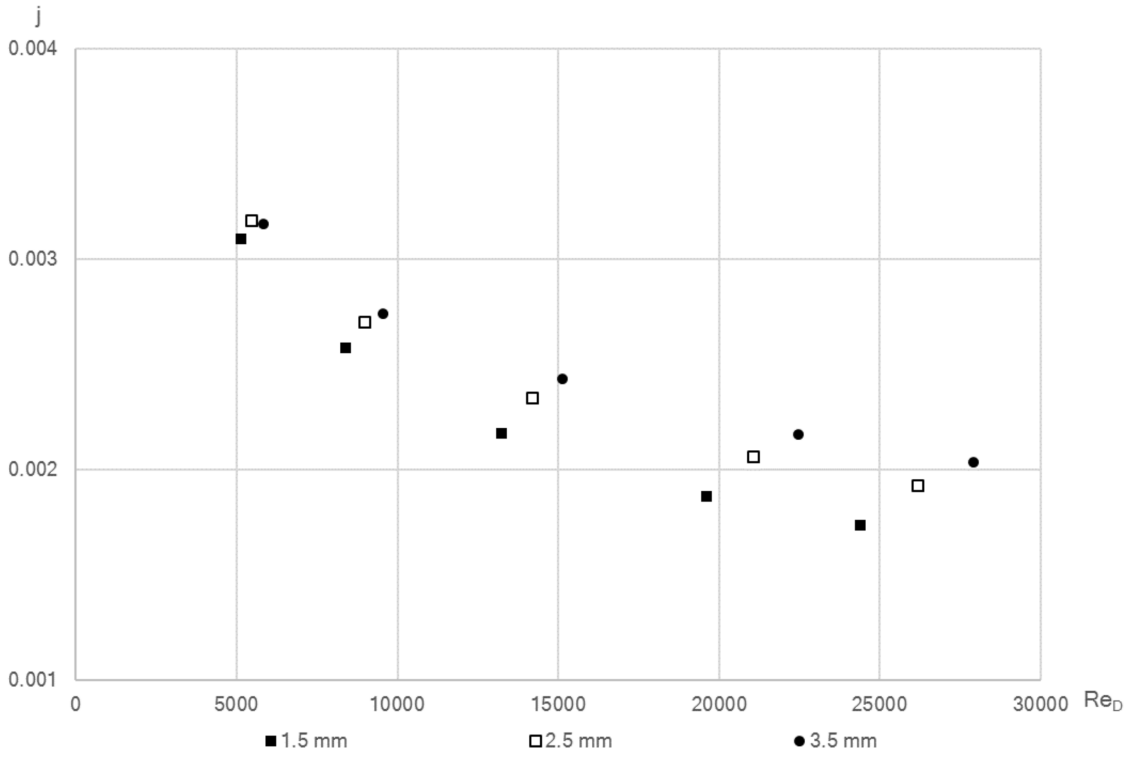

Figure 7.13. *Colburn j-factor as a function of the Reynolds number for varying fin thicknesses.*

The effect of the fin thickness on the Fanning friction factor is shown in the Fig. 7.14. There seems to be a surprisingly high increase in the friction factor for increasing the fin thickness which is most likely due to the increased form drag. This suggests that the form drag due to the fins have a quite high contribution to the total friction factor. It might be possible to decrease the form drag by sharpening the first fin leading edge to prevent the recirculation zone in the fin leading edge (see Fig. 6.13).

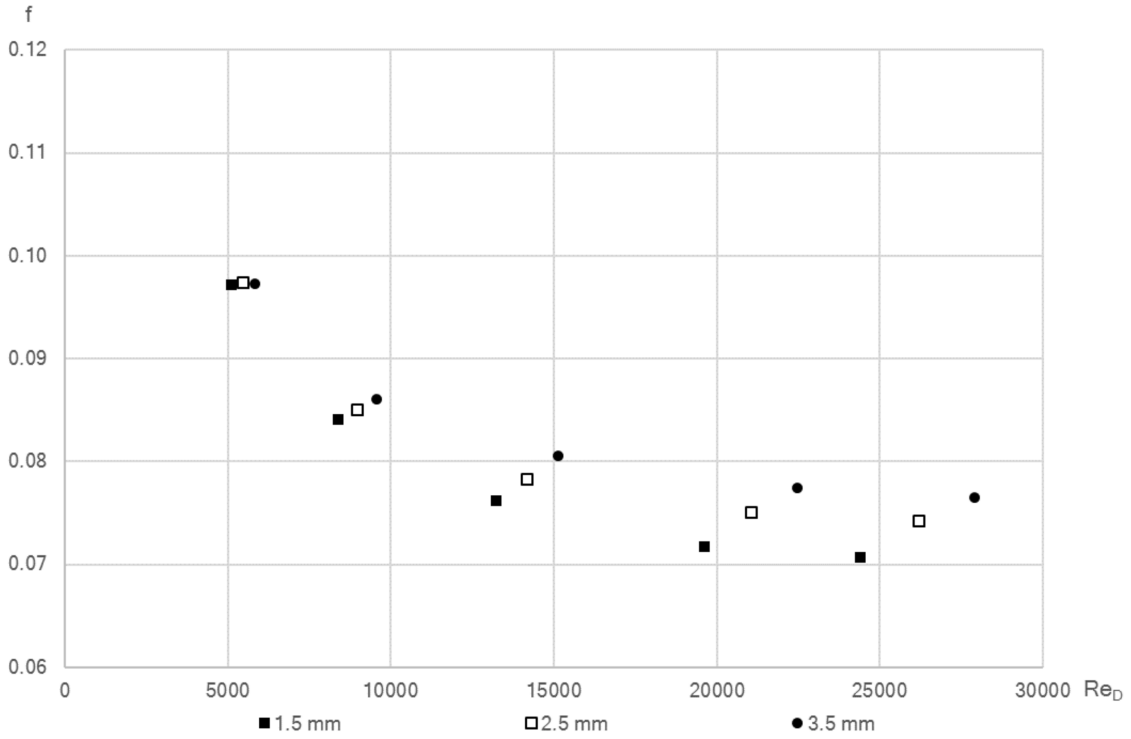

Figure 7.14. *Fanning friction factor as a function of the Reynolds number for varying fin thicknesses.*

8. COMPARISON OF DIFFERENT GEOMETRIES FOR FEASIBILITY

To compare the performance of the different geometries the correlations for Nusselt number, Euler number and fin efficiency for each case has to be developed. These correlations can then be used in calculating the finned tube performance for the given limiting boundary conditions. The limiting boundary conditions could be for example pressure drop and total heat transfer rate. Thus all comparing should be done for equal pressure drop and total heat transfer rate. Another limiting factor could be for example the pumping power and total heat transfer which would give slightly different optimal geometry. The pumping power is related to a pressure drop with the equation $\dot{W}_{pumping} = \dot{V}\Delta p$.

In this study the main comparison is done for the same pressure drop for given mass flow and inlet and outlet temperature as these are the dimensioning parameters for the exhaust gas boilers in diesel engine applications. This results in boilers with a different cross-sectional area and height but with same pressure drop and total heat transfer.

8.1 Geometries and correlations

The geometric parameters for all calculated cases are given in the appendix A. The tube diameter was varied from 38 to 58 mm, fin pitch from 10 to 30 mm, transverse pitch from 60 to 125, longitudinal pitch from 60 to 100, gap between fins from 2 to 6 mm, slit width from 4 to 14 mm and the fin thickness from 1.5 to 2.5 mm. Additionally, one case was calculated for a single gilled tube.

The correlations for fin efficiency, Euler number and Nusselt number are given in Table J.1. The correlations are developed for each case and as such they are slightly more accurate than the universal correlations given in the appendix I. However, this limits the comparison of different geometries to these specific cases.

As the optimisation of the heat exchanger is quite complex because there are multiple boundary conditions which have to be simultaneously satisfied and the each partial optimum might not be even close to global optimum. In this study only mass and volume optimum are considered as they can be unambiguously presented. It should be kept in mind that the fin and tubes usually have different prices and the manufacturing might be easier if there are less tubes. Additionally, the welding hours for a single tube bend in the heat exchanger core was approximated as 20

minutes for a single tube bend weld while the fins were assumed to be welded with a robot welding (Lotila and Aaltonen, 2017).

8.2 Dimensioning the heat exchanger

The dimensioning values for the boiler were chosen rather arbitrarily as typical values for exhaust gas boiler related to the diesel engine. The dimensioning values for the exhaust gas boiler are 15 $\frac{kg}{s}$, 623 K, 463 K, 443 K and 800 Pa for mass flow, inlet temperature, outlet temperature, tube inside temperature and pressure drop respectively. The temperature inside the tubes is in this case is constant which corresponds an evaporator section of the exhaust gas boiler. All temperature dependant properties are calculated with average temperature between the inlet and outlet according to the correlations given in the Appendix E.

For thermal-hydraulic dimensioning the equations (2.5) and (4.9) have to be solved simultaneously for heat output and pressure drop given with the input parameters in the earlier paragraph. The required geometric parameters for dimensioning are given in the Appendix K.

By using the appendices J and K, the tube length, tubes in width N_T and tubes in height N_L can be calculated. Tube length, tubes in width and tubes in height can then be used to calculate the total mass and required volume of the heat exchanger for given input values after which the different cases can be compared. The heat exchanger footprint was chosen as square for simplicity and it does not affect thermal-hydraulic dimensioning in any way. In the typical heat exchangers the square frontal area is preferred as the even flow distribution is usually easier to achieve.

The Table 8.1 shows the numbers of the tubes in the transverse and longitudinal directions and the dimensions of the heat exchanger core performing similarly for all cases. The number of tubes are not truncated to the nearest integer as it would cause unnecessary trimming for these specific input values. The higher tube pitches did not perform very well suggesting that the tube pitches much higher than 75 mm for 38 mm tube are not recommended.

Table 8.1. *Tubes in width N_T and height N_L and heat exchanger core dimensions for all cases.*

Case	N_T	N_L	Width (m)	Height (m)
1	22.5	36.2	1.7	2.7
2	23.0	25.0	1.7	1.9
3	22.4	42.6	1.7	3.2
4	22.4	53.9	1.7	4.0
5	15.8	49.9	1.6	3.7
6	31.4	25.4	1.9	1.9
7	22.6	31.1	1.7	3.1
8	22.6	41.4	1.7	2.5
9	22.3	40.7	1.7	3.1
10	22.9	33.5	1.7	2.5
11	20.7	45.9	1.6	3.4
12	27.3	25.4	2.1	1.9
13	22.4	35.4	1.7	2.7
14	22.7	37.3	1.7	2.8
15	22.6	35.7	1.7	2.7
16	22.4	38.6	1.7	2.9
17	22.6	37.6	1.7	2.8
18	16.2	57.3	1.6	5.7
19	16.1	46.3	1.6	4.6
20	12.9	73.2	1.6	7.3
21	23.9	112.5	1.8	8.4

The Fig. 8.1 shows the calculated mass, volume and welding hours for tube bends of different cases compared to the reference case 1. The cases from 18 to 21 are not presented in the next bar diagram 8.1 as they resulted in very high masses and volumes. The pressure drop and output for each geometry is same thus the difference in mass and volume corresponds to the thermal-hydraulic dimensioning of the heat exchanger with given heat transfer surface geometry and boundary conditions. The negative values means that the mass or volume of the case in question is lower than the reference case i.e. the heat exchanger is better in that aspect than the reference case 1 in regards of thermal-hydraulic dimensioning. The calculated mass, volume and welding hours for the reference case were 11 800 kg, 7.7 m^3 and 830 h respectively

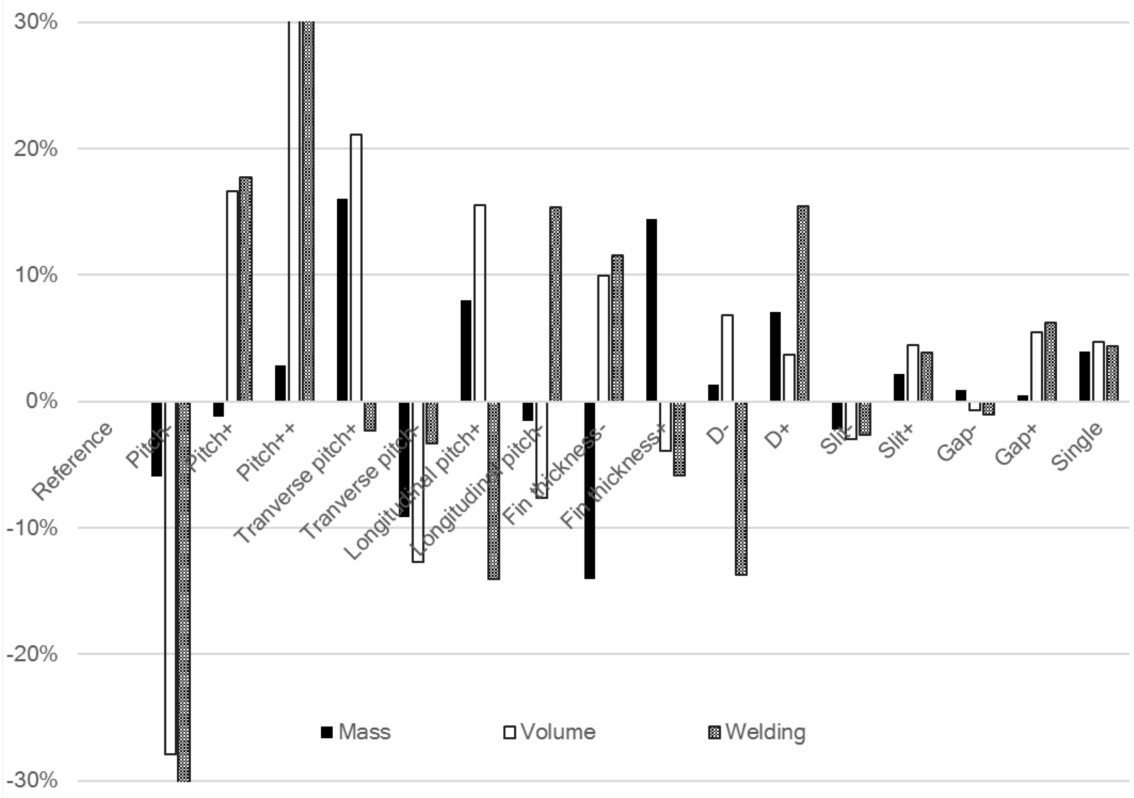

Figure 8.1. *Mass, volume and welding hours of different cases compared to the reference case 1.*

The fin pitch seems to be the only parameter which affects the thermal-hydraulic dimensioning considerably. Lower pitches are better in mass and volume efficiency while simultaneously providing a design with least welding work. The fin pitch is, however, many times limited by the exhaust gas fouling tendency and a clean exhaust gas is required for low fin pitches.

The increase in transverse pitch increases both mass and volume of the heat exchanger core which means that increasing the fin size is not an option if the heat transfer surface mass or volume is to be decreased. If the transverse pitch is decreased, either the aspect ratio of the boiler or tube amount in width has to be increased. Increasing the tube amount increases the tube bends required to connect the tubes which in turn requires more welding. If the tube length is increased the aspect ratio of the frontal area is increased which might make the flow distribution more challenging.

The increase in longitudinal pitch increases both mass and volume of the heat exchanger core. As the longitudinal pitch is increased the number of tubes in height is decreased while simultaneously the core is slightly longer due to a longer fin. The decreased tube number decreases the welding work for connecting the tubes but the increased flow length might decrease the soot blowing efficiency ending up in requiring more tube banks for a high output boilers. The increased longitudinal pitch also makes the exact dimensioning harder as the tube number in row has to be rounded

to at least to nearest two tubes due to double gilled tube geometry.

Decreasing the fin thickness should be done if the mass is to be minimised. This, however, leads into increased heat exchanger core volume and higher welding work. It should be noted that the flow area was kept constant with different fin thicknesses i.e. fin pitch was changed along the fin thickness. Some of the variation in mass and volume of the heat exchanger core might come from the reduced fin pitch. However, the effect of the fin thickness is much higher than what would be expected from varying the fin pitch by 1 mm.

Increasing and decreasing the tube diameter surprisingly increases both the mass and volume of the heat exchanger core. Smaller tube diameters also leads into smaller welding hours. Even though the tube wall thickness was not varied in this study, decreasing the wall thickness has an obvious effect of decreasing the mass of the heat exchanger while simultaneously increasing the fin efficiency slightly as the wall conductance is increased.

Decreasing the fin slit width increases both the mass, volume and welding hours of the heat exchanger core. The decrease in the volume of the heat exchanger is quite easy to explain as the heat surface density is increased by decreasing the slit size. However, the mass should intuitively increase as it increases the low performance heat surface between fins. This could, however, be due to fact that only six tubes in a row were calculated to make the correlations and it might overemphasise the first fin which has the highest heat transfer coefficient of all fins.

Increasing the gap between fins has an expected effect of increasing the volume of the heat exchanger as the heat surface density is decreased. The slight increase in mass for both directions suggests that the fin gap width is quite close to the mass optimum for reference geometry.

The single gilled tube performs about 5 % worse in both volume and mass. This is a rather high number considering the fact that only 0.5 % of the finned tube surface is removed between the two tubes. However, the heat transfer coefficient is 4 % lower for single gilled tube according to the CFD calculations.

It should also be noted that the optimisation of the mass and volume alone will not necessarily lead into an optimum design as the pipes are usually more expensive material while the fins are cheaper. The increased tube number also lead into increased welding length as the tubes have to be connected to transfer the medium inside to an another tube. The optimum design depends the ratio of the material costs to the total costs. If the material costs dominates the total costs, the design which leads into the material reduction usually also lead into reduction of the total costs. However, if the material costs and work costs are roughly half of the total costs, both have to be considered in the cost optimisation. Additionally, if only the total costs are considered, the resulting design may be of such sort that it does not even work as expected. This might be the case, for example, if the ratio of the inlet duct flow area to the heat exchanger core frontal area is too big resulting in a uneven flow distribution.

9. CONCLUSIONS

In this study, the effect of the H-type finned tube geometric parameters was studied with CFD. Correlations for the all studied geometries were developed to compare the dimensionless numbers. Additionally, a heat exchanger core was dimensioned with the correlations developed from the CFD to assess the effect of the parameters on the mass and volume of the heat exchanger core and the tube bend welding time. The varied parameters in this thesis were the fin pitch, transverse pitch, longitudinal pitch, fin thickness, tube diameter, fin slit and fin gap.

The geometric parameters in this study were varied one at the time and no comprehensive study of the additivity of the changes was made. The simultaneous variation in the geometric parameters might or might not be result into additive changes in the thermal-hydraulic performance as the flow field around the finned tube is relatively complex. As such, the additivity of the changes in the geometric parameters should be studied.

The flow field in the in-line H-type finned tube geometry contains many complex fluid dynamics phenomena including recirculation, boundary layer separation and even vortex shedding in some operation situations. The flow pattern across all cases did not vary much with varying geometries or Reynolds numbers. The flow quickly assumed a channel flow between the tubes and the interaction of the main channel flow to the recirculation area behind the tubes was quite negligible. The only noticeable secondary flow was the recirculation region between and after the tubes which resulted from the boundary layer separation at slightly over 90 degrees at tubes. The tube diameter affected the recirculation region the most, and the lowest tube diameter seemed to produce the simplest recirculation region while the higher tube diameters produced additional smaller recirculation regions to the back of the tube as the flow turned to the main flow. At the fin leading edge, there was a slight recirculation region due to a sudden contraction caused by the fins.

Maybe the most insightful feature of these kind of H-type in-line finned tubes was that the friction and heat transfer characteristics was dominated by the fin area in the channel between the tubes suggesting that the fin area in the recirculation region does not contribute that much to the overall performance of the fins. The local heat transfer coefficient at the fin surface seemed to be very similar in all cases and almost all variation in the overall heat transfer coefficient seemed to be caused by the non-isothermal fin. The local heat transfer coefficient at the channel between tubes was quite close to the Tiddus-Boelter correlation in each case while the heat flux at the recirculation region was approximately half of the channel and

even negative in some parts. Thus there might be a possibility that the problem of the conjugate heat transfer could be approximately simplified to the calculation of the fin temperature profile as the channel between the tubes dominates the fin efficiency and heat transfer. The same applies to the pressure drop as the friction factor is quite to one obtained from the Moody's chart in the channel between the tubes while the recirculation region could be approximated as almost zero friction area as the velocities are low. The form drag associated with the boundary layer separation at the tubes has still be accounted in some way though as the skin friction is only a small fraction of the total pressure drop with the finned tubes.

To fairly compare the different geometries from the heat exchanger dimensioning point of view, all cases were dimensioned as equal heat transfer and pressure drop heat exchanger cores. The fin pitch had the most effect on the thermal-hydraulic characteristics of the finned tubes. Low pitches always produce the lowest mass, volume and tube bend welding time for the heat exchanger core. Increasing the transverse pitch seemed to produce heat exchanger cores with higher mass and volume while the welding time decreased slightly for both decreasing and increasing the transverse pitch. The increase in the longitudinal pitch led into higher mass and volume of the heat exchanger and lower welding time while the opposite is true for decreasing the longitudinal pitch. Increasing the fin thickness resulted in heat exchanger core with higher mass but lower volume and welding time while the opposite is true for lowering the fin thickness. Changing the tube diameter seemed to increase the mass and volume of the heat exchanger while the welding time decreased when decreasing the tube diameter. The increase in fin slit width increases mass, volume and welding time. Increasing the gap between fins led into increase in the mass, volume and welding time. Single gilled fin also resulted in heat exchanger with more mass, volume and welding time.

As suggestions for future studies, the alternative fin shapes, the effect of the number of the tube rows and fin enhancement methods should be studied as it is quite obvious that there is no single geometric parameter which dominates the others. Minimising the fin pitch would otherwise result savings in every area but the fouling of the heat surfaces might be a problem in many applications with low fin pitches. The enhancement methods in the exhaust gas boiler applications should preferably be of such sort that they do not negatively impact soot blowing.

BIBLIOGRAPHY

Ansys Inc. *ANSYS 16.2 User Manual, Fluent*, 2016.

Blasius, H. 1908. The boundary layers in fluids with little friction. *National Advisory Committee for Aeronautics, Technical Memorandum 1256*, 126. `http://naca.central.cranfield.ac.uk/reports/1950/naca-tm-1256.pdf`, accessed 4.9.2017.

Cengel, Y.A. 2008. *Introduction to Thermodynamics and Heat Transfer*. McGraw-Hill, second edition.

Cengel, Y.A. and Cimbala, J.M. 2013. *Fluid Mechanics Fundamentals and Applications*. McGraw-Hill, third edition.

Chen, H. et al. 2015. Experimental study on heat transfer and resistance characteristics of h-type finned tube. *2015 AASRI International Conference on Industrial Electronics and Applications*. [`http://www.atlantis-press.com/php/download_paper.php?id=20525`, accessed 2.3.2017].

Erek, A., Özerdem, B., Bilir, L., and Ilken, Z. 2004. Effect of geometrical parameters on heat transfer and pressure drop characteristics of plate fin and tube heat exchangers. *Applied Thermal Engineering*, 25:2421–2431.

Gauler, K. 1974. *Wärme- und Stoffübertragung an eine mitbewegte ebene Grenzfläche bei Grenzschichtströmung*. Max-Planck-Institut für Strömungsforschung Göttingen: Mitteilungen aus dem Max-Planck-Institut für Strömungsforschung. Dt. Forschungs- u. Versuchsanst. f. Luft- u. Raumfahrt, Forschungszentrum Aerodynam. Versuchsanst., Max-Planck-Ges. z. Förderung d. Wiss., Max-Planck-Inst. f. Strömungsforschung.

Gnielinski, V. 1976. New equations for heat and mass transfer in turbulent pipe and channel flow. *Int. Chem. Eng*, 16:359–368.

Incropera, F., Bergman, T., Lavine, A., and Dewitt, D. 2011. *Fundamentals of Heat and Mass Transfer*. John Wiley & Sons, seventh edition.

Jang, J., Wu, M., and Chang, W. 1996. Numerical and experimental studies of three-dimensional plate-fin and tube heat exchangers. *International Journal of Heat and Mass Transfer*, 39:3057–3066.

Jin, Y. et al. 2013. Parametric study and field synergy principle analysis of h-type finned tube bank with 10 rows. *International Journal of Heat and Mass Transfer*, 60:241–251. [`http://www.sciencedirect.com/science/article/pii/S0017931012009064`, accessed 1.8.2017].

Joardar, A. and Jacobi, A. 2008. Heat transfer enhancement by winglet-type vortex generator arrays in compact plain-fin-and-tube heat exchangers. *International Journal of Refrigeration*, 31:87–97.

Kays, W.M. and London, A.L. 1964. *Compact Heat Exchangers.* McGraw-Hill, second edition.

Leu, J., Wu, Y., and Jang, J. 2004. Heat transfer and fluid flow analysis in plate-fin and tube heat exchangers with a pair of block shape vortex generators. *International Journal of Heat and Mass Transfer*, 47:4327–4338.

Lotila, H. and Aaltonen, P. 2017. Welding time for a single tube bend. Private conversation.

Patankar, S. 1980. *Numerical Heat Transfer and Fluid Flow.* McGraw-Hill, first edition.

Peric, F. 2002. *Computational Methods for Fluid Dynamics.* Springer-Verlag, third edition.

Pohlhausen, E. 1921. Der wärmeaustausch zwischen festen körpern und flüssigkeiten mit kleiner reibung und kleiner wärmeleitung. *ZAMM - Journal of Applied Mathematics and Mechanics / Zeitschrift für Angewandte Mathematik und Mechanik*, 1(2):115–121. ISSN 1521-4001. doi:10.1002/zamm.19210010205.

Pope, S.P. 2009. *Turbulent Flows.* McGraw-Hill, seventh edition.

Schlichting, H. and Kestin, J. 1979. *Boundary-layer theory.* New York : McGraw-Hill, 7th ed edition. ISBN 0070553343. Translation of Grenzschicht-Theorie.

Schmidt, T. 1949. Heat transfer calculations for extended surfaces. *Refriferating Engineering*, 4:351–357.

Shah, R.K. 1978. Compact heat exchanger surface selection methods. *Heat Transfer*, 4:193–199.

Shah, R.K. and Sekulic, D.P. 2003. *Fundamentals of Heat Exchanger Design.* John Wiley & Sons, first edition.

Singh, S., Sørensen, K., and Condra, T. 2017a. Investigation of material efficient fin patterns for cost-effective operation of fin and tube heat exchanger. *Applied Thermal Engineering*, 126:903–914.

Singh, S., Sørensen, K., Simonsen, A.S., and Condra, T. 2017b. Implications of fin profiles on overall performance and weight reduction of a fin and tube heat exchanger. *Applied Thermal Engineering*, 115:962–976.

Thulukkanam, K. 2013. *Heat Exchanger Design Handbook.* CRC Press, second edition.

VDI e. V. 2010. *VDI Heat Atlas.* Springer Berlin Heidelberg, second edition.

Versteeg, H. and Malalasekera, W. 2007. *An Introduction to Computational Fluid Dynamics.* Pearson Education Limited, second edition.

Wang, C. and Chi, K. 2017. Heat transfer and friction characteristics of plain fin-and-tube heat exchangers, part i: new experimental data. *International Journal of Heat and Mass Transfer*, 43(15):2681–2691.

Wang, H., Liu, Y., Yang, P., Wu, R., and He, Y. 2016. Parametric study and optimization of h-type finned tube heat exchangers using taguchi method. *Applied Thermal Engineering*, 103:128–138.

Webb, R. 2005. *Principles of Enhanced Heat Transfer*. Taylor & Francis. ISBN 9781591690146.

White, F. 2009. *Fluid Mechanics*. McGraw-Hill, seventh edition.

Zhong, G.Y., Liu, Q.S., and Liu, Y.W. 2017. Modeling of thermal-hydraulic characteristics of h-type finned tube using response surface methodology. *Energy Procedia*, 105:5098–5105.

Appendices

A. GEOMETRIC PARAMETERS FOR ALL CALCULATED CASES

The geometric parameters for all calculated cases are shown in the Table A.1. The explanation of the notation is given in the Table 5.1. In the layout column, the double means a double gilled tube, single a single gilled tube and bare a tube bank heat exchanger

Table A.1. *Geometric parameters of all calculated cases in millimetres.*

Case	*Layout*	D	P	S_T	S_L	δ_f	Δ_f	s_f	s_{tube}
1	Double	38	15	75	75	3	7	2.5	4
2	Double	38	10	75	75	3	7	2.5	4
3	Double	38	20	75	75	3	7	2.5	4
4	Double	38	30	75	75	3	7	2.5	4
5	Double	38	15	100	75	3	7	2.5	4
6	Double	38	15	60	75	3	7	2.5	4
7	Double	38	15	75	100	3	7	2.5	4
8	Double	38	15	75	60	3	7	2.5	4
9	Double	38	14	75	75	3	7	1.5	4
10	Double	38	16	75	75	3	7	3.5	4
11	Double	28	15	75	75	3	7	2.5	4
12	Double	52	15	75	75	3	7	2.5	4
13	Double	38	15	75	75	3	4	2.5	4
14	Double	38	15	75	75	3	14	2.5	4
15	Double	38	15	75	75	2	7	2.5	4
16	Double	38	15	75	75	6	7	2.5	4
17	Single	38	15	75	75	3	7	2.5	4
18	Double	38	15	100	100	6	14	1.5	4
19	Double	38	15	100	100	6	14	2.5	4
20	Double	38	15	125	100	3	7	1.5	4
21	Bare tube	38	-	75	75	-	-	-	4

B. UNDER-RELAXATION FACTORS AND INITIALISATION OF THE COUPLED SOLVER

The under-relaxation factor for energy was chosen as 0.99 for first 200 iterations to get faster convergence. After that, the under-relaxation factor for energy was decreased to 0.75-0.90 depending on the inlet velocity to prevent oscillations in solutions. Time scale for pseudo-transient formulation was calculated with ANSYS Fluent "automatic" formulation while the fluid timescale factor was chosen as 2 and solid timescale factor as 5 to speedup convergence. These parameters were chosen by trying different parameters and they may not be the best, however, these resulted in much faster and more robust convergence than the default SIMPLE algorithm. The used under-relaxation factors are given in Table B.1.

Table B.1. *Under-relaxation factors.*

Pressure	0.5
Momentum	0.5
Density	1
Body Forces	1
Turbulence kinetic energy	0.75
Specific dissipation rate	0.75
Turbulent viscosity	0.75
Energy	0.75 - 0.99

The first solution in each case which was the case with the highest velocity was initialised by using a standard initialisation from inlet values for initial guess. After that full multi-grid (FMG) initialisation was used to get good initial guess for the solver. The FMG initialisation solves the inviscid Euler equations for fluid domain which gives a rather good guess for initial flow field. The FMG was found to be best initialisation method in this case for overall speed of convergence as it did not take that much longer than hybrid initialisation while simultaneously providing much faster convergence.

After first solution of each case the solutions at lower velocities were calculated directly from next higher velocity solution which resulted into even faster convergence. As boundary layers are known to cause stiffness to the discretised equations, the speedup from using high velocity solution for low velocity solution initial values might be due to the fact that high velocity solution has almost correctly resolved boundary layers for lower velocity solution.

C. TEMPERATURE PROFILES BETWEEN THE FINS AT DIFFERENT POSITIONS

Figure C.1 shows the temperature profiles at the each tube, a $\frac{3}{8}$ transverse pitch away from the tube symmetry. The temperature profiles follow similar trend as the velocity profiles as expected. The highest heat resistance which is directly proportional to the temperature gradient occurs near the wall while the core region has a much lower heat resistance.

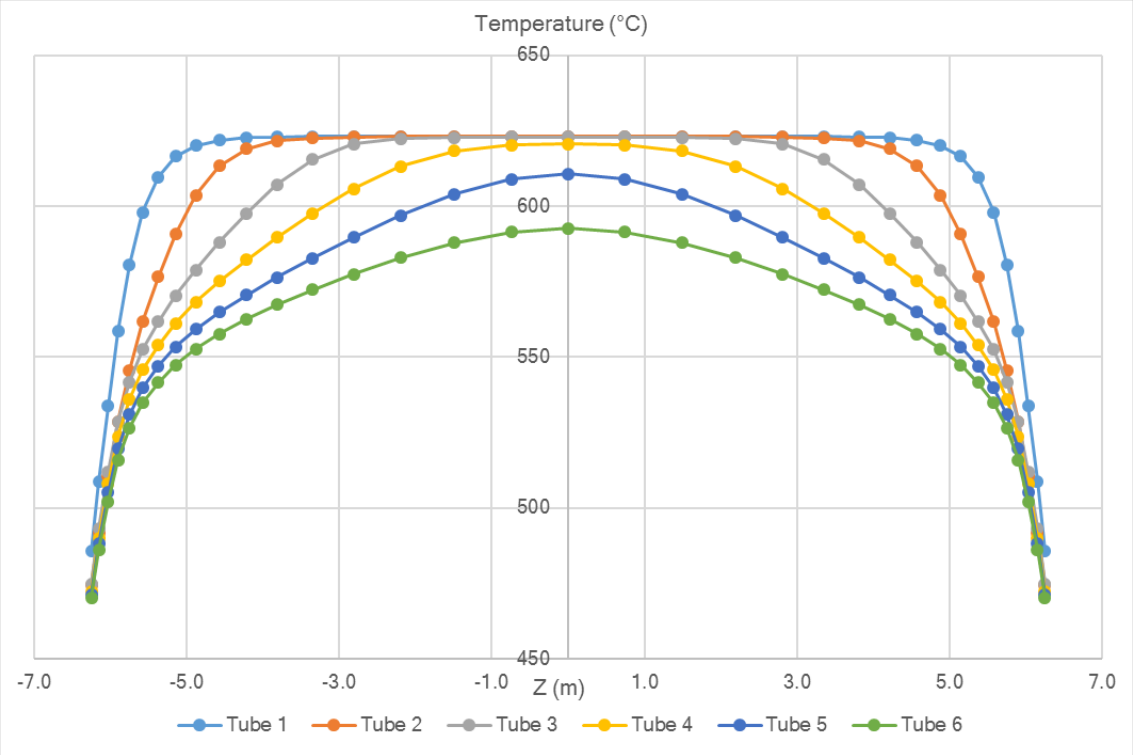

Figure C.1. *Temperature profiles at $\frac{3}{8}$ transverse pitch away from tube symmetry line at each tube.*

Figure shows the dimensionless temperature profiles at two last tubes $\frac{3}{8}$ transverse pitch away from tube symmetry. The normalisation is done with fin pitch for z direction and $\frac{T-T_{fin}}{T_{centre}-T_{fin}}$ is used for temperature normalisation. The temperature profile is still developing at the last tubes which is easier to confirm from dimensionless temperature profile as the temperature decrease due to the heat transfer is eliminated in normalisation.

C. Temperature profiles between the fins at different positions

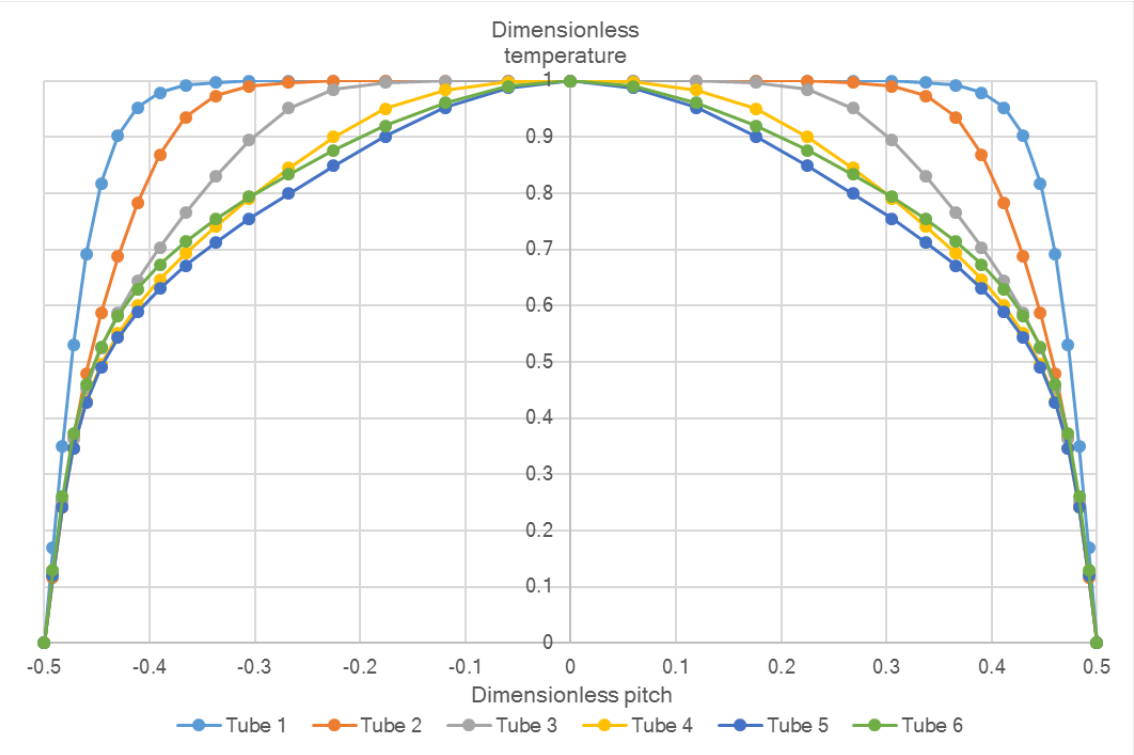

Figure C.2. *Dimensionless temperature profiles at* $\frac{3}{8}$ *transverse pitch away from tube symmetry line at each tube.*

D. THE BOUNDARY LAYER DEVELOPMENT BETWEEN THE FINS

The development of the momentum and thermal boundary layers is shown in Fig. D.1 in addition to correlations for laminar flat plate boundary layer by Blasius (3.7) and turbulent flat plate boundary layer for $\frac{1}{7}$ power law (3.10). For two first tubes the momentum boundary layer develops as laminar flat plate boundary layer. At third tube there is a sudden increase in boundary layer thickness which might be associated the flow transition from laminar to turbulent. This corresponds to Reynolds number of $Re_x = 72000$ which is almost an order of magnitude lower than 500 000 given in literature (Incropera et al., 2011, p. 390). It should, however, be noted that CFD has a hard time in capturing transitional flow unless transition specific turbulence models are used. At fifth tube the boundary layers occupy the whole gap between fins and after a while the flow may become fully-developed channel flow. This did not however occur in this CFD calculation. The thermal boundary layer is thicker than the momentum boundary layer as it should be according to Prandt number of 0.7 and turbulent diffusion at further in channel.

D. The boundary layer development between the fins

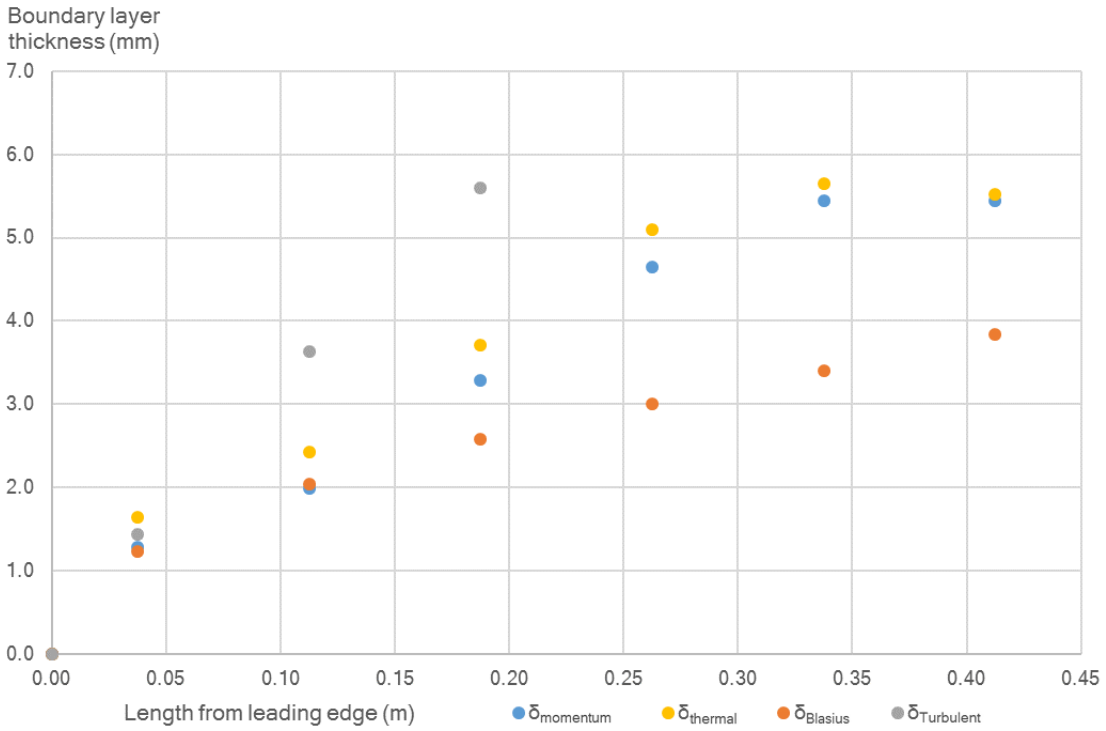

Figure D.1. *Boundary layer thicknesses at $\frac{3}{8}$ transverse pitches from tube symmetry from CFD and correlations.*

E. PROPERTIES FOR AIR

The correlations were developed by using the air properties given in VDI e. V. (2010) and their maximum error was less than 0.4 % for given values between 250 K and 1300 K. The correlation for all properties is of a form (E.1) where ϕ is a corresponding property and T is temperature given in Kelvin scale. The Table E.1 gives the coefficients for the equation.

$$\phi = \sum_{i=0}^{6} C_i T^i \tag{E.1}$$

Table E.1. *Correlations for air properties*

Variable	$\rho\left(\frac{kg}{m^3}\right)$	$c_p\left(\frac{J}{kgK}\right)$	$k\left(\frac{W}{m\times K}\right)$	$\mu\left(\frac{kg}{m\times s}\right)$
C_0	4.43564	1.01749×10^{3}	1.02129×10^{-2}	-1.41918×10^{-6}
C_1	-2.27381×10^{-2}	3.86869×10^{-2}	-8.31047×10^{-6}	9.18613×10^{-8}
C_2	6.10213×10^{-5}	-1.02802×10^{-3}	3.81547×10^{-7}	-1.17966×10^{-10}
C_3	-9.29978×10^{-8}	3.82542×10^{-6}	-7.88124×10^{-10}	1.34966×10^{-13}
C_4	8.08735×10^{-11}	-4.88584×10^{-9}	7.76095×10^{-13}	-9.38633×10^{-17}
C_5	-3.73356×10^{-14}	2.76588×10^{-12}	-3.80344×10^{-16}	3.30335×10^{-20}
C_6	7.09040×10^{-18}	-5.92724×10^{-16}	7.55881×10^{-20}	-4.16870×10^{-24}

F. CFD INPUT AND OUTPUT VALUES

The input and output values for CFD calculations are given in the next table. All calculations used same inlet temperature $T_i = 623K$, turbulence intensity $I = 1\%$ and eddy viscosity ratio $\frac{\mu_t}{\mu} = 2$. The tube temperature at inside the tube $T_w = 443K$ was also same in all cases. Only varied parameter was the domain inlet velocity V_∞. Output values were extracted with ANSYS CFD Post from the ANSYS Fluent solution. The values needed in data reduction were the total heat transfer rate Q, fin efficiency η_f, surface efficiency η_0 and pressure drop Δp of the fin system and the outlet temperature from the domain T_o. As the wall conductance was lumped into the surface efficiency the surface efficiency of the bare tube was assumed to be 99 % according to the finned tube cases. All unique inputs and outputs are given in Table F.1

Table F.1. *CFD input and output values*

Case	$V_\infty \left(\frac{m}{s}\right)$	Q (W)	Δp (Pa)	$T_o(K)$	η_f	η_0
1	3	38.423	19.905	545.435	0.8393	0.8622
1	5	56.189	50.201	555.083	0.7991	0.8250
1	8	79.767	121.813	562.928	0.7408	0.7776
1	12	107.533	268.373	569.327	0.6732	0.7194
1	15	126.489	418.123	572.798	0.6316	0.6837
2	2.5	30.567	25.280	511.574	0.8193	0.8356
2	4	43.084	56.442	525.017	0.7817	0.8013
2	7	64.494	153.610	539.480	0.7199	0.7452
2	11	89.056	357.884	550.096	0.6471	0.6788
2	14	104.782	565.661	556.051	0.6037	0.6392
3	3	42.821	15.395	558.268	0.8535	0.8812
3	5	63.240	39.887	565.736	0.8167	0.8512
3	8	91.540	99.657	571.336	0.7600	0.8050
3	12	126.267	224.594	575.740	0.6927	0.7500
3	16	157.768	400.267	579.061	0.6373	0.7048
4	3	51.894	11.966	570.773	0.8644	0.9007
4	6	89.386	45.473	578.119	0.8115	0.8615
4	9	123.424	100.929	581.804	0.7524	0.8180
4	13	163.907	208.075	585.340	0.6873	0.7700
4	17	199.886	351.692	588.163	0.6403	0.7351

F. CFD input and output values

Case	$V_\infty \left(\frac{m}{s}\right)$	Q (W)	Δp (Pa)	$T_o(K)$	η_f	η_0
5	3	45.150	11.871	554.696	0.7579	0.7835
5	5	63.540	29.182	565.445	0.7043	0.7356
5	8	86.564	69.274	574.112	0.6359	0.6743
5	12	112.421	150.202	580.856	0.5579	0.6045
5	16	133.687	260.224	585.644	0.5046	0.5566
6	2.5	31.372	29.311	527.874	0.8853	0.9060
6	4	45.696	69.955	536.546	0.8592	0.8844
6	7	71.655	205.226	545.852	0.8092	0.8431
6	11	103.203	501.835	552.887	0.7506	0.7945
6	15	133.761	936.320	557.182	0.6997	0.7523
7	3	45.751	24.103	530.523	0.7585	0.7843
7	5	65.876	60.604	543.272	0.7034	0.7351
7	8	91.221	145.666	554.222	0.6376	0.6761
7	12	119.905	317.818	563.147	0.5672	0.6130
7	15	139.018	491.768	567.856	0.5254	0.5756
8	3	32.968	17.435	556.545	0.8716	0.8946
8	5	48.492	43.913	564.451	0.8408	0.8693
8	8	70.203	107.329	570.174	0.7921	0.8292
8	12	96.543	238.463	574.837	0.7313	0.7790
8	15	114.891	373.372	577.410	0.6917	0.7464
9	3	34.467	17.270	548.495	0.7768	0.8099
9	5	49.500	43.322	558.919	0.7289	0.7690
9	8	68.557	104.108	567.699	0.6728	0.7209
9	12	90.429	226.400	574.642	0.6126	0.6694
9	15	105.730	351.994	578.028	0.5702	0.6331
10	3	41.613	22.725	544.263	0.8703	0.8883
10	5	61.767	57.804	553.008	0.8312	0.8544
10	8	89.661	141.875	559.701	0.7713	0.8028
10	12	122.129	312.978	565.877	0.7103	0.7501
10	15	144.575	486.886	569.253	0.6718	0.7167
11	3	36.512	11.913	549.331	0.7781	0.8006
11	6	58.325	40.707	564.310	0.7055	0.7352
11	9	76.737	87.205	571.653	0.6388	0.6752
11	13	96.922	176.116	578.308	0.5719	0.6148
11	18	118.048	330.550	584.015	0.5111	0.5600
12	2	30.603	26.955	530.202	0.9132	0.9322
12	4	54.391	98.015	540.765	0.8824	0.9078
12	6	76.334	214.396	546.311	0.8534	0.8848
12	8	97.389	377.746	549.948	0.8235	0.8612
12	10	118.360	590.874	552.377	0.7949	0.8386
13	3	38.756	19.884	544.765	0.8444	0.8659
13	5	56.649	50.187	554.528	0.8062	0.8328
13	9	88.496	153.626	563.819	0.7307	0.7676
13	12	110.021	271.107	568.066	0.6834	0.7267
13	15	130.414	425.169	571.216	0.6446	0.6930

F. CFD input and output values

Case	$V_\infty \left(\frac{m}{s}\right)$	Q (W)	Δp (Pa)	$T_o(K)$	η_f	η_0
14	3	37.784	19.882	546.757	0.8252	0.8523
14	5	55.101	50.162	556.413	0.7812	0.8149
14	9	84.843	152.387	566.292	0.7007	0.7467
14	12	104.145	266.374	571.039	0.6507	0.7043
14	15	121.973	413.316	574.618	0.6077	0.6678
15	3	38.716	20.366	544.862	0.8364	0.8593
15	5	56.602	51.440	554.587	0.7959	0.8243
15	9	87.862	156.819	564.258	0.7192	0.7582
15	12	108.546	275.034	568.825	0.6706	0.7162
15	15	127.674	428.064	572.336	0.6298	0.6810
16	3	36.176	17.947	550.028	0.8527	0.8751
16	5	52.876	45.570	559.119	0.8152	0.8433
16	9	82.769	140.496	567.673	0.7390	0.7785
16	12	102.398	246.805	571.890	0.6920	0.7386
16	15	120.644	384.615	575.105	0.6520	0.7045
17	3	37.135	18.797	548.045	0.8791	0.8974
17	5	54.413	48.176	557.164	0.8344	0.8595
17	9	84.488	150.217	566.258	0.7564	0.7932
17	12	103.699	263.729	570.799	0.7119	0.7554
17	15	121.513	409.346	574.083	0.6744	0.7235
18	4	52.740	18.673	563.245	0.5651	0.6078
18	6	66.516	38.734	572.847	0.5079	0.5561
18	9	82.878	81.492	581.460	0.4478	0.5018
18	14	104.748	187.635	589.475	0.3748	0.4358
18	19	122.628	338.700	594.385	0.3230	0.3888
19	4	60.999	22.672	553.822	0.6529	0.6842
19	6	78.355	47.105	563.870	0.5965	0.6329
19	9	100.026	100.349	572.827	0.5266	0.5691
19	14	128.106	232.347	581.982	0.4458	0.4955
19	19	150.702	418.016	587.827	0.3910	0.4454
20	4	57.055	13.961	571.430	0.4975	0.5315
20	8	80.189	50.868	586.802	0.3916	0.4351
20	12	96.949	106.368	593.951	0.3302	0.3792
20	17	114.104	207.951	599.064	0.2738	0.3268
20	23	131.038	361.104	602.986	0.2302	0.2858
21	3	1750.700	6.930	596.650	1.0000	0.9900
21	6	2957.400	27.522	600.790	1.0000	0.9900
21	9	4020.000	61.303	602.930	1.0000	0.9900
21	13	5321.800	126.330	604.740	1.0000	0.9900
21	16	6241.100	189.560	605.720	1.0000	0.9900

G. DISCRETISATION

A simple 2D computational mesh is presented in a Fig. G.1 for which the discretisation is conducted. The Fig. G.1 shows a typical structure of a simple computational mesh where indices (i, j) represent the location of the computational node in the mesh. As an example a simple 2D heat equation for solids (G.1) is given but the method is applicable to any governing equation. (Versteeg and Malalasekera, 2007, Chapter 4.2)

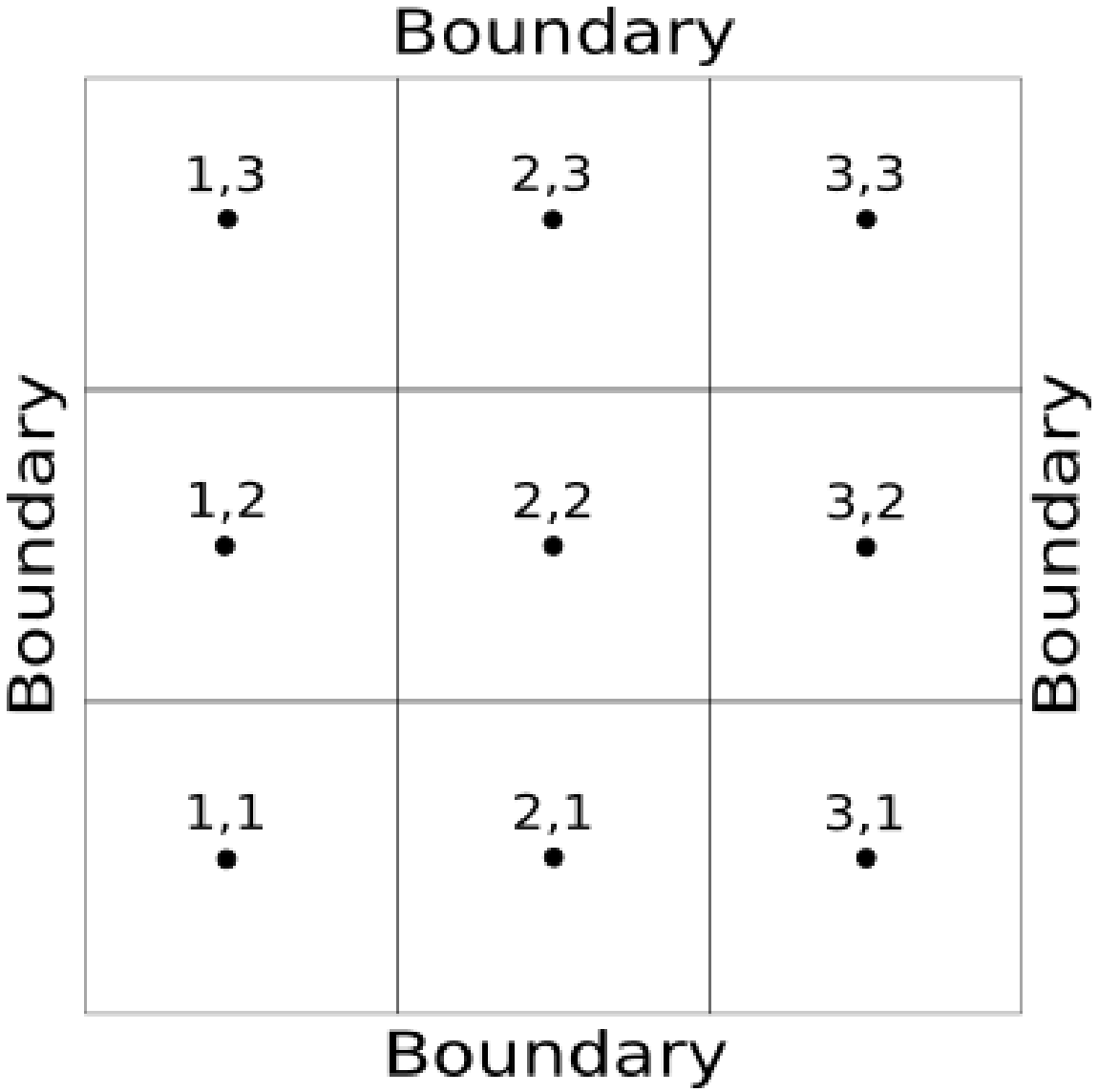

Figure G.1. *A sketch of a simple finite volume discretisation of a square.*

$$\iiint_R \rho c_p \frac{\partial T}{\partial t} dR + \oint_S (q_x dy + q_y dx) = 0 \tag{G.1}$$

As the q in solids is given by the Fourier's equation, the equation (G.1) may be presented in an alternative form (G.2).

$$\iiint_R \rho c_p \frac{\partial T}{\partial t} dR = \oint_S \left(k \frac{\partial T}{\partial x} dy + k \frac{\partial T}{\partial y} dx \right) \tag{G.2}$$

To solve the equation with discrete variables in cell nodes the integrals has to be approximated with discretisation. The approximation in this example is done at control volume (2, 2) to avoid boundary effects.

The time dependant term on the left hand side can be readily approximated with a forward time difference with the equation (G.3) if the mean value of the control volume is assumed to be node value. (Patankar, 1980, Chapter 4)

$$\iiint_R \rho c_p \frac{\partial T}{\partial t} dR \approx \rho c_p \frac{T_{i,j}^{n+1} - T_{i,j}^{n}}{\Delta t} \Delta x \Delta y \tag{G.3}$$

In the equation (G.3) the n presents the time number while Δt presents the time step size. As the time gradient has been fixed to a forward differencing discretisation the right hand side term decides whether the differencing scheme is implicit or explicit. By evaluating net heat flow at current time step the scheme becomes fully explicit and by evaluating net heat flow at next time step the scheme becomes fully implicit. (Patankar, 1980, Chapter 4)

The right hand side requires evaluating the fluxes at the faces which results in the equation (G.4). At this stage only the shape of the control volume is assumed to be rectangular. (Patankar, 1980, Chapter 4)

$$\begin{aligned} \oint_S \left(k \frac{\partial T}{\partial x} dy + k \frac{\partial T}{\partial y} dx \right) \approx & \; k \frac{\partial T}{\partial x} \Delta y \Big|_{i+\frac{1}{2},j} - k \frac{\partial T}{\partial x} \Delta y \Big|_{i-\frac{1}{2},j} \\ & + k \frac{\partial T}{\partial y} \Delta x \Big|_{i,j+\frac{1}{2}} - k \frac{\partial T}{\partial y} \Delta x \Big|_{i,j-\frac{1}{2}} \end{aligned} \tag{G.4}$$

In the equation (G.4) the indice $\frac{1}{2}$ means half step between computational nodes i.e. values at cell faces. As the equation requires evaluation of gradients at the cell faces they have to be approximated in some way. For example central differencing scheme uses values at adjacent nodes at current time step to approximate the gradients. This results in the equation (G.5). (Patankar, 1980, Chapter 4)

$$\oint_S \left(k\frac{\partial T}{\partial x}dy + k\frac{\partial T}{\partial y}dx \right) \approx k\frac{T^n_{i,j} - T^n_{i+1,j}}{\Delta x}\Delta y + k\frac{T^n_{i,j} - T^n_{i-1,j}}{\Delta x}\Delta y + k\frac{T^n_{i,j} - T^n_{i,j+1}}{\Delta y}\Delta x + k\frac{T^n_{i,j} - T^n_{i,j-1}}{\Delta y}\Delta x \tag{G.5}$$

By substituting the equations (G.3) and (G.5) into the equation (G.1) and by rearranging terms an explicit finite volume scheme for 2D energy equation with no convection is obtained. The time differencing for the equation is forward time difference i.e. the next time step is calculated with the known values at current time step. The spatial differencing uses central differencing i.e. the gradients at face are calculated with the values of adjacent nodes. (Patankar, 1980, Chapter 4)

$$\frac{T^{n+1}_{i,j} - T^n_{i,j}}{\Delta t} = \alpha \left(\frac{T^n_{i+1,j} - 2T^n_{i,j} + T^n_{i-1,j}}{\Delta x^2} + \frac{T^n_{i,j+1} - 2T^n_{i,j} + T^n_{i,j-1}}{\Delta y^2} \right) \tag{G.6}$$

In the equation (G.6) $\alpha = \frac{k}{c\rho}$ is the thermal diffusivity. While the example of the discretisation is given to a rather simple problem, the 3D problem with any governing equation is formulated in a same way. The only differences are three dimensionality and the utilised discretisation for the time and spatial gradients. (Patankar, 1980, Chapter 4)

Typical spatial differencing schemes in CFD where convection is dominating are upwind and second-order upwind schemes which uses values upstream to formulate the gradient. Additionally, there is a power-law scheme which uses power law approximation, central-differencing which uses adjacent values and QUICK and MUSCL schemes which are a mixture of second-order upwind and central-differencing schemes. There are even more schemes but these are only ones given in ANSYS Fluent. (Ansys Inc., 2016, Spatial Discretization)

For time differencing schemes ANSYS Fluent provides first and second order implicit schemes for pressure-based solver which differ in number of time values they use. In addition there is a bounded version of second order scheme which may be beneficial in solving compressible flows. For density-based solver there are additional explicit formulations. (Ansys Inc., 2016, Temporal Discretization)

For the boundary conditions things get slightly more complicated as the given boundary condition may be a constant temperature or a constant heat flux or a given convective or radiation heat transfer coefficient and temperature at infinity. However, the basic method is similar to cell face formulation, only the boundary values have to be substituted to correct ones. For given temperature the temperature at cell face is known and the gradient is formulated on half of cell size. For constant heat flux the gradient at the cell face is known and no approximation is needed. For heat transfer coefficient the heat flux at wall is equal to the convective

heat transfer at outside. (Ansys Inc., 2016, Cell Zone and Boundary Conditions)

H. DIMENSIONLESS NUMBERS PLOTTED FOR ALL CASES

Before differentiating the effect of the fin parameters on the dimensionless numbers it is worthwhile to get an overall view of the Reynolds number dependency of the dimensionless numbers, to see if there is any simple data fit possible for multiple geometries. The values used in these graphs are available in the Appendices F and A.

Shah (1978) has given a heat transfer surface area-goodness criterion H.1. The area goodness is usually rather constant for a range of Reynolds numbers and high values of area goodness means that the heat exchanger requires a low frontal area.

$$\text{area goodness} = \frac{j}{f} \tag{H.1}$$

Kays and London (1964, Chapter 1) has given a volume goodness criterion H.2 for which E and Z are given in H.3 and H.4. High volume goodness results in a heat exchanger with low volume. The A_{fr} in the equations is the frontal area of the heat exchanger core while the η_0 in the equations is the surface efficiency which is discussed more in-depth in section 3.1.

$$\text{volume goodness} = \frac{E}{Z} \tag{H.2}$$

$$E = \frac{\Delta P \dot{m}}{\rho_m L A_{fr}} \tag{H.3}$$

$$Z = \frac{\eta_0 h A}{L A_{fr}} \tag{H.4}$$

In the Fig. H.1 the Nusselt number calculated from the overall heat transfer coefficient $U = \eta_0 h$ as a function of the Reynolds number Re_D. It is apparent that there is a quite high dependency of the Nusselt number on the geometry as the data is quite heavily scattered. The trend is, as expected, rising with the Reynolds number.

H. Dimensionless numbers plotted for all cases

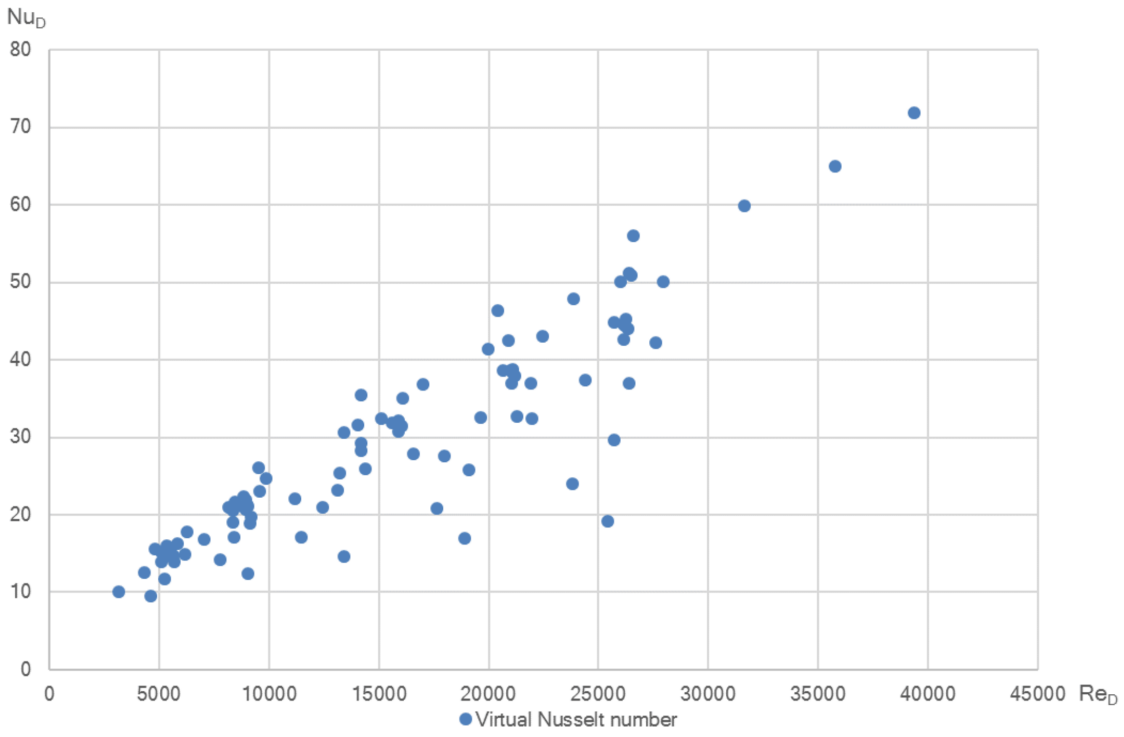

Figure H.1. *Nusselt number calculated from overall heat transfer coefficient as a function of the Reynolds number for all calculated cases.*

In the Fig. H.2 the Nusselt number has been calculated from heat transfer coefficient $h = \frac{U}{\eta_0}$ which almost eliminates the geometry dependency of the Nusselt number. As the overall heat transfer coefficient $U = \eta_0 h$ is still a value of the interest instead of the heat transfer coefficient h, the fin efficiency has to be calculated in some way. However, as seen on the flow field visualisation, the heat flux and thus the heat transfer coefficient in the channel between the tubes is rather constant while the recirculation areas have a rather low heat flux, the problem of the conjugated heat transfer could maybe be reduced to the calculation of the temperature distributions of the fin which is much less computational intensive, as the Nusselt number does not vary much with geometry. This should be still be validated with experiments as the CFD solutions contains simplifications and modelling errors. However, given the sheer amount of the CFD calculations and cases, the results should point to the correct direction.

H. Dimensionless numbers plotted for all cases

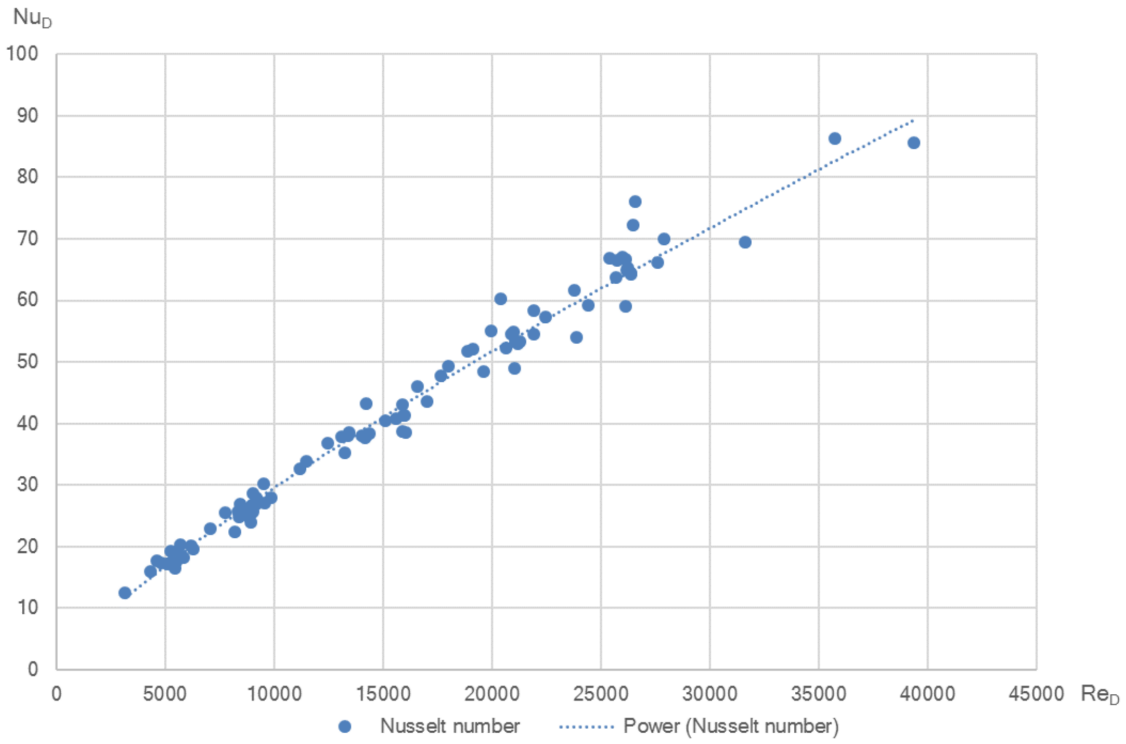

Figure H.2. *Nusselt number calculated by* $h = \frac{U}{\eta_0}$ *as heat transfer coefficient as a function of the Reynolds number for all calculated cases.*

The Fig. H.3 shows the Euler number as a function of Reynolds number for all cases. Its obvious that the geometry has a quite high effect on the Euler number and the trend is declining with Reynolds number. Most of the data point are in a range 0.17-0.22 and the geometries which deviate from this range the most are the cases where pitch and tube diameter were varied. It should also be noted that the pressure drop which Euler number is used for increases in power of two with velocity while heat transfer increases in power of less than unity and as such the precise value of Euler number may not even matter that much in thermal-hydraulic dimensioning.

H. Dimensionless numbers plotted for all cases

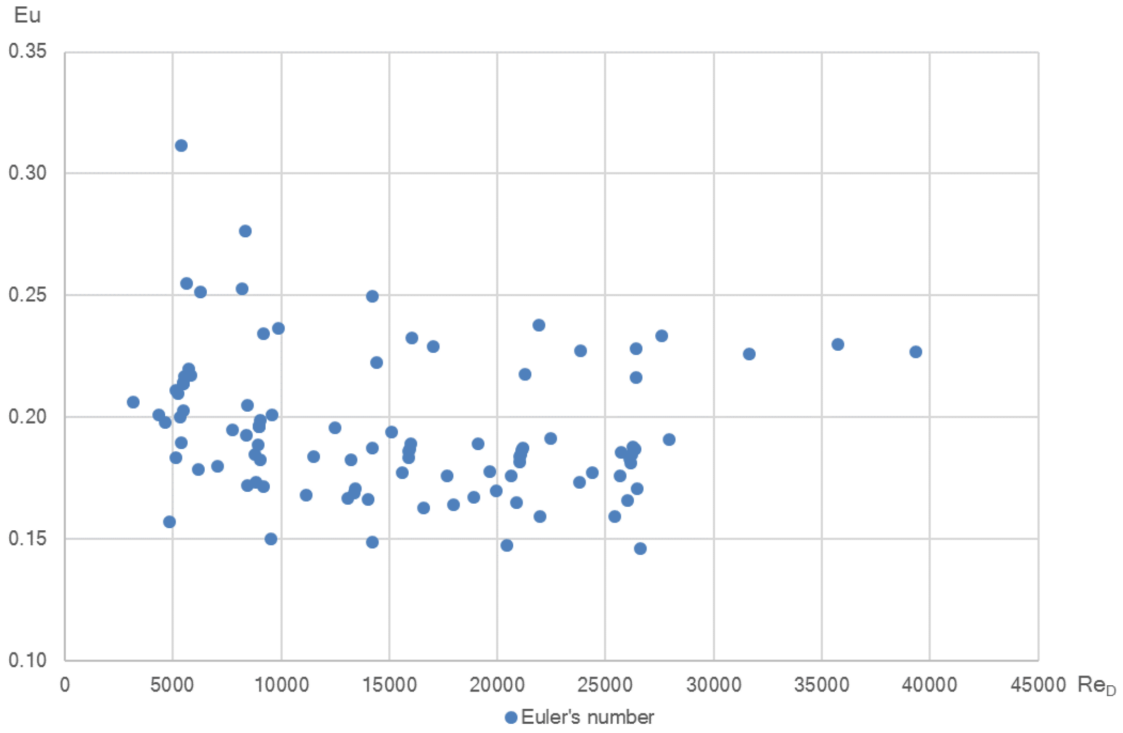

Figure H.3. *Euler number as a function of the Reynolds number for all calculated cases.*

Figure H.4 shows the Colburn j-factor and Fanning friction factor for all cases as a function of Reynolds number. There seems to be rather high correlation between two values which was expected from (Shah and Sekulic, 2003, Chapter 10.3.1.1). Additionally, the ratio of Colburn factor to Fanning friction factor is rather constant for a wide range of Reynolds numbers. Then problem of the choosing the most efficient heat exchanger is reduced down to picking up the heat exchanger geometry with the highest ratio of j to f.

H. Dimensionless numbers plotted for all cases

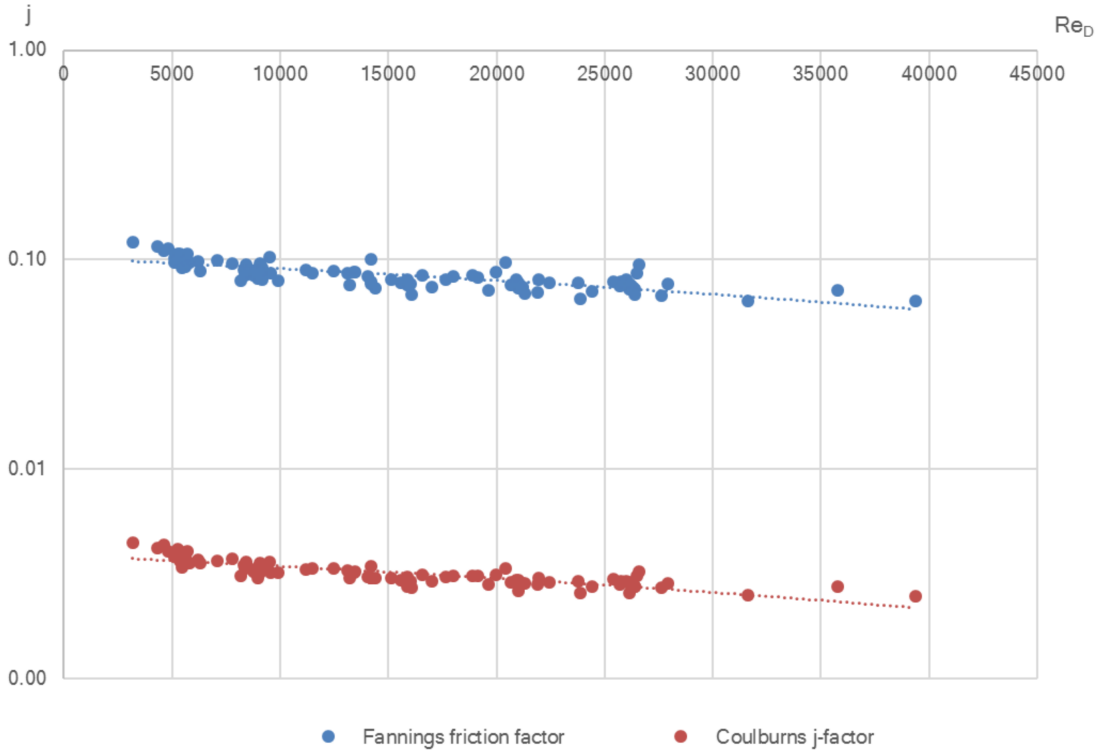

Figure H.4. *Colburn j-factor and Fanning friction factor as a function of Reynolds number.*

In the Fig. H.5 the ratio of the Colburn factor to Fanning friction factor also known as area goodness factor shows quite little dependency on Reynolds number. The ratio is also known as area-goodness ratio and the problem of choosing the heat exchanger surface with lowest frontal area is reduced to choosing the surface with highest ratio (Kays and London, 1964, Chapter 10.3.1.1.).

H. Dimensionless numbers plotted for all cases

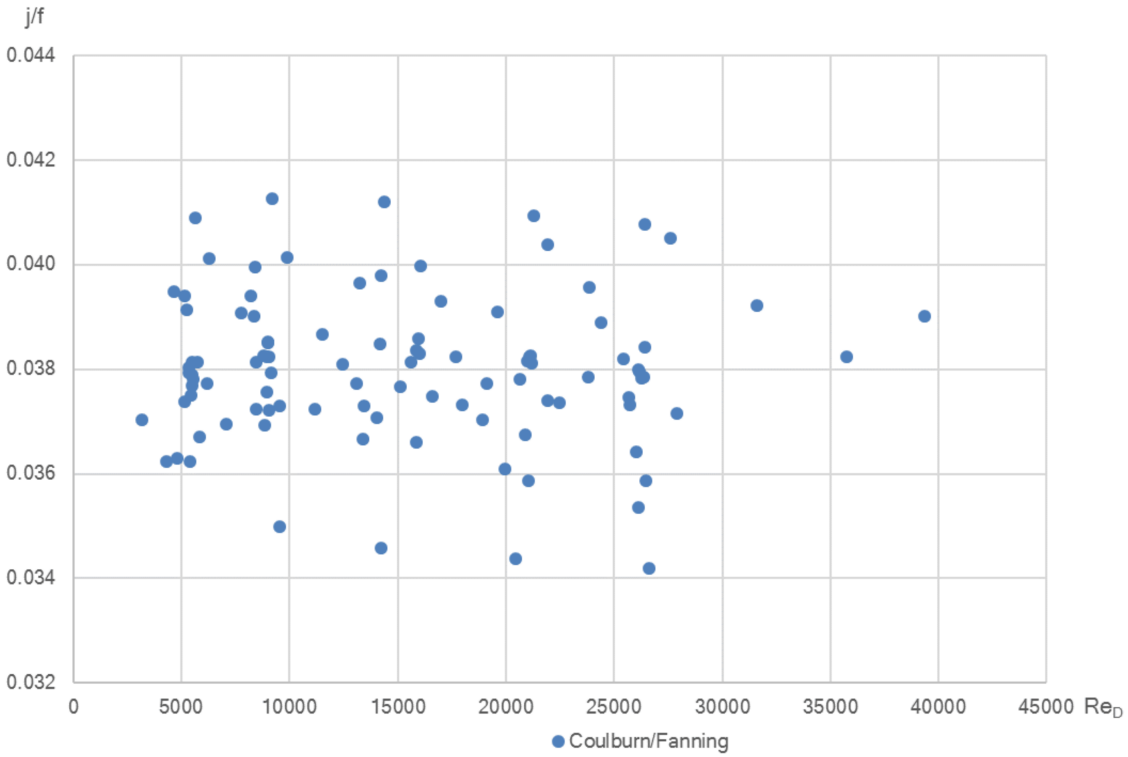

Figure H.5. *The ratio of Colburn j-factor and Fanning friction factor.*

The Fig. H.6 shows the ratio of the conductance per volume to pumping power per volume for all calculated cases. The ratio is known as volume goodness factor by (Kays and London, 1964, Chapter 1) and the highest Z values for given E corresponds to a heat exchanger with lowest volume. Most of the cases seems to be quite close to each other but the case for the lowest transverse pitch and fin pitch shows noticeably higher ratio while the case for the highest transverse pitch and fin pitch shows noticeably lower ratio.

H. Dimensionless numbers plotted for all cases

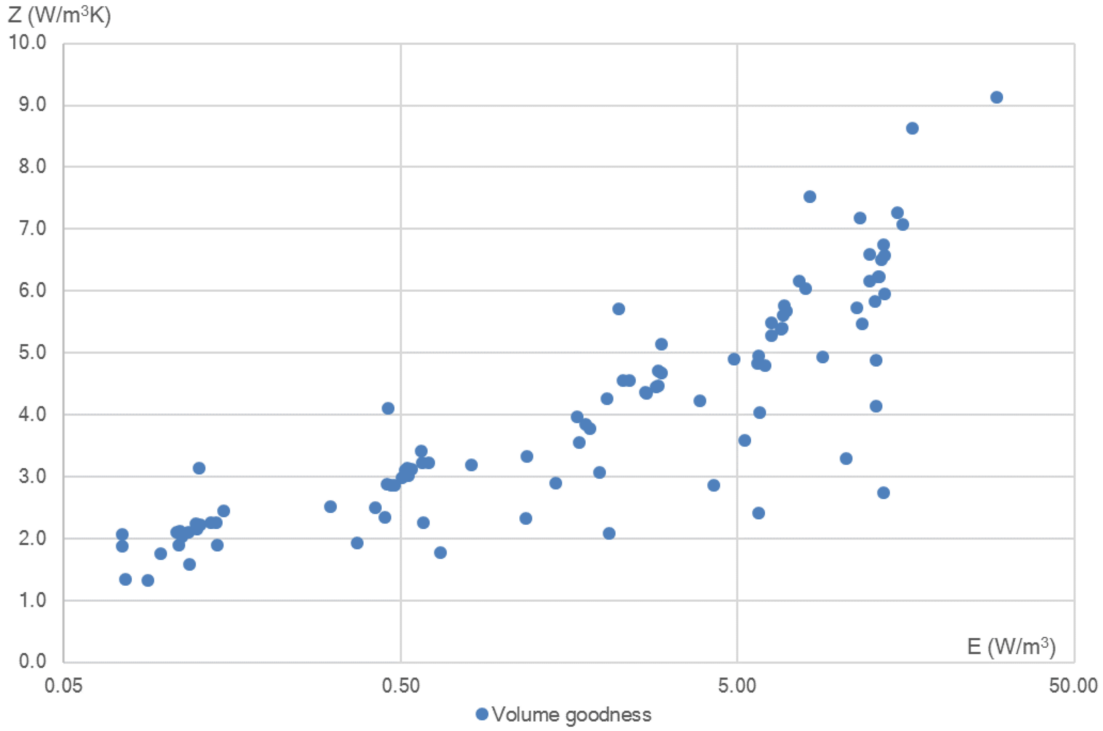

Figure H.6. *The ratio of conductance per volume to pumping power per volume*

I. UNIVERSAL CORRELATIONS FOR DIMENSIONLESS PARAMETERS FOR ALL CFD DATA

All correlations were developed with Microsoft Excel solver add-in by minimising the sum of square of errors. The correlations for all dimensionless numbers for the calculated cases were developed by quite subjectively choosing the dimensionless parameters to get best possible CFD data fit while simultaneously being as simple as possible. The Reynolds number in the correlations was based on the properties at average temperature, maximum velocity at the smallest cross-section and hydraulic diameter given in the equation (2.3). It should be noted that the heat transfer coefficient used in calculating the Nusselt number and Colburn j-factor was $h = \frac{U}{\eta_0}$ i.e. the overall heat transfer coefficient divided by the surface efficiency. This was done to improve the correlation accuracy considerably and get the value closer to the real convective heat transfer coefficient at the surface.

The correlations for Nusselt number, Euler number, Fanning friction factor and Colburn j-factor were found to correlate quite well with a power law fit with corrections for geometric variations. The fin efficiency was found to correlate rather well with the annular fin efficiency equation with some corrections for the effective fin height and non-homogeneous heat transfer coefficient. Additionally, at low Reynolds numbers a correction due for laminar flow was needed. If the reader is interested in the basis of these correlation the A with the knowledge of the six tubes in row and appendix F should be enough to calculate the specific numbers used in making these correlations with the help of some geometry and the equations given in this thesis.

As the fin efficiency is used in calculating the conductance with the Nusselt number a correlation for it is given in the equations (I.1), (I.2), (I.3), (I.4) and (I.5). The correlation has been adapted from the fin efficiency equation for an annular fin but some corrections has been made according to the CFD solutions to minimise the square sum of error (Incropera et al., 2011, Chapter 3.6.4).

$$\eta_f = \frac{2a}{b(1-a^2)} \frac{K_1(ab)I_1(a) - K_1(a)I_1(ab)}{K_1(a)I_0(ab) + K_1(ab)I_0(a)} \tag{I.1}$$

I. Universal correlations for dimensionless parameters for all CFD data

$$a = \frac{D}{L_{eff}} \tag{I.2}$$

$$b = \left(\sqrt{\frac{hL_{eff}^2}{2ks_f}} \right)^{1.19} \tag{I.3}$$

$$L_{eff} = (S_T - \delta_f)^{0.53} (S_L - \delta_f)^{0.47} \left(\frac{S_T - \delta_f}{D} \right)^{0.17} \left(\frac{S_L - \delta_f}{D} \right)^{0.05} \left(\frac{A_{fin}}{A_{contact}} \right)^{0.07} \tag{I.4}$$

$$A_{contact} = \pi D s_f \left(1 - \frac{2atan\left(\frac{\Delta_f}{D} \right)}{\pi} \right) \tag{I.5}$$

The Fig. I.1 shows the deviation of the correlation from CFD values with +-10 % lines. The single gilled tube had 2-4 percentage points higher fin efficiency in this Reynolds number range than the double gilled tube. The correlation was mostly within 5 % of CFD fin efficiency but the largest fin size of 125 mm resulted in 10 % error at low and high Reynolds numbers. The correlation gives slightly higher values overall compared to CFD solutions.

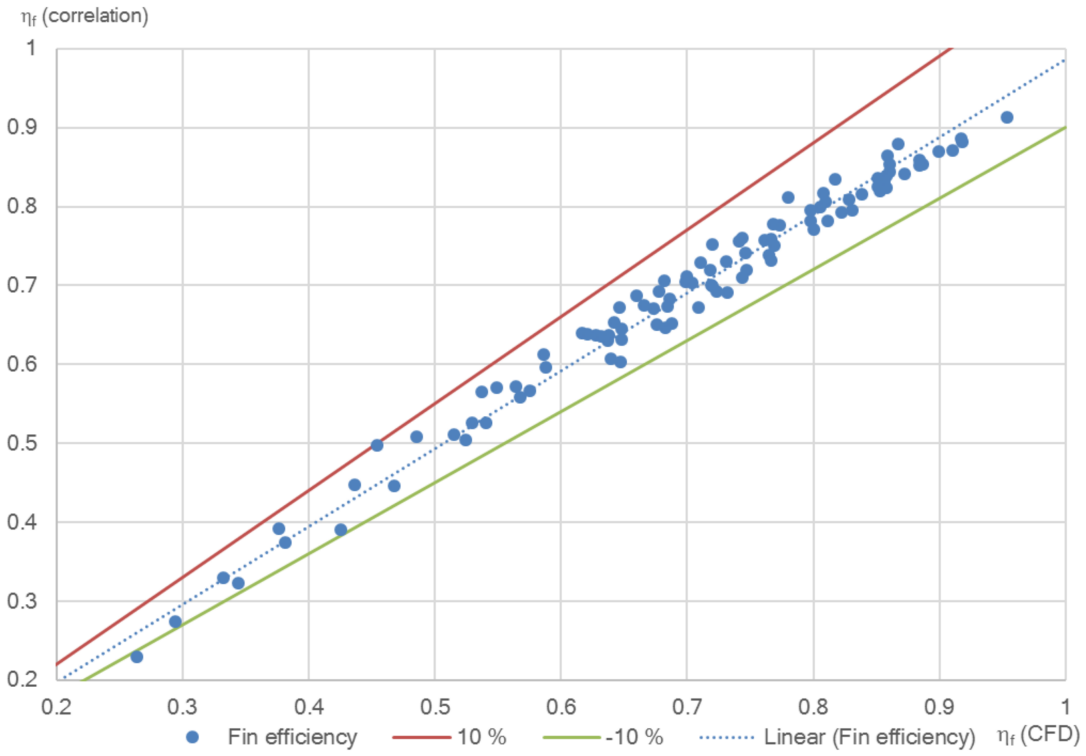

Figure I.1. *Deviation of the fin efficiency correlation from CFD fin efficiency.*

The effect of almost all geometric parameters to the Nusselt number correlation (I.6) was encapsulated into the ratio of the hydraulic diameter to the tube diameter when a Reynolds number based on hydraulic diameter was used. Additionally, a low Reynolds number correction was included to account for laminar flow. The slit width was also found to have a slight effect on the area averaged Nusselt number which is most likely due to the decrease in the low heat transfer area at recirculation areas between the tubes. The Nusselt number for single gilled tube was found to be 9 % lower than with double gilled tubes for a given Reynolds number, and as such the Nusselt number can be multiplied by 0.91 if single gilled tubes are used.

$$Nu_{D_h} = 0.00353(Re_{D_h} + 1530)^{0.963} \left(\frac{D_h}{D}\right)^{0.28} \left(\frac{\Delta_f}{D}\right)^{0.017} \tag{I.6}$$

The Fig. I.2 shows the deviation of the correlation from CFD values with +-10 % lines. The error of correlation when compare to the CFD solutions was less than 5 % for all data points except for couple of low Reynolds number CFD solutions.

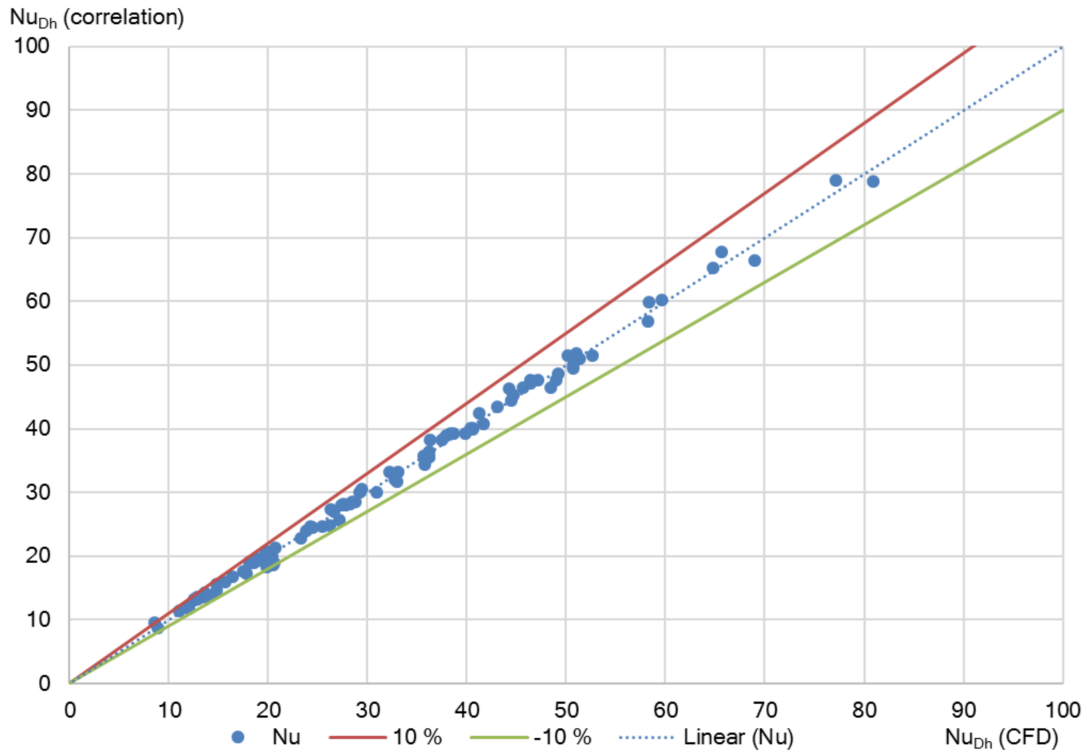

Figure I.2. *Deviation of the Nusselt number correlation from CFD Nusselt number.*

The Colburn j-factor was found to correlate worse with the CFD results than the Nusselt number. The correlation (I.7) is of similar form to Nusselt number correlation.

$$j_{D_h} = 0.0119(Re_{D_h} - 2140)^{-0.119} \left(\frac{D_h}{D}\right)^{0.317} \left(\frac{\Delta_f}{S_T}\right)^{0.029} \tag{I.7}$$

The Fig. I.3 shows the deviation of the correlation from CFD values with +-10 % lines. The error was slightly higher than with Nusselt number correlation but the agreement with the CFD results was for most cases within 5 % with couple of low Reynolds number values at 10 % range.

I. Universal correlations for dimensionless parameters for all CFD data

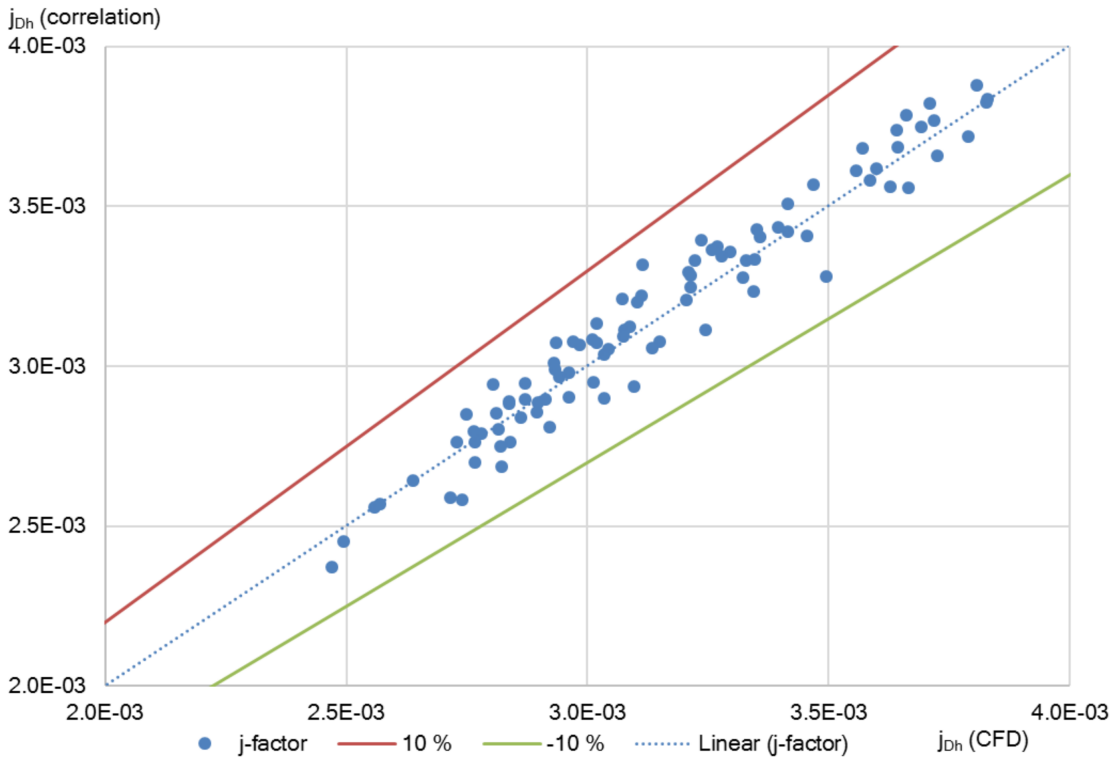

Figure I.3. *Deviation of the Colburn number correlation from CFD Colburn number.*

The best simple correlation (I.8) for Euler number was found when ratios of hydraulic diameter to tube diameter, the fin surface area to tube surface area, longitudinal pitch to tube diameter and transverse pitch to tube diameter was utilised in correlation. Additionally, a low Reynolds correlation was needed due to laminar flow. The Euler number for single gilled tube was found to be 4 % lower than with double gilled tubes for a given Reynolds number, and as such the Euler number can be multiplied by 0.96 if single gilled tubes are used.

$$Eu_{D_h} = 0.202(Re_{D_h} - 2430)^{-0.061} \left(\frac{D_h}{D}\right)^{-0.53} \left(\frac{A_{fin}}{A_{tube}}\right)^{-0.85} \left(\frac{S_T - \delta_f}{D}\right)^{0.08} \left(\frac{S_L - \delta_f}{D}\right)^{0.67} \tag{I.8}$$

The Fig. I.4 shows the deviation of the correlation from CFD values with +-10 % lines. The error of the correlation was less than 5 % for almost all CFD solutions except for high fin pitches where the error was at maximum of 10 %. The Colburn j-factor for single gilled tube was found to be 9 % lower than with double gilled tubes for given Reynolds number and as such the j-factor can be multiplied by 0.91 if single gilled tubes are used.

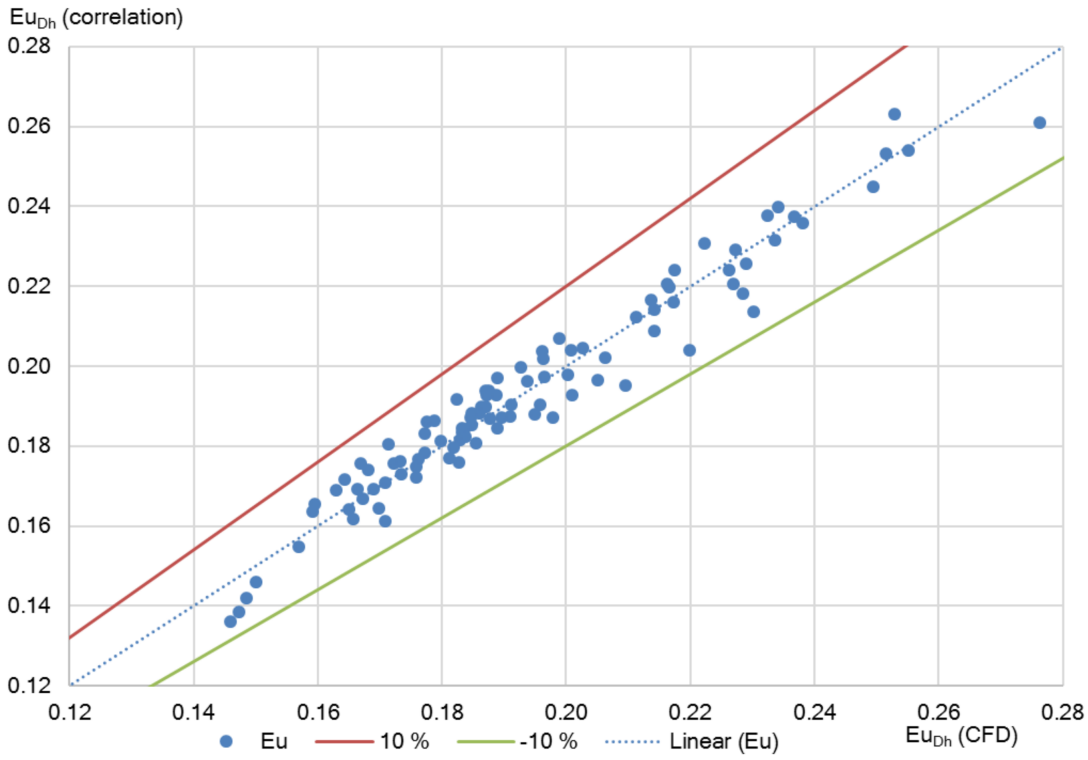

Figure I.4. *Deviation of the Euler number correlation from CFD Euler number.*

Fanning friction factor correlation (I.9) assumed similar form to Euler number correlation. The correlation was not, however, as good as Euler number correlation. The correlation with the CFD values was actually worst of all correlation. The Fanning friction factor for single gilled tube was found to be 5 % lower than with double gilled tubes for a given Reynolds number and as such the Fanning friction factor can be multiplied by 0.95 if single gilled tubes are used.

$$f_{D_h} = 0.277(Re_{D_h} - 2360)^{-0.12} \left(\frac{D_h}{D}\right)^{0.33} \left(\frac{A_{fin}}{A_{tube}}\right)^{-0.096} \left(\frac{S_T - \delta_f}{D}\right)^{0.25} \left(\frac{S_L - \delta_f}{D}\right)^{-0.077} \tag{I.9}$$

The Fig. I.5 shows the deviation of the correlation from CFD values with +-10 % lines. The correlation was within 10 % of the CFD data but the scatter were quite high.

I. Universal correlations for dimensionless parameters for all CFD data

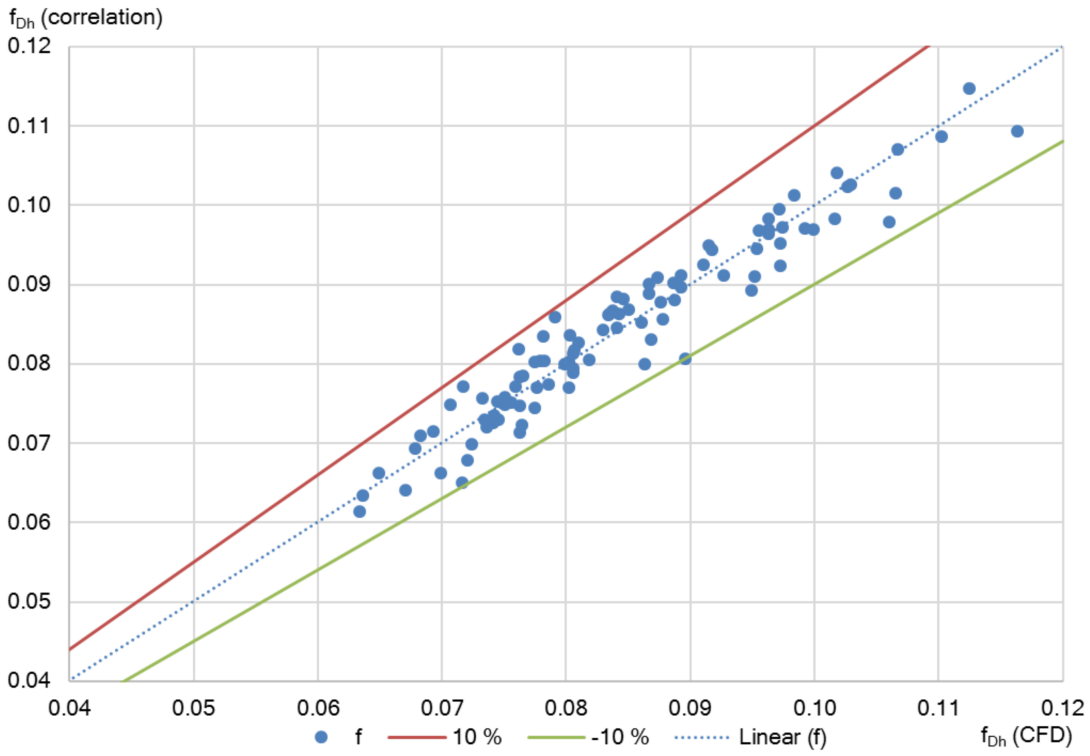

Figure I.5. *Deviation of the Fanning number correlation from CFD Fanning number.*

The error in conductance for all cases when the Nusselt number and fin efficiency correlations were used to calculate the conductance was within 6 % except for couple of low Reynolds number and high transverse and longitudinal pitches solutions. The agreement of conductance calculated from correlations with CFD solutions is shown in Fig. I.6 with +-10 % lines.

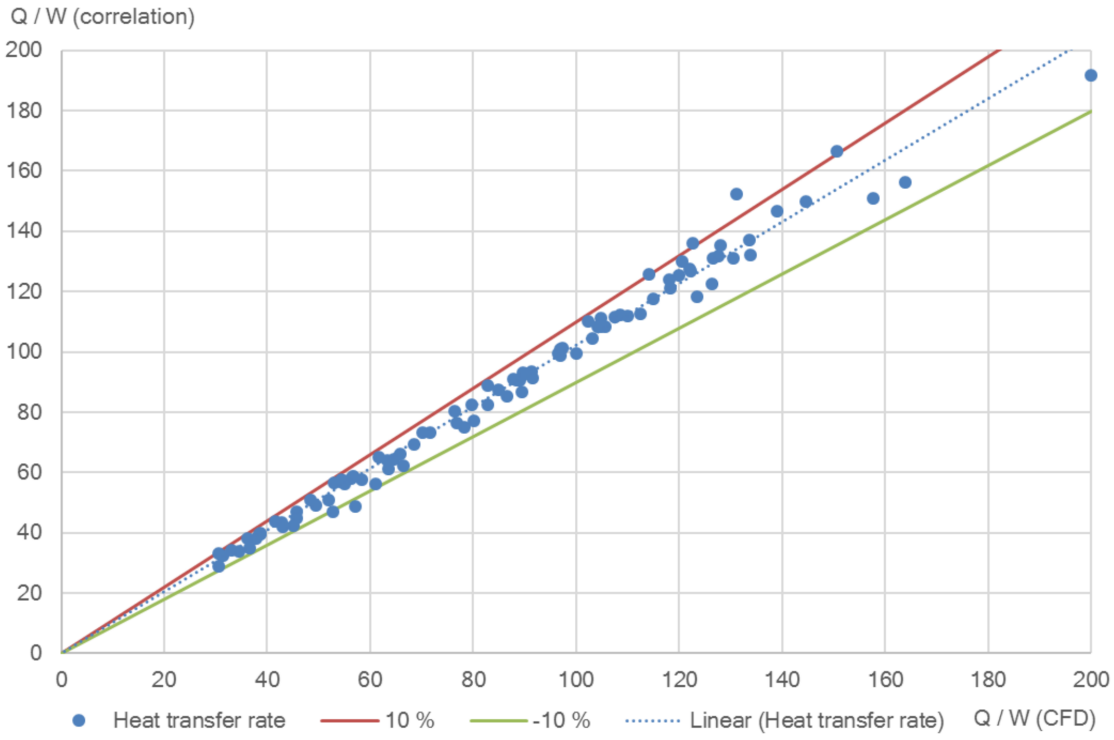

Figure I.6. *Deviation of the heat transfer rate calculated from Nusselt number and fin efficiency correlations from CFD heat transfer rate.*

The pressure drop calculated from the Euler number correlation agreed slightly better with CFD solutions than conductance. The error was less than 6 % for all values but couple of low Reynolds number CFD solutions.

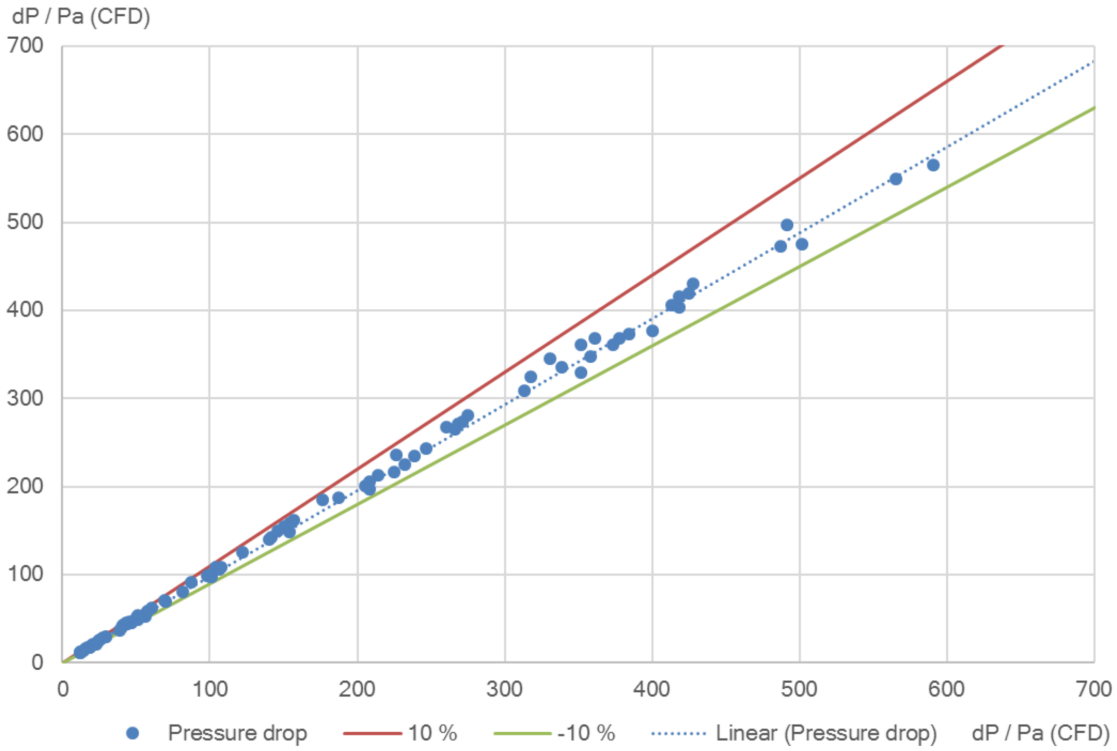

Figure I.7. *Deviation of the pressure drop calculated from Euler number correlation from CFD pressure drop.*

J. CORRELATIONS FOR INDIVIDUAL CASES

The correlations for individual CFD cases are given in Table J.1 below. The Euler number and Nusselt number were found to follow a power law fit (J.1) while the fin efficiency followed a quadratic equation (J.2). Although, for this Reynolds number range the fin efficiency followed even linear fit quite faithfully. The characteristic dimension in the all dimensionless numbers is the tube diameter and the characteristic velocity is the maximum velocity at the smallest cross-section. All properties were evaluated at the average temperature between the inlet and outlet. The heat transfer coefficient used in calculating the Nusselt number is the $h = \frac{U}{\eta_0}$.

$$\begin{aligned} Eu &= ARe_D^B \\ Nu &= ARe_D^B \end{aligned} \tag{J.1}$$

$$\eta_f = A + BRe_D + CRe_D^2 \tag{J.2}$$

J. Correlations for individual cases

Table J.1. *Correlations for individual CFD cases.*

Case	A_{η_f}	B_{η_f}	C_{η_f}	A_{Eu}	B_{Eu}	A_{Nu}	B_{Nu}
1	9.109E-01	-1.354E-05	1.093E-10	0.4668	-0.0931	0.0102	0.8275
2	8.879E-01	-1.357E-05	1.186E-10	1.3541	-0.1739	0.0128	0.7595
3	9.202E-01	-1.327E-05	9.694E-11	0.2518	-0.0398	0.0090	0.8765
4	9.344E-01	-1.466E-05	1.332E-10	0.2206	-0.0410	0.0144	0.8692
5	8.524E-01	-2.327E-05	3.374E-10	0.6321	-0.1397	0.0174	0.7974
6	9.347E-01	-8.094E-06	4.256E-11	0.3797	-0.0496	0.0065	0.8478
7	8.517E-01	-1.794E-05	2.121E-10	0.6258	-0.1060	0.0138	0.7962
8	9.259E-01	-1.016E-05	4.347E-11	0.3798	-0.0838	0.0085	0.8497
9	8.511E-01	-1.576E-05	1.767E-10	0.5428	-0.1128	0.0156	0.7849
10	9.438E-01	-1.317E-05	1.230E-10	0.4282	-0.0805	0.0075	0.8574
11	8.927E-01	-3.428E-05	7.298E-10	0.1246	0.0318	0.0124	0.8636
12	9.451E-01	-3.931E-06	2.910E-12	0.4695	-0.0705	0.0040	0.8490
13	9.162E-01	-1.352E-05	1.204E-10	0.4302	-0.0838	0.0091	0.8374
14	9.029E-01	-1.488E-05	1.370E-10	0.4987	-0.1003	0.0117	0.8219
15	9.094E-01	-1.377E-05	1.195E-10	0.4756	-0.0935	0.0097	0.8288
16	9.235E-01	-1.362E-05	1.181E-10	0.3961	-0.0817	0.0103	0.8343
17	9.584E-01	-1.548E-05	1.771E-10	0.3613	-0.0691	0.0104	0.8181
18	6.812E-01	-2.503E-05	4.217E-10	0.6076	-0.1260	0.0285	0.7665
19	7.829E-01	-2.526E-05	3.913E-10	0.5643	-0.1108	0.0210	0.7900
20	6.100E-01	-2.766E-05	5.047E-10	0.5760	-0.1266	0.0285	0.7767
21	1.000E+00	0.000E+00	0.000E+00	0.1280	-0.0186	0.0913	0.7447

K. GEOMETRIC PARAMETERS FOR EXHAUST GAS BOILER DIMENSIONING

The geometric parameters useful for the heat exchanger dimensioning are given in the Table K.1. The parameters are the tube diameter D, transverse pitch S_T, longitudinal pitch S_L, heat surface area per metre of a finned tube $\frac{A_h}{L}$, minimum cross-sectional area per metre of a finned tube $\frac{A_c}{L}$ and mass per metre of a finned tube $\frac{m}{L}$. The heat transfer area, cross-sectional area and mass are for double-gilled finned tube. Even the single gilled tube and bare tube bank (case 17 and case 21) are calculated for two tubes.

Table K.1. *Geometric parameters useful for heat exchang*

$Case$	$D(mm)$	$S_T(mm)$	$S_L(mm)$	$\frac{A_h}{L}\left(\frac{m^2}{m}\right)$	$\frac{A_c}{L}\left(\frac{m^2}{m}\right)$	$\frac{m}{L}\left(\frac{kg}{m}\right)$
1	38	75	75	0.671	0.0313	8.64
2	38	75	75	0.946	0.0285	11.28
3	38	75	75	0.533	0.0328	7.32
4	38	75	75	0.395	0.0342	6.00
5	38	100	75	0.920	0.0522	11.04
6	38	60	75	0.521	0.0188	7.20
7	38	75	100	0.904	0.0313	10.76
8	38	75	60	0.531	0.0313	7.36
9	38	75	75	0.697	0.0334	6.75
10	38	75	75	0.647	0.0296	10.29
11	28	75	75	0.708	0.0397	8.19
12	52	75	75	0.584	0.0197	8.92
13	38	75	75	0.684	0.0313	8.71
14	38	75	75	0.640	0.0313	8.45
15	38	75	75	0.685	0.0312	8.78
16	38	75	75	0.627	0.0318	8.23
17	38	75	75	0.667	0.0313	8.57
18	38	100	100	1.105	0.0564	9.16
19	38	100	100	1.126	0.0527	13.03
20	38	125	100	1.431	0.0789	5.53
21	38	75	75	0.239	0.0740	1.68